MULTIFUNCTIONAL BIOSENSORS USING ZnO AND ITS NANOSTRUCTURES

by

PAVEL IVANOFF REYES

A Dissertation submitted to the

Graduate School-New Brunswick

Rutgers, The State University of New Jersey

in partial fulfillment of the requirements

for the degree of

Doctor of Philosophy

Graduate Program in Electrical and Computer Engineering

written under the direction of

Professor Yicheng Lu

and approved by

_____

_____

_____

_____

_____

New Brunswick, New Jersey

May, 2012

ABSTRACT OF THE DISSERTATION

Multifunctional Biosensors Using ZnO and its Nanostructures

By PAVEL IVANOFF REYES

Dissertation Director:
Prof. Yicheng Lu

In recent years, biosensors research has emerged as a major field in both academic institutes and industries with broad applications in drug discovery and development, clinical diagnostic tools, cancer and genetic research, agricultural and veterinary analysis, pollution and contamination monitoring, and food processing. ZnO is a wide band gap semiconductor with unique multifunctional material properties, which is particularly attractive for sensor technology. ZnO can be grown as thin films or as nanostructures with different morphologies on various substrates. Through proper doping, ZnO and its ternary $Mg_xZn_{1-x}O$ can be made transparent and conductive, piezoelectric, or ferromagnetic. ZnO-based sensors have demonstrated high sensitivity to various organic and inorganic gases and liquids. The biocompatibility of ZnO is demonstrated in detections of proteins, antibodies, and DNA through the proper surface functionalization. The control of the surface wettability of ZnO nanotips between super-hydrophilic and super-hydrophobic states are used to dramatically enhance the sensitivity of ZnO-based biosensors.

The aim of this work is to create new paradigms in sensor technology through novel manipulation of nanometer-scale ZnO surfaces and structures, advancement of ZnO-based multi-modal sensing (e.g., acoustic, electrical, and optical). The new sensor

technology is based on combination of accurate and high quality growth of multifunctional ZnO single crystal nanostructure arrays, organic and biomolecular functionalization of ZnO surfaces, and design and development of sensor platforms and devices. The key results of this research features the following sensors and their specific applications: (i) ZnO nanostructure-modified thin film bulk acoustic wave resonator (ZnO_{nano}-TFBAR) for DNA detection, (ii) ZnO nanostructure-modified quartz crystal microbalance (ZnO_{nano}-QCM) for dynamic and noninvasive monitoring of bovine aortic endothelial cells (BAEC), (iii) sensor-on-food packaging based on ZnO surface acoustic wave (SAW) sensor built on protein-coated flexible substrates, and (iv) ZnO thin film transistor immunosensor (ZnO-bioTFT) for detection of epithelial growth factor receptor (EGFR) proteins found in breast cancer cells. The new ZnO sensor technology presents great impact on the future classes of multi-modal and multifunctional biosensors and biochips for applications such as cell-based assay development, smart food packaging, and high throughput biosensor arrays that perform highly sensitive and selective biochemical detection.

DEDICATION

To my mentors:

Diosdado Reyes, who taught me the lessons of life

Prof. Cesar Saloma, who taught me the beauty of Physics

Prof. Delfin Jay Sabido, IX, who taught me the practicality of Engineering

Dr. Paul Westbrook, who taught me the wonders of Innovation

Prof. Nada Boustany, who taught me the complexity of Biology

and

Prof. Yicheng Lu, who taught me how to combine life, Physics, Engineering, Innovation, and Biology into one coherent whole.

To the memory of my mother, Luzviminda Reyes

May this work in its small way contribute to the fight to end all illness.

ACKNOWLEDGEMENTS

First, I would like to express my deepest gratitude to my dissertation advisor, Professor Yicheng Lu, for bringing out my potential, for his unwavering support, guidance, encouragement, and patience. Thank you for laying down the solid foundation for my future career.

I would like to thank my dissertation committee members, Prof. Jaeseok Jeon, Prof. Wei Jiang, Prof. Warren Lai, and Prof. Nada Boustany for taking time off of their busy schedule to review and critique my dissertation.

My thanks also go to my collaborators without whom I am not able to establish such an interdisciplinary body of work: Prof. Elena Galoppini, Dr. Olena Taratula and Yan Cao from Rutgers Newark, Prof. Ki-Bum Lee, Aniruddh Solanki, and Dr. Sung Myung from Rutgers Wright Reimann Labs, Prof. Nada Boustany and Dima Khavulya from Rutgers Biomedical Engineering Department, and Prof. Qingrong Huang and Ji Li from Rutgers Food Science Department.

I would like to thank my colleagues in Prof. Lu's research group, who have provided support throughout my work. Dr. Jian Zhong, Dr. Ying Chen, and Dr. Zheng Zhang for training me in microelectronic device fabrication and characterization. Dr. Hanhong Chen, Dr. Gaurav Saraf and soon to be Dr. Ziqing Duan for material growth and film characterizations. Mr. Jeren Ku for his invaluable device fabrication expertise and insights. Mr. Yang Zhang, Mr. Rui Li and Wen Chiang, for their help in the many facets of my work in the group, and the great friendship. Working with you guys is such an honor.

I would like to thank my family (my father Diosdado, my brothers Vajramejev and Yevgeny and their wives Celina and Victoria, my favorite aunt Consuelo, and my niece Svetlana) in Cavite Viejo, Philippines who have been my constant source of strength and support. I would like to thank them for understanding me when it was time for me to go and chart a new life for myself in a foreign land. I also thank my family in the United States: Allan Altman, my best friend for life and Dayle Treece, my mom-away-from-home for taking me in unconditionally.

This work has been supported in part by the United States Air Force Office of Scientific Research (AFOSR) under Grant No. FA9550-08-01-0452, and by the National Science Foundation (NSF) under Grant No. ECCS 1002178.

TABLE OF CONTENTS

LIST OF ILLUSTRATIONS

Chapter 1

Introduction

1.1. Motivation

Biosensors research is emerging as a major focus in both academic and commercial sectors. According global market analysts, the biosensor market is projected to reach $12 billion by 2015 [1]. The emergence of new technologies in materials design, device fabrication, microfluidics, and nanotechnology, and the maturation of biochemical analytics helped propel this market viability. The key areas of growth in biosensors research are in non-invasive sensor platforms, device design with increasingly high accuracy, sensitivity, selectivity, and compactness, real-time point-of-care testing, and development of high throughput, multi-species biochemical protocols. The applications for biosensors have widened in recent years to include drug discovery and development, clinical diagnostic tools, cancer and genetic research, agricultural and veterinary analytical tools, pollution and contamination monitoring, and food processing.

ZnO is emerging as a highly viable wide bandgap semiconductor. Through proper doping and alloying ZnO can be made as a multifunctional material, which is particularly attractive for sensor technology. ZnO based sensors have demonstrated high sensitivity to a variety of chemicals such as CH_4, CO, H_2O, H_2, NH_3, trimethylamine, ethanol and NO_2 [2,3]. ZnO and its ternary alloy, $Mg_xZn_{1-x}O$ are known to be biocompatible oxides, in which Zn and Mg are important elements for neuroetransmitter production and enzyme function[4]. ZnO is particularly attractive as a bio-interface for various biochemical species because ZnO nanostructures can be grown with different morphologies (nanometer-scale rods, belts, tips, etc) on various substrates including Si,

quartz, glass, and metals. ZnO nanostructures are also considered as a coating material for medical implants [5]. It is shown that ZnO nanorods are compatible with intracellular material and are highly sensitive to pH changes inside cellular environments [6]. ZnO nanorods are also used for detection of enzymatic reactions with target biochemicals[7]. The biocompatibility of ZnO and its feasibility for biosensing applications are further demonstrated in detections of proteins, antibodies, and DNA through the proper surface functionalizations [8,9,10,11]. The control of the surface wettability of ZnO nanotips between the super-hydrophillic and super-hydrophobic status is used to dramatically enhance the sensitivity of the biosensors [10].

The aim of this interdisciplinary work is to create new paradigms in biosensor technology through the novel manipulation of nanoscale surfaces and structures, advancement and optimization of current capabilities in developing ZnO-based multi-modal sensing (e.g., acoustic, electrical, and optical). The sensors will be developed by combining techniques of: (i) accurate and high quality growth of multifunctional ZnO thin and single crystal ZnO nanostructure arrays, (ii) organic and biomolecular functionalization, and (iii) development of sensor platforms and devices for applications in biochemical detection and dynamic and noninvasive techniques of monitoring biophysical activity. The work seeks to show through the unique properties of ZnO as a sensor material, we can achieve our ultimate goal of multifunctional sensor technology.

1.2. Objectives and Scope of Work

The objective of this research is to design, fabricate and characterize the prototypes of ZnO nanostructure-based biosensors with multifunctional and multi-modal operation. The scope of this study covers:

(1) Development, design and characterization of the ZnO nanostructure-based bio-interface through biofunctionalization protocols and biomolecular/biospecies binding studies, wettability control, and surface morphology control.

(2) Design, fabrication and characterization of the multifunctional ZnO-based devices, specifically the surface and bulk acoustic wave devices, and the thin film transistor. These devices are used as the core sensor building-blocks to realize the multi-modal biosensors.

(3) Integration of the ZnO nanostructured bio-interface with the multifunctional ZnO-based core devices to demonstrate biosensing, specifically DNA/oligonucleotide sensing, antibody-protein reaction detection (immunosensing), dynamic and noninvasive cellular monitoring, and surface acoustic wave-based sensor built directly on a protein coated flexible substrate (to serve as sensor-on-food packaging (SOFP) platform).

1.3. Organization of the Dissertation

After establishing the motivation and the specific objectives and scope of this research in Chapter 1, a review of the related work on ZnO-based biosensors is presented in Chapter 2. Chapter 2 also provides a background on the technical approach employed in designing ZnO nanostructure-based biosensors starting from the bio-interface to the core sensing devices. Chapter 3 includes a discussion of the development of the ZnO nanostructure-based bio-interface. A detailed description of the experimental results is also presented on the biofunctionalization protocols for ZnO and optimization of cellular adhesion and DNA immobilization through surface morphology control of the ZnO

nanostructures. Chapters 4 through 7 will focus on the various ZnO-based biosensor prototypes. In particular: Chapter 4 deals with DNA/oligonucleotide sensors using the ZnO-based thin film bulk acoustic wave resonator (ZnO_{nano}-TFBAR); Chapter 5 presents the use of the ZnO-based quartz crystal microbalance (ZnO_{nano}-QCM) and the Butterworth van-Dyck (BVD) multiparameter modeling to perform dynamic and noninvasive cellular monitoring of bovine aortic endothelial cells (BAEC); Chapter 6 presents a piezoelectric ZnO-based surface acoustic wave (SAW) sensor built directly on a protein-coated flexible substrate, that serves as a novel sensor-on-food package (SOFP) platform; and Chapter 7 discusses the demonstration of a highly sensitive and selective immunosensing using a ZnO-based thin film transistor (ZnO bioTFT). Finally, Chapter 8 summarizes the results of the dissertation research and presents further work.

Chapter 2

Technical Background

In recent years, biosensors design and development has emerged as a major field of research with high global market potential. Currently, the most significant contribution of biosensor research is in medical applications such as development of analytical tools for blood analysis, drug discovery, point-of-care monitors, and genetic analysis, and clinical diagnostic tools. However, biosensors are not only indispensable for medical purposes, but are gaining more ground in utility in environmental applications (pollution and contamination analysis), agricultural and food industry applications (intelligent food packaging, horticultural and veterinary diagnostic tools), and security. Development of sensitive biosensors and other devices that would detect toxic biological agents and hazardous chemicals has recently become one of the most urgent and important focus of biosensors research. Ongoing research is geared toward sensors with high accuracy, selectivity, sensitivity, reduced device dimensions, and increased portability. In this chapter, the role of ZnO in the field of biosensors research will be discussed. ZnO has been proven to be a promising material in fabricating biosensor platforms as it possesses a good degree of biocompatibility and ability for biomolecular binding. Various biosensing devices based on ZnO operating in different modes will also be discussed in this chapter.

2.1. Biosensors and their Figures of Merit

A biosensor is a device having a biological sensing element either intimately connected to or integrated with a transducer. The purpose of this device is to produce an

electronic, optical, or acoustic signal, which is proportional to the concentration of a specific chemical or set of chemicals. Significant progress has been made in this field for the last several years, which exploit technological advances in microfabrication, optoelectronics and nanotechnology. Biosensors have a variety of very important applications and impact on such areas as drug discovery and development, biochemical synthesis, biomaterial development (medical implants), discovery of new biological functions, medical and clinical applications (cancer treatment, disease detection, pathogen detection), environmental monitoring (control of pollution and detection of hazardous chemicals), food analysis (detection of ingredients, contamination etc.), and detection of biological warfare agents.

The operation of biosensors may be classified into three modes: (i) identifying and quantifying the presence of a specific bio-species either in pure state or in solution with other species [12], (ii) extracting information about the fundamental mechanism of a biochemical reaction [13], and (iii) using the sensor itself to facilitate biochemical reactions to synthesize another biochemical [14]. With these modes of operation follow figures of merit that would quantify the efficiency of the biosensor. The primary figures of merit that characterize a biosensor are sensitivity and selectivity.

Sensitivity:

Sensors that register a linear relationship between its output signal and the quantity it is detecting is referred to as a linear sensor. For this type of sensor its sensitivity is defined as the amount of sensor signal change per unit change in the amount of analyte being detected. For this case the sensitivity value is also the calibration coefficient of the

sensor. For sensors that have a nonlinear response, the sensitivity is defined by its detection limit or the lowest amount of analyte that can still register a change in the device.

Selectivity:

There are instances when a multi-species solution containing the target analyte is introduced into the sensor. For a good sensor design, even with the presence of multiple species only the target molecules should be immobilized onto the sensor and register a unique signal. For this case the sensor's sensitivity is not the only important figure of merit but its selectivity should be quantified. The selectivity limit is defined as the lowest amount of analyte that can still register a change in the device even in the presence of other species.

2.2. ZnO as a Biosensing Material

2.2.1. Multifunctionality and Biocompatibility of ZnO

ZnO is a wide band gap semiconductor with unique multifunctional material properties, which is particularly attractive for sensor technology. It can be grown as thin films or as nanostructures on a variety of substrates. Through proper doping and alloying, ZnO and $Mg_xZn_{1-x}O$ can be made transparent and conductive [15], piezoelectric [16], or ferromagnetic [17,18], allowing it to be used for various sensors.

In Chapter 1, it was established that multifunctional ZnO and its nanostructures possess unique properties that are particularly suitable for biosensor technology. To summarize

(i) <u>Sensitivity to Various Chemical Species:</u> ZnO is highly sensitive to various gases and liquids such as CH_4, CO, H_2O, H_2, NH_3, trimethylamine, ethanol and NO_2 [2-3].

(ii) <u>Biocompatible Oxide:</u> ZnO and its ternary alloy, $Mg_xZn_{1-x}O$ are known to be the biocompatible oxides, in which Zn and Mg are important elements for neuroetransmitter production and enzyme function [4]. ZnO nanostructures are also compatible with intracellular material and are highly sensitive to pH changes inside cellular environments [6] with Mg $Mg_xZn_{1-x}O$ having a large range of pH compatibility. ZnO nanostructures are also considered as a coating material for medical implants [5].

(iii) <u>Tunable Material Properties:</u> ZnO nanostructures with different morphologies (nanometer-scale rods, belts, tips, etc) can be grown on various substrates including Si, quartz, glass, and metals.

(iv) <u>Functionalizability for Selective Detection:</u> To further increase the variety of molecular species that can be detected, ZnO nanostructures can be functionalized to bind with a large number of biomolecules. These include the detection of enzymatic reactions [7], proteins, antibodies, and DNA through the proper surface functionalizations [8,9,11,19].

(v) <u>Controllable and Reversible Surface Wettability:</u> The control of the surface wettability of ZnO nanotips between the super-hydrophillic and super-hydrophobic states are used to dramatically enhance the sensitivity of the biosensors [20], and significantly decrease the liquid analyte intake.

ZnO and its nanostructures can also serve as the basic sensing platform for detection of biophysical activity of larger bio-species such as cells, bacteria, and viruses.

The variation in morphology of the ZnO nanostructured surfaces can impact the attachment of certain biological cell lines (i.e., NIH 3T3 fibroblasts, umbilical vein endothelial cells, and capillary endothelial cells) and control the extent of cellular adhesion [21]. ZnO nanostructures were also used to bind with bacterial and viral cultures for reaction with enzymes and antibodies for applications in immunosensing [22,23]. ZnO nanostructures have also been employed in intracellular measurements where ZnO nanotips were used as coatings for microprobes or serve as the probes themselves. These intracellular probes can sense conductivity changes due to the ZnO coating's reaction to various target biochemicals within the cellular environment. This setup was used widely for pH determination of intracellular environments which was first reported by [5]. More recently, microtubes coated with ionophore-functionalized ZnO nanorods were used as an intracellular probe to selectively sense the Ca^{2+} ions within the cell membrane [24]. This selective binding with ZnO nanorods causes the probe tip to measure the voltage gradient between the membranes, and consequently giving a highly accurate measurement of intracellular pH levels. A similar method was also reported to determine the membrane potential across a human fat cell [25]. The use of ZnO nanorods as fluorescence enhancing substrates has been reported where biomolecular detection sensitivity of sub-picomolar and attomolar levels was obtained by using a conventional fluorescence microscope [26]. This ultrasensitive detection was due to the presence of ZnO nanomaterials which contributed greatly to the increased signal-to-noise ratio of biomolecular fluorescence. Moreover, E. coli cells were monitored optically through surface enhanced Raman spectroscopy by introducing ZnO nanoparticles into the cells to increase the optical signal [27].

2.2.2. Biofunctionalization and Bio-interfacing of ZnO

The design of a smart multifunctional ZnO-based biosensing platform is due to three important components of ZnO's properties: (i) reversible wettability control, (ii) bi-functional biochemical binding (serves as both active biological attachment and optical platform i.e. fluorescence emission), (iii) nanostructure morphology control. These controllable properties can be tailored to simultaneously enhance and optimize liquid sample intake, biochemical sensitivity and selectivity, and biospecies binding and distribution.

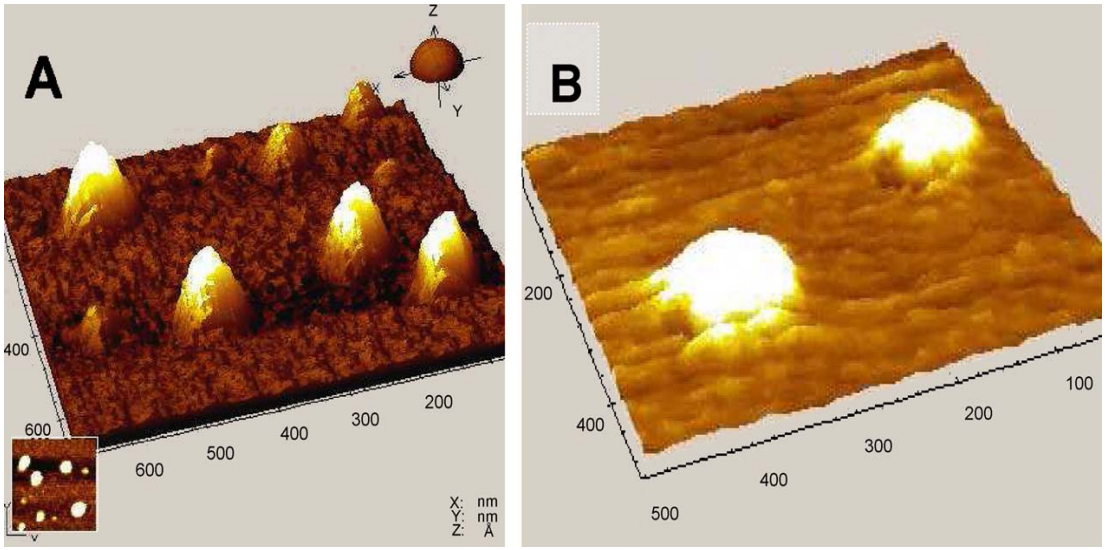

Fig. 2.1. Direct physisorption of glucose oxidase on porous ZnO nanostructures (a) before and (b) after biochemical binding. (Ref. [28])

<u>Biofunctionalization of ZnO: Linkage Chemistry</u>

Biofunctionalization is a critical issue for ZnO nanostructured surface to obtain the high sensitivity and selectivity to various types of biospecies. One method of activating ZnO to bind with a set of target biomolecules is direct physisorption of the receptor molecules onto the ZnO nanostructures. A good example of this technique is

demonstrated by Z. Dai et al. [28] where glucose oxidase was directly physisorbed onto porous ZnO nanostructures. The ZnO samples were grown using wet chemistry method and then immersed in the receptor solution (glucose oxidase). Fig. 2.1 shows the atomic force microscope (AFM) image of the ZnO surface before (a) and after (b) the direct physisorption. The direct physisorption method features a very simple chemical binding method but the binding quality is not stable, as after rinsing, a large percentage of the linker molecules are washed away.

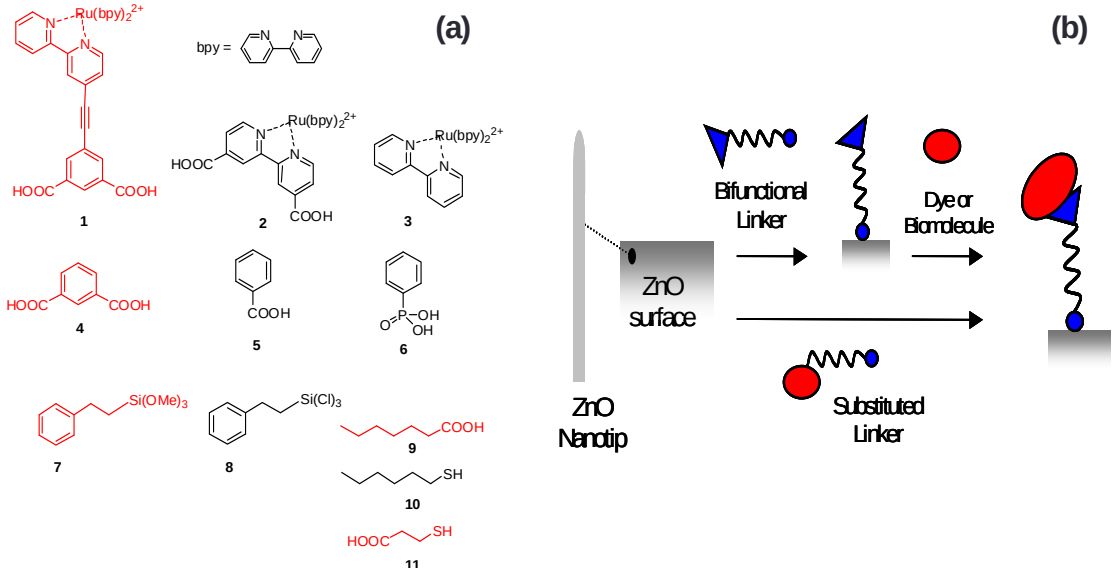

Fig. 2.2. (a) Compounds employed in the binding study. The compounds that did bind to the ZnO nanotips are shown in red. (b) The schematic of the functionalization of ZnO nanotip using bifunctional linker. (Ref. [9])

A more stable biofunctionalization method is done through development of bifunctional linkage chemistry. The binding properties of a number of small molecules with functional groups are reported to form covalent bonds with metal oxides nanoparticles (including ZnO): [29] COOH, SH, $SiOMe_3$, $SiCl_3$, and $PO(OH)_2$. The

structures of the compounds are shown in Fig. 2.2(a) [9]. To achieve the selective biochemical attachment to the ZnO nanostructures, a family of linkers called bifunctional linkers are employed, having one functional group that attaches to the ZnO nanotip surface while leaving other end available for further biological functionalization. The surface functionalization could be done in one step by using a functionalized linker, as represented in Fig. 2.2(b) [9]. The ability to functionalize the nanotips would lead to numerous applications, for instance, new ZnO-based integrated, multimode and multifunctional sensor technology to achieve higher accuracy and selectivity than existing sensors. The binding experiments indicate that the carboxylic acid group (COOH) is the most stable anchoring group for binding to the ZnO-N but that the number and position of the COOH groups, the acidity of the anchoring group, and solution pH also play a role in the binding. Another potentially useful, but flexible, bifunctional linker is 3-mercaptopropionic acid since it did bind to ZnO with its COOH end, leaving the SH group available for selective binding with various biomolecule targets. Increased resistance to acids can also be obtained by alloying ZnO with MgO (5-10%). MgZnO films are a novel material that exhibits increased stability toward acidic linkers, while staying identical to the ZnO in other respects. Alloyed films could therefore be employed with a larger variety of binding groups and at wider pH ranges.

There is another anchor group for ZnO that has been reported by R. Yakimova et al. [30] called organosilanes. This linker family has the advantage of having the reactive functional group that is more versatille for multi-species immobilization.

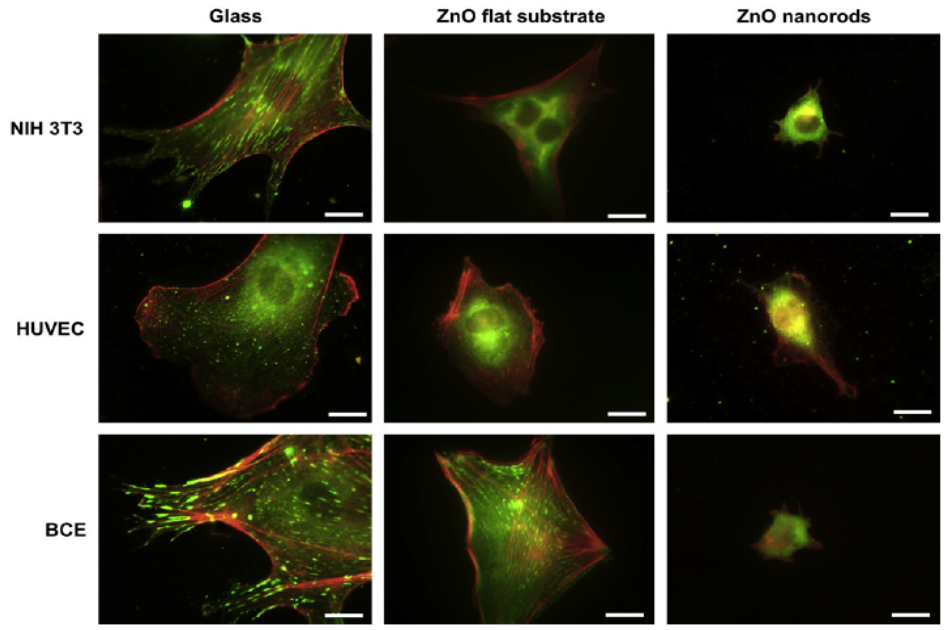

Fig. 2.3. Adhesion and spreading of various cell lines growing on ZnO of various surface morphologies. (Ref. [5])

Biointerfacing with Living Species

In addition to binding with various biochemical, ZnO has been shown to sustain an interface with living biological species such as cells and tissue cultures. ZnO nanostructured surfaces with the proper adhesion precipitator can facilitate the attachment of certain biological cell lines (i.e., NIH 3T3 fibroblasts, umbilical vein endothelial cells, and capillary endothelial cells) and control the extent of cellular adhesion [5]. ZnO nanostructures were also used to bind with bacterial and viral cultures for reaction with enzymes and antibodies for applications in immunosensing [22]. Fig. 2.3 shows the fluorescence microscope images of different cell lines attaching and spreading on various ZnO nanostructured surface morphologies. The level of pH sensitivity on ZnO also introduces issues about the toxicity of the ZnO nanostructures to the biospecies being

detected. A. E. Nel, et. al. [31] presented a study of where they observed pure ZnO releases cyto-toxic Zn^{2+} outside the pH range of 4.0-5.5. The size and morphology of the nanostructure also affects toxicity. Therefore, in designing the sensor platform, one must consider the pH levels of the analyte or employ MgZnO in place of pure ZnO since it has a larger range of pH levels compatible to living cells. Fig. 2.4. shows the mechanism of producing Zn^{2+} that causes the toxicity of ZnO with living biospecies.

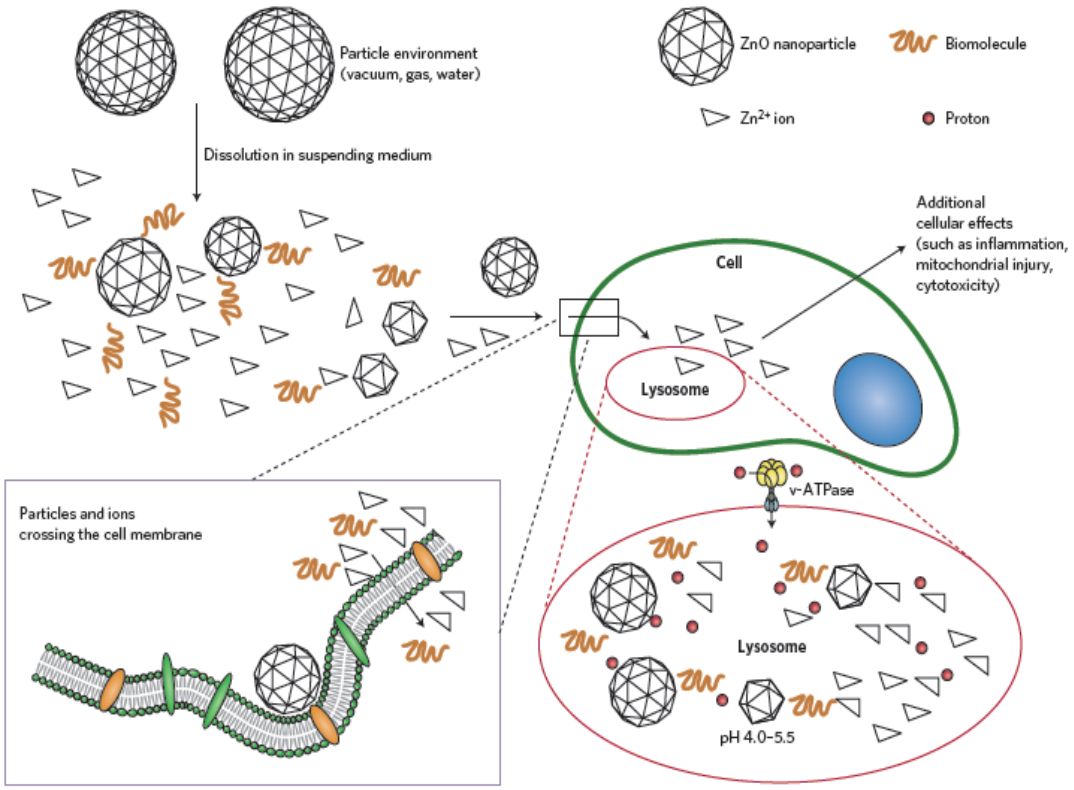

Fig. 2.4. Mechanism of toxicity produced by ZnO nanoparticles inside a cellular environment. (Ref. [31])

2.3. ZnO Based Biosensors and Bio-platforms

The existing devices and platforms used primarily for biosensing that are based on ZnO films and nanostructures can be classified according to their modes of operation.

Because of the multifunctional properties of ZnO, it is possible to design biosensors that could perform in acoustic mode (using the piezoelectric properties of ZnO), electric or amperometric biosensors (using the semiconductive properties of ZnO), and optical mode (using the transparent and conductive properties of ZnO). It is the goal of this proposal to be able to design ZnO-based biosensors that integrate these modes in a single platform.

2.3.1. Acoustic Mode Biosensors

Acoustic wave devices have been in commercial use for more than 60 years. The telecommunications industry is the largest consumer, primarily in mobile cell phones and base stations. These are typically surface acoustic wave (SAW) devices, and act as bandpass filters in both the radio frequency and intermediate frequency sections of the transceiver electronics. Several of the emerging applications for acoustic wave devices as sensors may eventually equal the demand of the telecommunications market. These include automotive applications (torque and tire pressure sensors), medical applications (chemical sensors), and industrial and commercial applications (vapor, humidity, temperature, and mass sensors). Acoustic wave sensors are competitively priced, inherently rugged, very sensitive, and intrinsically reliable. Some are also capable of being passively and wirelessly interrogated (no sensor power source required). The acoustic wave sensors typically come in two main categories: surface acoustic wave (SAW) and bulk acoustic wave (BAW) sensors. The signal transduction mechanism for the SAW is through the perturbations in the transverse components of the travelling waves on the surface of the piezoelectric layer of the device. For the BAW devices, the signal transduction is detected from the perturbations in the longitudinal waves

resonating within the piezoelectric layer of the device. With the integration of ZnO nanostructures on the sensing area of these devices and the proper biofunctionalization protocol, these acoustic wave devices can be transformed into highly sensitive and selective biosensors. A novel SAW biosensor built on a piezoelectric material ($LiNbO_3$) has been demonstrated. ZnO and MgZnO nanotips were integrated onto the sensing area and bio-functionalized to enabling it to optimally bind with oligonucleotides [19]. The SAW signals were measured after DNA oligonucleotide immobilization to determine mass loading which is detected by phase shift peak and insertion loss reduction as shown in Fig. 2.5. The advantages offered by this biosensor is the compact and portable design, high sensitivity, and low power consumption.

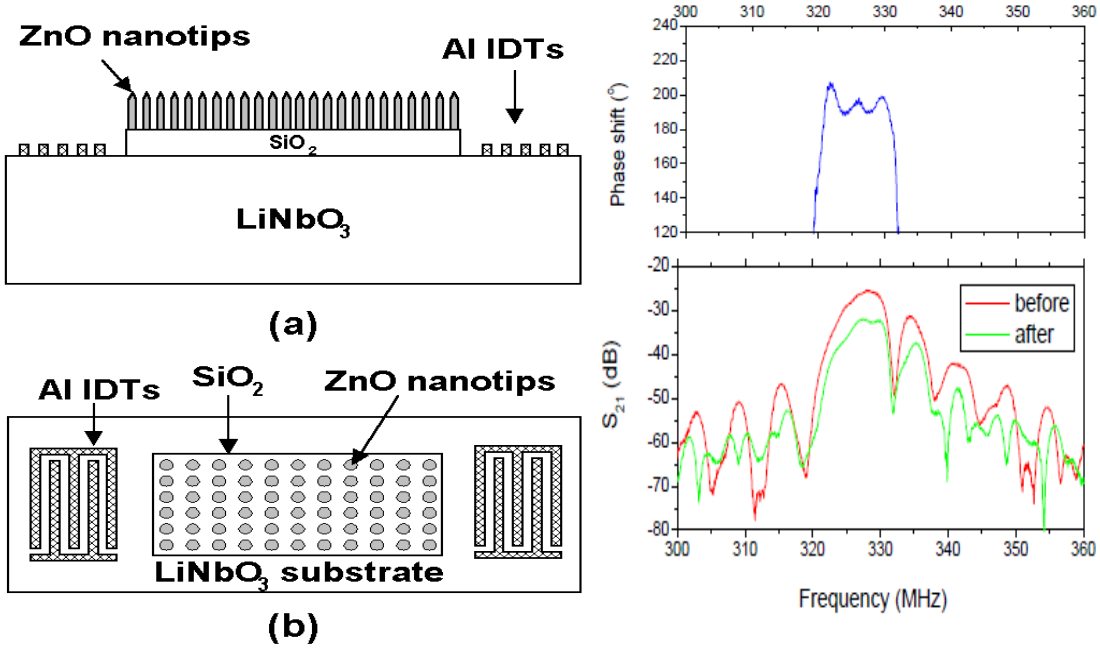

Fig. 2.5. Schematic of the ZnO nanotip-based SAW biosensor structures: (a) cross-section, (b) top view. (c) The phase shift peaks at the operation frequency, and (d) a reduction in transmission spectrum amplitude results after mass loading of the detected biomolecules. (Ref. [19])

A BAW biosensor has been demonstrated based on a thin film resonator based on piezoelectric ZnO or MgZnO film sandwiched between two metal electrodes on a Si substrate. ZnO nanotips deposited on the top electrode were bio-functionalized to specifically bind with DNA and detect the immobilization and hybridization to complement DNA strands. A shift in resonant frequency due to DNA binding and complementary DNA hybridization was detected [11]. Moreover, this sensor's operating frequency can be tuned by changing the Mg composition of the piezoelectric MgZnO film. Another BAW device that has been used as a biosensor is the ZnO surface modified quartz crystal microbalance (nano-QCM). ZnO nanotips are directly grown on top of the QCM sensing electrode. The ZnO nanotips are then bio-functionalized with the appropriate linker molecule that would selectively adhere with the target biochemical. The surface modified ZnO nanotips significantly enhance the sensitivity and selectivity over the conventional QCM. The utilization of the nano-QCM as a biosensor was demonstrated through the detection of DNA immobilization and hybridization [20].

Sensing biochemicals is not the only function of the ZnO-based acoustic wave devices. Biosensing platforms also require other functions like transporting, mixing and storage of liquid microsamples. These functions will lead to the ultimate biosensing system on a single chip. A ZnO-based SAW device was reported to perform mixing and transporting a mico-droplet [32] on a silicon chip. This ZnO-SAW micromixer consists of a 2μm thick piezoelectric Zn film deposited on a Si chip with Au interdigital transducer (IDT) on the top surface. An oscillating voltage with 80V peak value was introduced into the IDT to cause transverse components of the SAW wave to agitate a

microdroplet for mixing and transporting it to another end of the chip as shown in Fig. 6(b-d).

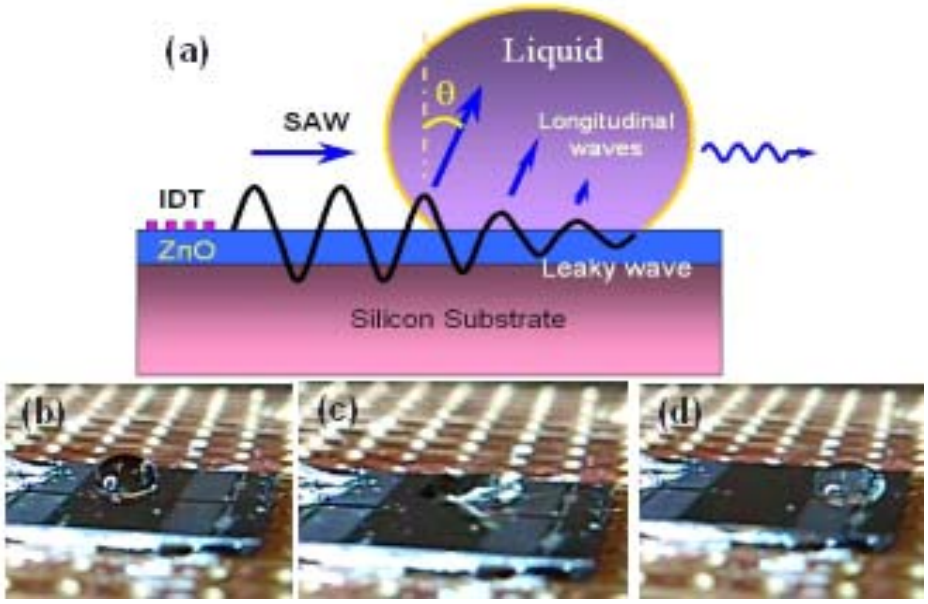

Fig. 2.6. (a) Schematic of the ZnO-based SAW micromixer, (b-d) water microdroplet being agitated and transported from left to right end of the chip. (Ref. [32])

2.3.2. Electrical Mode Biosensors

Another family of biosensors based on ZnO operates in the electrical mode. These sensors use conductivity-based measurements due to the modulation of current flowing though the semiconductive ZnO films and nanostructures that is modified by the detected biomolecules. Among the reported electrical mode ZnO-based biosensors are (i) potentiometric micro/nano probes, (ii) amperometric ZnO-platforms, and (iii) field-effect transistor (FET)-based sensors.

The potentiometric micro/nano probes consists of a pair of electrodes (either metallic or glass microcapillaries), one of which is coated with ZnO nanotips and the

other one is uncoated (reference electrode). The electrode with the ZnO nanotip coating is biofunctionalized to bind specifically to a target biomolecule. The electrode pair is then immersed in the liquid analyte. The target molecules migrate to the biofunctionalized ZnO-coated electrode, causing a potential difference between the electrode pair, which is proportional to the concentration of the target molecules in solution. Fig. 2.7 shows the various potentiometric sensors. M.Q. Israr *et al.* [33] reported cholesterol detection using Ag microwires coated with ZnO nanotips while M.H. Asif et al. [34] demonstrated a glass microcapillary coated with functionalied ZnO nanotip intracellular probes that detects the pH levels of the cytoplasm.

Fig. 2.7. Various potentiometric ZnO-based micro/nano probes used for inctracellular pH sensing. (Refs. [33 34])

Amperometric ZnO-based platforms typically consist of a layer of semiconductive ZnO nanowire or nanoparticles with two electrodes deposited on the top. The exposed ZnO layer is biofunctionalized for specific binding with the target molecule

and the I-V curve of the platform before and after detection is measured just like a diode circuit would be characterized. The amount of current changes according to the conductivity modulation of ZnO due to the binding molecules. Several amperometric ZnO platforms have been reported such as the nanowire-based Schottky biosensor by Z. L. Wang, et al. [35], and the functionalized ZnO nanocomb platform by Wang et al. [36], all of which register current density modulation as a function of analyte concentration. Pradhan et al. [37] on the other hand demonstrated an amperometric biosensor with ZnO nanowires deposited on Au-coated flexible substrate. Fig. 2.8 shows the typical device structures of the reported amperometric sensors and their mechanism of signal transduction.

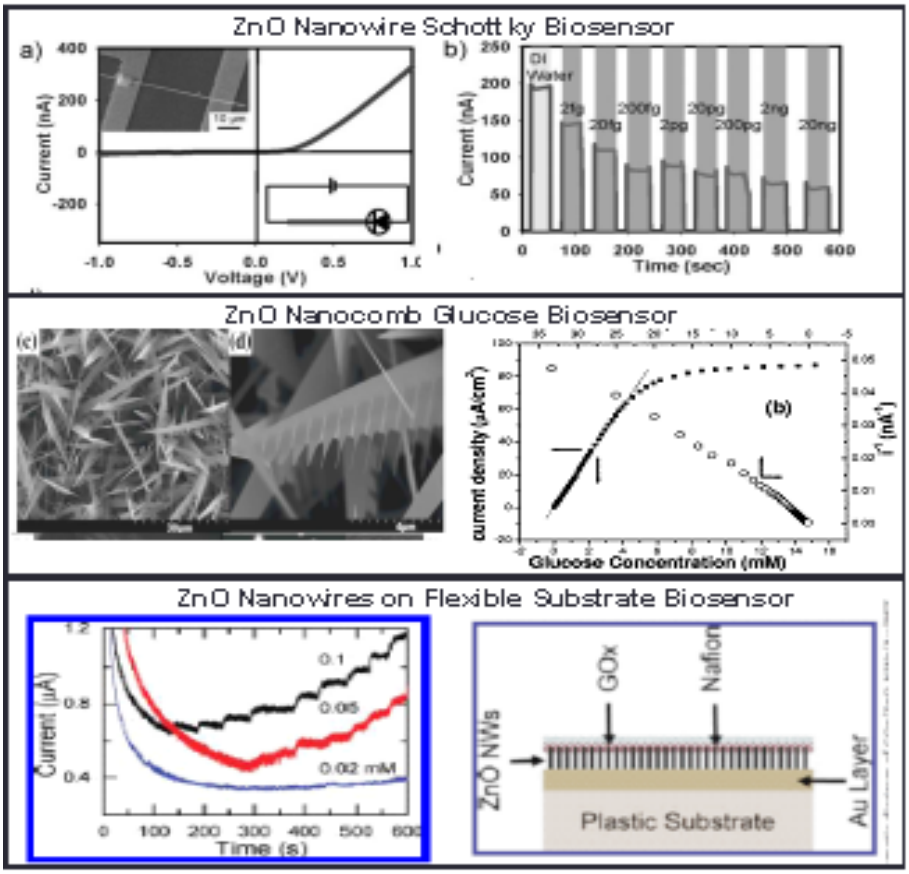

Fig. 2.8. Various amperometric biosensor platforms based on various ZnO nanostructures. (Refs. [35, 36, 37])

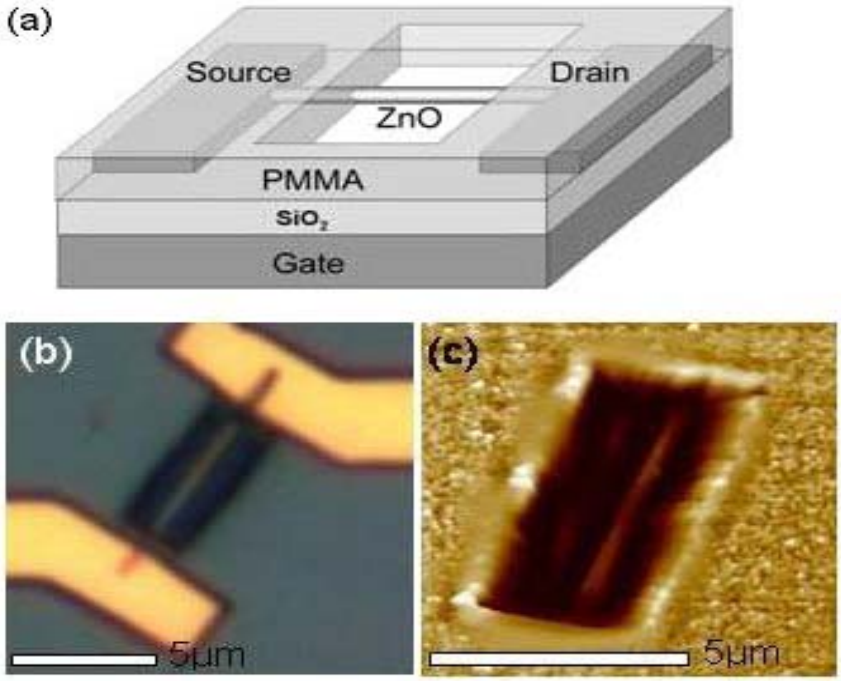

Fig. 2.9. Typical structure of the ZnO nanowire-based FET biosensor. (Ref. [38])

Currently, the ZnO FET-based biosensors consist of ZnO nanowire serving as the FET's channel. These sensors are demonstrated with high sensitivity reaching the order of fM [38,39,40]. The current modulation is monitored before and after the target molecules have been immobilized onto the exposed biofunctionalized ZnO nanowire channel. Fig. 9 shows a typical device structure of the ZnO nanowire FET biosensor. These devices have very high sensitivity, however, these prototypes of sensors generally involve a complex fabrication process as they are constructed individually by manipulating and aligning a single strand of semiconducting nanowire as the FET channel between the source and drain patterns. It is difficult to achieve repeatability and manufacturability in fabrication and integration of these devices for larger sensor arrays. Recently, a ZnO-based thin film transistor biosensor (bio-TFT) was demonstrated. It consists of an enhancement-mode bottom-gate MOSFET with an exposed ZnO channel

serving as the active sensing area. The bio-TFT has an on-off ratio of 10^8, and achieved a sensitivity of 10fM detection of epidermal growth factor receptor (EGFR) proteins that are important proteins expressed by breast cancer cells [41].

2.3.3. Optical Mode Biosensors

The main role of ZnO nanostructures in optical biosensors is the enhancement of the optical emission due to the light-gathering properties of the nanostructures. Usually, the ZnO nanostructures in this case serve a dual purpose: the biochemical binding layer and the optical signal enhancer. W. Hu et al. [42] demonstrated a ZnO nanowire enhanced fluorescence emission biosensor. The platform consisted of an array of antibody droplets on ZnO nanostructures and on glass substrate. The antibodies on the glass substrate has amplifying fluorophores while the ones on the ZnO nanostructures do not have amplifying fluorophores. The fluorescence micrographs of both platforms show the same fluorescence emission levels as shown in Fig. 2.10.

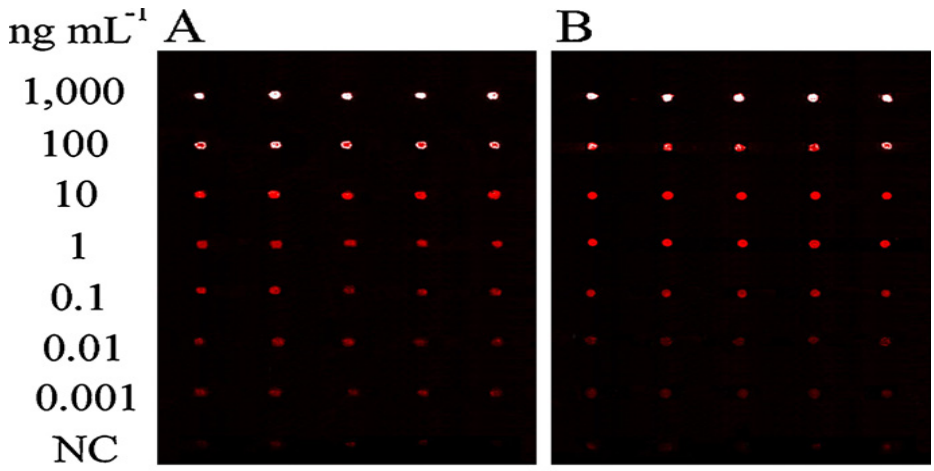

Fig. 2.10. Fluorescence emission of antibody array with various concentrations with (a) amplifying fluorophores and no ZnO, (b) with ZnO nanostructure layer without amplifying fluorophores. (Ref. [42])

X. Hong et al. [43] showed that Fe-doped ZnO can greatly enhance the Raman shift signal in an immunosensor platform coated with Fe:ZnO nanoparticles. The femto-Molar level sensitivity to the detection of human IgG antibodies has been attained through the enhancement of the Raman shift signals facilitated by the Fe:ZnO nanoparticles as shown in Fig. 2.11.

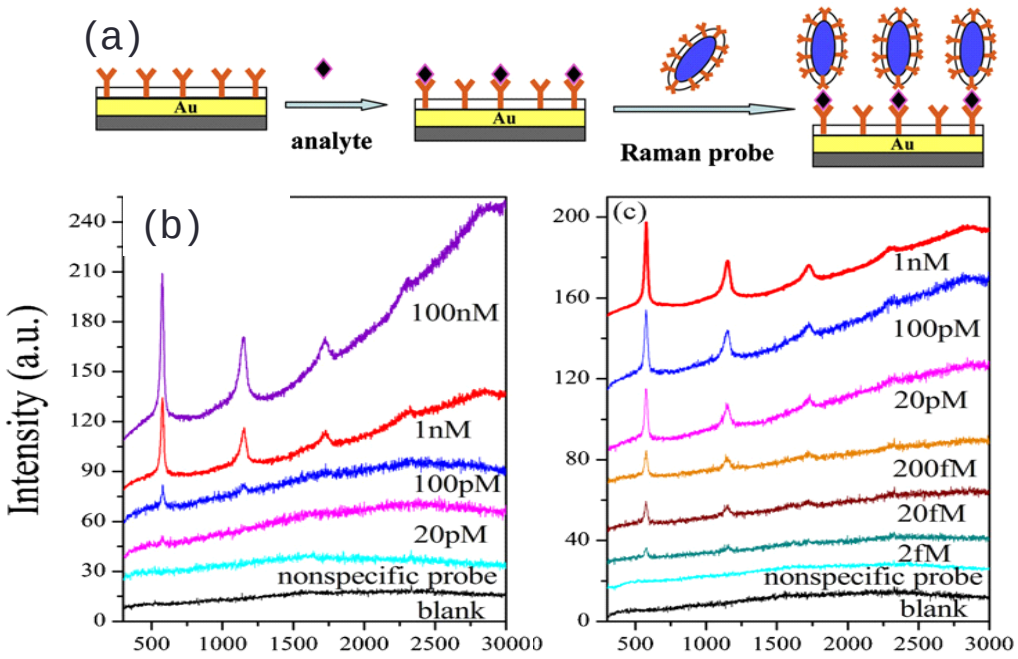

Fig. 2.11. (a) Fe-doped ZnO Raman-based optical sensor schematic, Raman shift of the sensor (b) without Fe:ZnO, and (c) with Fe:ZnO. (Ref. [43])

ZnO thin films have also shown promise in application with surface plasmon resonance-based biosensing. C. de Julian Fernandez *et al.* [44] reported that ethanol detection through surface plasmon resonance has enhanced through coating the gold surface of the sensor with a ZnO thin film. The plasmon reflectance spectrum exhibited a higher value with the ZnO thin film as compared to the bare gold surface when ethanol vapors are introduced (Fig. 2.12).

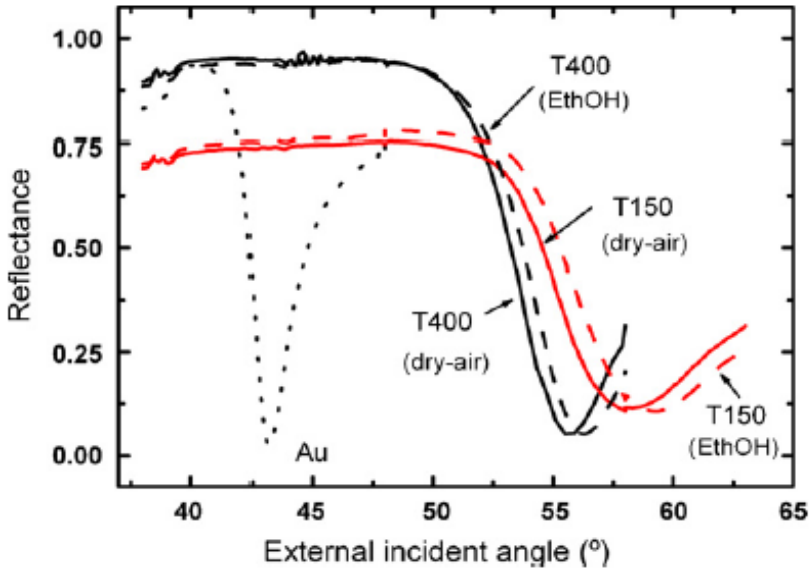

Fig. 2.12. (red lines) Surface plasmon resonance without ZnO film (black lines) Raman shift of the sensor with Fe:ZnO film. (Ref. [44])

2.4. Generalized Approach to ZnO-based Biosensor Development

In this dissertation we take the following generalized approach to develop the ZnO-based biosensors. The general sensor building roadmap for this research is schematically shown in Fig. 2.13. The biosensor development technique consists of three major components:

(i) ZnO nanostructure growth including morphology control and surface wettability control for the creation of the bio-interface template. (Fig. 2.13 Box A) This component also includes the growth of ZnO thin films on various substrates to serve as the active material (piezoelectric and semiconductive) for the core sensor devices.

(ii) Bio-interfacting of the ZnO nanostructure template using our developed biofunctionalization protocols (Fig. 2.13 Box B). In this research, various protocols have been studied for the specific binding of DNA/oligonucleotides, cells, and antibodies.

(iii) Fabrication and characterization of the multifunctional ZnO-based core devices (Fig. 2.13 Box C). These devices will serve as the basic sensor platform. The integration of the ZnO nanostructured bio-interface with these core devices will complete the ZnO-based biosensing system. The output of these biosensors will take the form of multiple modes, i.e., electrical, acoustic, or optical.

It will be observed that in this generalized approach to ZnO-based biosensor development, ZnO performs a dual role in the biosensor system. Firstly, it performs the basic function as the active material for the device (piezoelectric or semiconductive) that provides the signal transduction for the sensor (acoustic or electrical). Secondly, ZnO nanostructures serve as the link between the inorganic layer, and the organic layer of the biosensor system. This dual role of ZnO establishes it as a versatile material with unique properties that can pave the way for future biosensor paradigms.

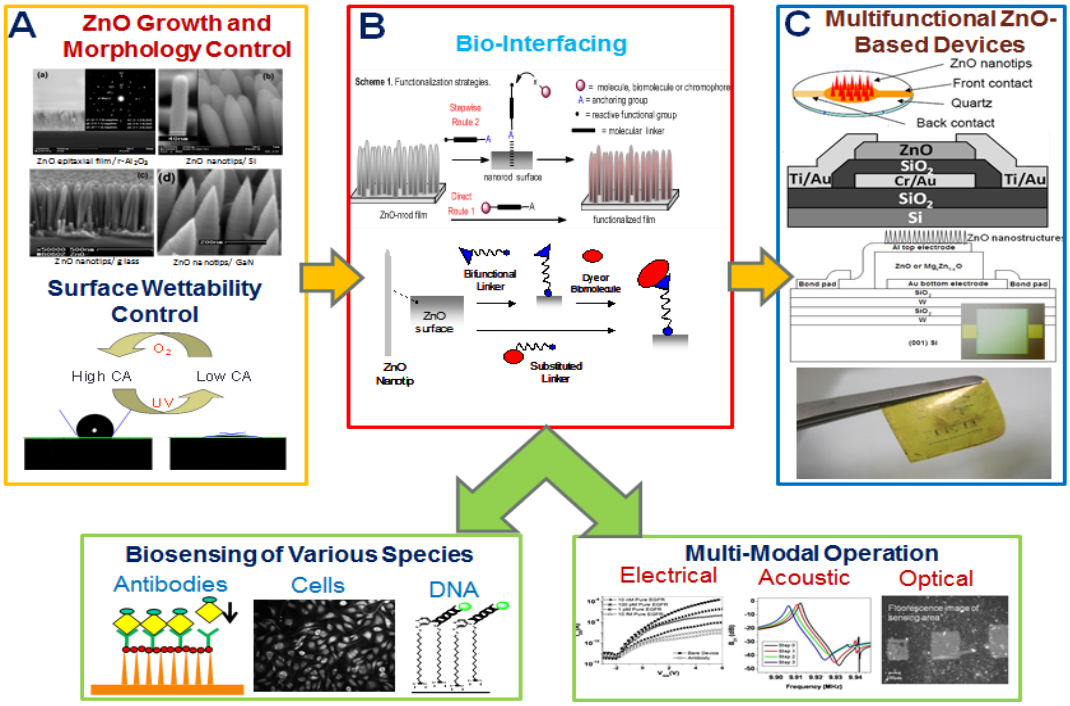

Fig. 2.13. Schematic of the generalized approach adopted for the ZnO-based biosensor development.

2.5. Summary and Challenges

In summary we have shown that

- ZnO and its nanostructures is a highly suitable material for biosensor design
- The multifunctional properties of ZnO have established it as a suitable biosensing material. This paves the way for development of sensors with good biocompatibility, functionalizability, sensitivity and selectivity enhancement.
- Single-device sensor designs operated in various modes (electrical, acoustic and optical) have shown great promise in meeting the challenge of enhanced figures of merits and design issues.
- ZnO is an excellent material that interfaces the biological layer to the inorganic layer

Challenges for future biosensor design:

- Multimodal operation in a single platform.
- A 3-Dimensional organic-inorganic biointerface (2D film device platform + 1D nanostructured array).
- Integrated devices to form high throughput arrays in a single chip

Chapter 3

Bio-interfacing ZnO Nanostructures for Biosensing Platforms

As mentioned in Chapter 2, the quality of the design of the biosensing device depends on the sensitivity and selectivity of the active sensing layer of the device. For ZnO-based devices, sensitivity and selectivity relies on the optimized surface biofunctionalization. Firstly, we developed a series of biofunctionalization schemes/protocols and surface treatments for ZnO nanostructures to accomplish the optimized binding with (i) DNA/oligonucleotides, (ii) monoclonal epidermal growth factor receptor antibodies (EGFR mAbs), and (iii) bovine aortic endothelial cells (BAEC). Next we investigated the effects of surface morphology of ZnO nanostructures on the quality of binding of DNA and on the quality of cellular adhesion and proliferation.

3.1. Functionalization of ZnO Nanostructures for Biochemical Binding

In this section we discuss the chemical protocols that we have developed for ZnO to specifically bind with (a) DNA/oligonucleotides and (b) EGFR mAbs. We employed a stepwise functionalization method to accomplish the biochemical binding, which consists of three general steps: (i) attachment of the bifunctional linker based on carboxylic acid (COOH) functional group as the covalent anchor molecule to ZnO on one end, and an open-ended functional group on the other end; (ii) the receptor molecule that is responsible for the attachment of the target biomolecule to ZnO is bonded to the open-ended functional group of the bifunctional linker; finally (iii) the target biomolecule is reacted with the reception molecule.

3.1.1. Stepwise Biofunctionalization for DNA Immobilization and Hybridization on ZnO Nanotips (Ref. [45])

Two DNA immobilization methods were developed to bind with ZnO nanostructures as illustrated in Fig. 3.1. In both cases a bifunctional carboxylic acid was first anchored to the MOCVD-grown ZnO nanotips films surface by the COOH group, leaving a second reactive functional group, temporarily protected to avoid reaction with the ZnO surface, available for reaction with DNA. In Fig. 3.1-Route A, the surface that was functionalized with pyridyl disulfide was then reacted with thiol-modified 16 base ssDNA, and in Fig. 3.1-Route B, the *N*-hydroxysuccinimide-ester end group was reacted with amino-modified 16 base ssDNA. The DNA-functionalized ZnO nanotips films were hybridized with complementary 5′-fluorescein-modified ssDNA.

DNA Immobilization via PDHA layer (Route A): Bifunctional carboxylic acid 16-(2-pyridyldithiol)hexadecanoic acid (PDHA) was bound to ZnO nanotips by immersing the ZnO samples in 2 mM solutions of the acid in 1-butanol/ethanol (Step 1, Fig 3.1-Route A). Reaction of the pyridyl disulfide with an aqueous solution of 16 bases 5′-thiol-modified ssDNA (GTGTTAGCCTCAAGTG), deprotected prior to use by reaction with a DTT-resin, in PBS buffer (phosphate buffer saline, pH 7.4) (Step 2, Fig 3.1-Route A) resulted in a thiol-disulfide exchange reaction. The hybridization step to form dsDNA-functionalized ZnO nanotips films (Step 3, Fig 3.1-Route A) was performed by immersing the DNA-substituted ZnO films in an aqueous solution of complementary Fl-ssDNA in a pH 7.4 buffer (PBS). The hybridization step was monitored by fluorescence emission spectra ($\lambda_{excitation}$ = 490 nm, $\lambda_{emission}$ = 520 nm), by

detecting the presence of the fluorescent label (Fl = fluorescein) which was attached to the complementary DNA strand.

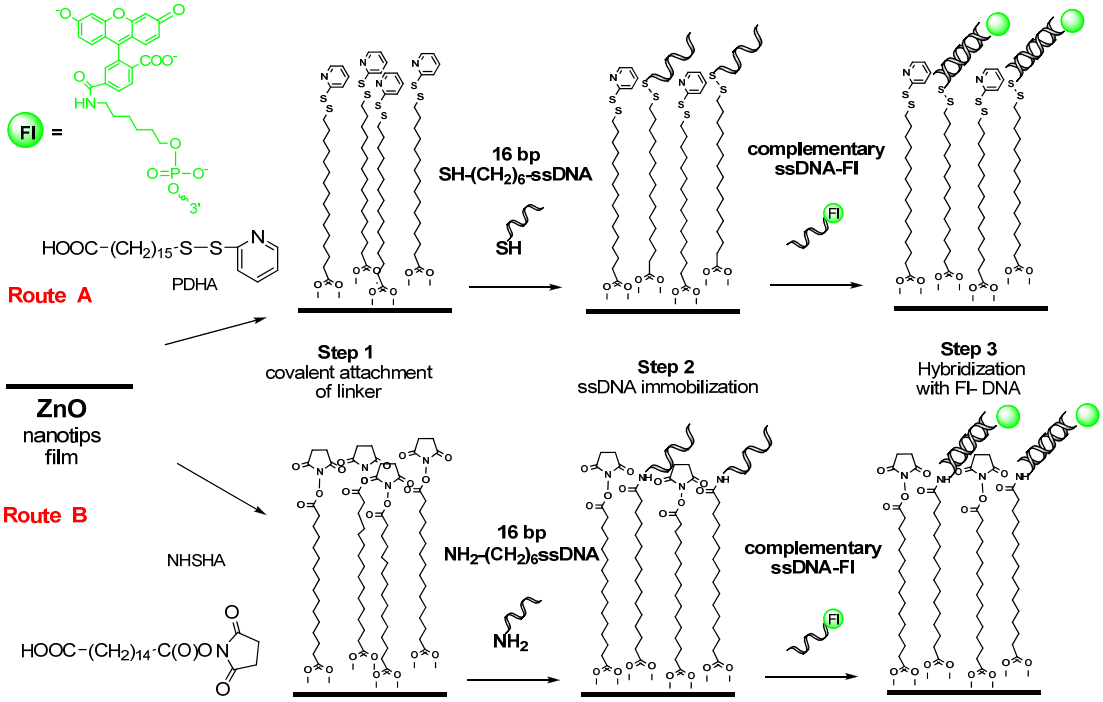

Fig. 3.1. ZnO nanotips surface modification via route A: thiol-disulfide exchange reaction, and route B: NHS-ester hydrolysis reaction. (Ref. [45])

DNA Immobilization via NHSHA layer (Route B): In Route B, a different end group was used for the fatty acid bound to ZnO nanotips surface to react with an amino-substituted ssDNA, to demonstrate that the strategy of forming a receptor layer on ZnO nanotips surfaces can be extended to other functional groups and reactions. Bifunctional hexadecanoic carboxylic acid *N*-(15-carboxypentadecanoyloxy)succinimide (NHSHA) was bound by the COOH group to form a *N*-hydroxysuccinimide-ester functionalized surface that was reacted in a substitution reaction with 16 bases 5′-amino-modified ssDNA (GTGTTAGCCTCAAGTG) in experimental conditions similar to those reported

for Route A (Fig 3.1-Route B, Step 2). Finally, hybridization of the DNA-modified surface was performed with the same complementary Fl-ssDNA used in Route A (Fig 3.1-Route B, Step 3).

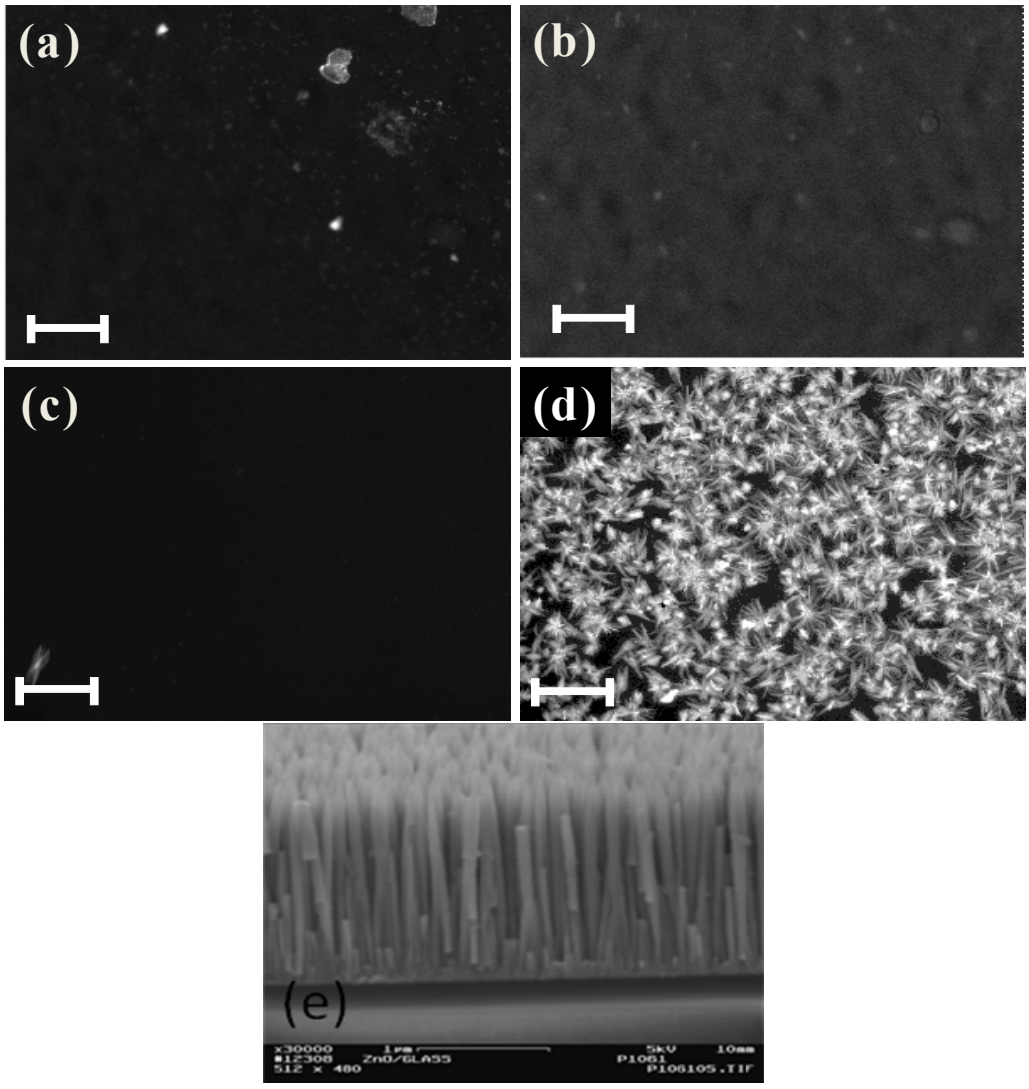

Fig. 3.2. Demonstration of selective DNA from the fluorescence images (bar is 100μm) of the ZnO nanotips grown on C-sapphire with (a) step 1 only, (b) step 1 + step 2 (c) step 1 + step 3, and (d) step 1 + step 2 + step 3. Only the nanotips with properly hybridized DNA molecules are positively fluorescing. (e) ZnO nanotips grown on glass used in the DNA functionalization studies (Ref. [8,45]).

We performed fluorescence imaging of the ZnO nanotips grown on glass subjected to various combinations of the steps outlined in routes A and B to confirm whether or not selective immobilization and hybridization was achieved. An Axiovert 200M confocal fluorescence microscope (Zeiss Axiovert 200M, Gottingen, Germany) was used with a 510 nm filter and 480 nm excitation to obtain reflection type fluorescence images of the ZnO nanotips. Figs. 3.2(a-d) show fluorescence images of the ZnO nanotips for different combinations of the three chemical steps: in (a) only step 1 is performed, in (b) only steps 1 and 2 are performed, in (d) only steps 1 and 3 are performed, and in (d) all three steps are performed in order. Only the nanotips with all the three complete steps are positively fluorescing which confirms the selective binding of the ZnO nanotips to the DNA molecules.

3.1.2. The role of the Buffer pH in the Linker Attachment to ZnO

Phosphate buffer saline (PBS) was selected over other buffers commonly used in this kind of step that contain COOH or other functional groups, which can displace the linker layer by binding to the ZnO nanotip films surface. Indeed, we observed competitive displacement of the linker layers in the presence of EDTA (ethylene diamine tetraacetic acid) and HEPES (4-(2-hydroxyethyl)-1-piperazineethanesulfonic acid), which are buffers commonly used in these reactions. An additional advantage of PBS is that it is isotonic and non-toxic to cells, properties that could be useful for future biosensing applications. In route B, buffers containing primary amines, such as TRIS (tris(hydroxymethyl)aminomethane hydrochloride), or glycine buffers were avoided,

because they contain amino groups that could compete with the amino group present on the ssDNA.

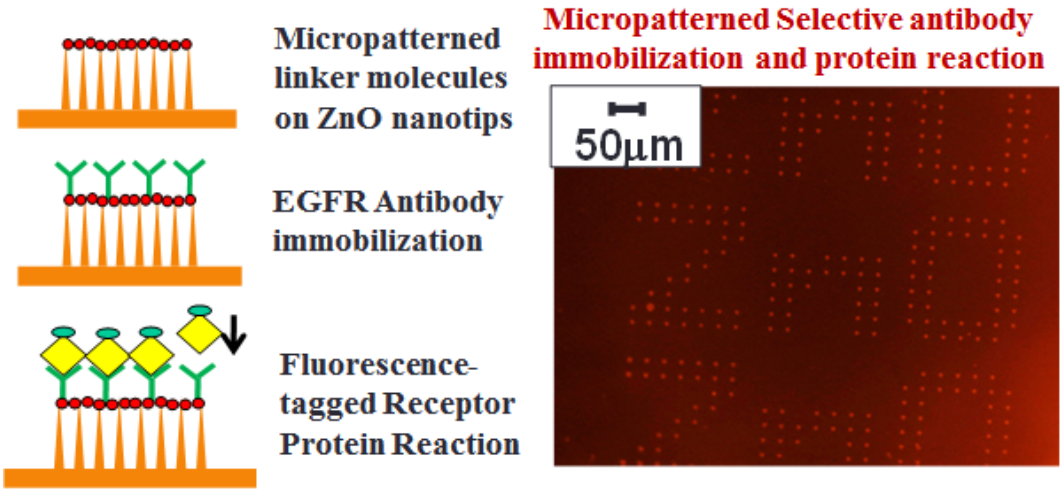

Fig. 3.3. Fluorescence image of the EGFR proteins that reacted with the immobilized EGFR antibodies on ZnO nanotips grown on glass.

3.1.3. Linkage Chemistry for Monoclonal EGFR Antibodies (mAbs EGFR) (Ref. [41])

We also developed a functionalization scheme for binding monoclonal EGFR antibodies (mAbs EGFR) to ZnO nanostructures and then reacting them specifically to its antigen protein. This chemical scheme involves three basic steps. First, the ZnO channel was functionalized with trimethoxysilane aldehyde (having a reactive aldehyde end group) by incubating the device in 1% v/v solution of the silane-aldehyde in 95% ethanol for 30 min. The device was then cured at 120°C for 15 min. Second, the aldehyde groups were coupled to the amine groups of the monoclonal EGFR antibodies (1:50) through reductive amination in the presence of 4 mM sodium cyanoborohydride in PBS (pH 7.4)

for two hours. Third, unreacted aldehyde groups were blocked using 100 mM ethanolamine in a similar manner to prevent non-specific interactions of proteins. Finally, the device was rinsed in a continuous flow of PBS, pH 7.4 for 10 min. Fig. 3.3 shows the fluorescence image of the nanopatterned EGFR molecules specifically binding to ZnO nanotips.

3.2. Cellular Adhesion via ZnO Surface Morphology Control [46]

It is critical to determine the most suitable ZnO nanostructure morphology to facilitate the optimal adhesion of the cells to the device. In order to determine the optimum morphology for the cell adhesion, ZnO nanostructures with three different surface morphologies were grown on 22 mm square glass cover slips (Fisher Scientific, Pittsburg, PA) by the metal-organic chemical vapor deposition (MOCVD) technique. Diethylzinc (DEZn) and ultra-high purity O_2 are used as the Zn precursor source and oxidizer, respectively. A chamber pressure of ~50 torr was maintained during growth and the substrate temperature varied from 250^{o}C to 500^{o}C. Three different surface morphologies ("flat", "rough", and "sharp") were prepared for this experiment by varying the substrate temperature during the MOCVD growth. It was found that the substrate temperature played the major role on achieving various surface morphologies of ZnO films. Figs. 3.2(a-c) show three different surface morphologies of ZnO films, taken by FESEM. The relatively flat surface, shown in Fig. 3.4(a), was grown at a low temperature of ~250^{o}C, while the relatively rough one (Fig. 3.4(b)) was grown at ~330^{o}C. The sample shown in (Fig. 3.4(c)), which will be referred to as the "sharp" surface required a relatively high temperature (>400^{o}C) for growth. The surface roughness (root mean

square) of ZnO films was characterized by AFM, which is 1.39 nm for flat ZnO (Fig. 3.4(a)), 7.48 nm for rough one (Fig. 3.4(b)) and 11.4 nm for sharp one (Fig. 3.4(c)). The three samples were treated with fibronectin which serves as the biochemical layer that facilitates initial cell anchorage to ZnO. The surface treated samples were then placed in a standard 6-well cell culture plate containing growth medium for BAEC cell seeding. The samples were incubated for an average of 50 hours in a standard CO_2 incubator.

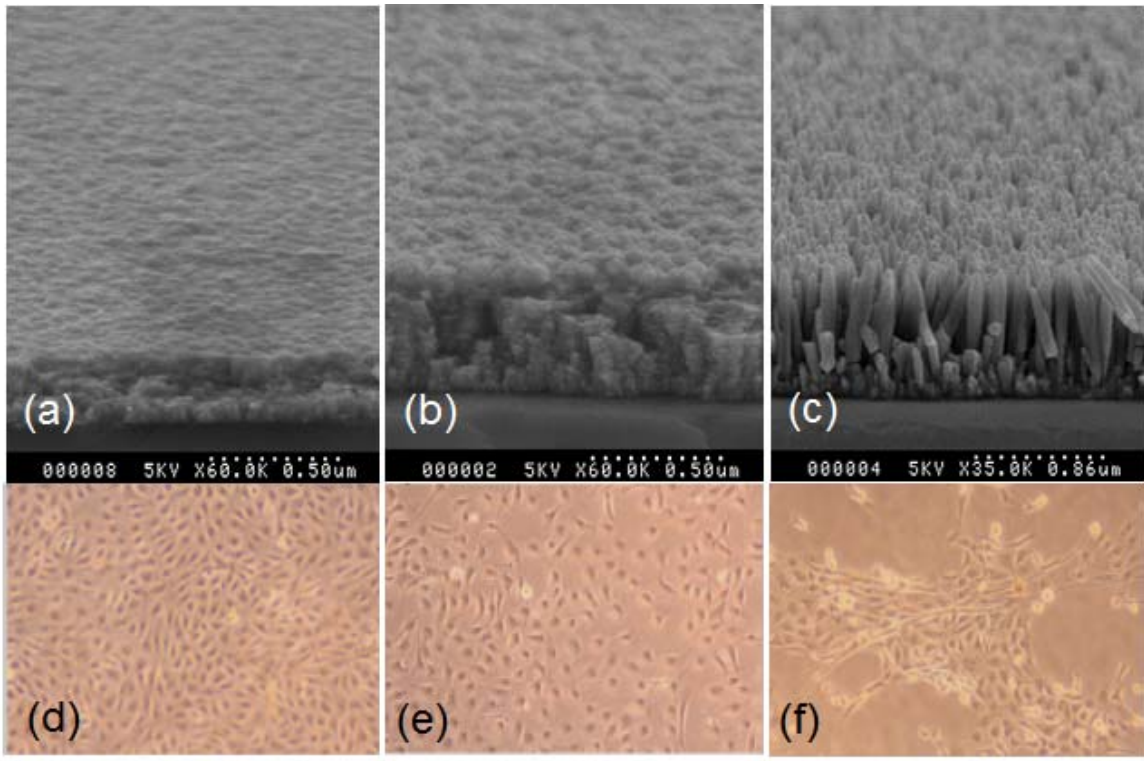

Fig. 3.4. The FESEM images of the different surface morphologies of ZnO nanostructures: (a) flat film grown on glass, (b) rough surface formed by dense nano-columns grown on glass (c) sharp nanotips grown on glass. These surfaces were treated with fibronectin and seeded with BAEC cells. Transmission type optical microscope images of the growing BAEC cells on (d) flat ZnO film, (e) rough surface of dense ZnO nano-columns, and (f) sharp ZnO nanotips. (Ref [46])

The standard transmission type optical microscope images of the three ZnO samples were taken after 60 hours of incubation. For the flat ZnO surface, the cell culture is close to 100% confluency and uniformly spreading and proliferating on the ZnO substrate (Fig. 3.4(d)). However, it is found that after the entire duration of the monitoring cycle the cells have crowded among with each other, competing for nutrients and space. This condition will eventually induce the cells to die and detach from the ZnO surface. On the other hand, the cells on the rough ZnO surface have reached about 75% confluency, uniform proliferation, and the individual cells have considerable amount of spreading as shown in Fig. 3.4(e). The cells adhered to the sharp ZnO surface, but did not establish good focal adhesion to facilitate uniform proliferation and proper individual cell spreading. The cell culture on the sharp ZnO surface only attained 40% confluency and a clumped cell distribution as shown in Fig. 3.4(f). This clumped distribution could cause localized areas on the ZnO surface where cell death is induced. The results of poor cell adhesion on sharp nanorods are consistent with the observation reported by J. Lee *et al*. [5] wherein the same cell line (BAEC cells) lacked the ability to establish strong initial adhesion to the sharp nanostructures, thus prohibited them to produce lamellipodia (cell-anchoring mechanism). In order to obtain a good cell culture for monitoring purposes, three components of cell growth need to be satisfied: (i) good initial cell adhesion, (ii) uniform cell proliferation, and (iii) considerably large individual cell spreading (Freshney, 2005). The flat and rough ZnO surfaces displayed all three while the sharp ZnO surface failed to fulfill the last two requirements. It would be a natural choice to use the flat ZnO surface since it gives us a large yield in cell growth while fulfilling all three cell culture requirements. However, there is an inherent tradeoff in

choosing the optimal ZnO morphology for the sensing surface. In terms of cell attachment, the cells favor the adhesion to flatter surfaces, but in terms of device performance the sharper surface provides the highest sensitivity due to the large effective sensing area provided by the nanostructures [8,10]. It is determined that the rough ZnO surface is the most suitable morphology for adhesion and viability for cell growth without sacrificing the device sensitivity.

3.3. Optimization of DNA Immobilization via ZnO Surface Morphology Control [47]

Using the same surface morphology control on ZnO nanostructures for cell adhesion, we did a study on the optimization of the ZnO surface morphology for DNA immobilization. For this case we utilized three ZnO morphologies similar to the ones used in Section 3.2. The FESEM of the three morphologies are shown in Fig. 3.5. ZnO Film-N consisted of columnar, perpendicularly aligned, ZnO nanorods about 0.5 μm long and 40 nm in diameter (Fig. 3.5(a)). ZnO Film-R exhibited a rough surface (Fig. 3.5(b)) and ZnO Film-P had a mostly planar surface (Fig. 3.5(c)). In all cases, the films were about 0.5 μm thick. The morphology was controlled by varying the growth temperature: ZnO Films-P were grown at ~250 $^{\circ}$C, Films-R were grown at ~330 $^{\circ}$C, and the nanorods required a relatively high growth temperature (> 400 $^{\circ}$C). In the nano-QCM, the ZnO-covered sensing area was exposed to UV light to make it super-hydrophilic.

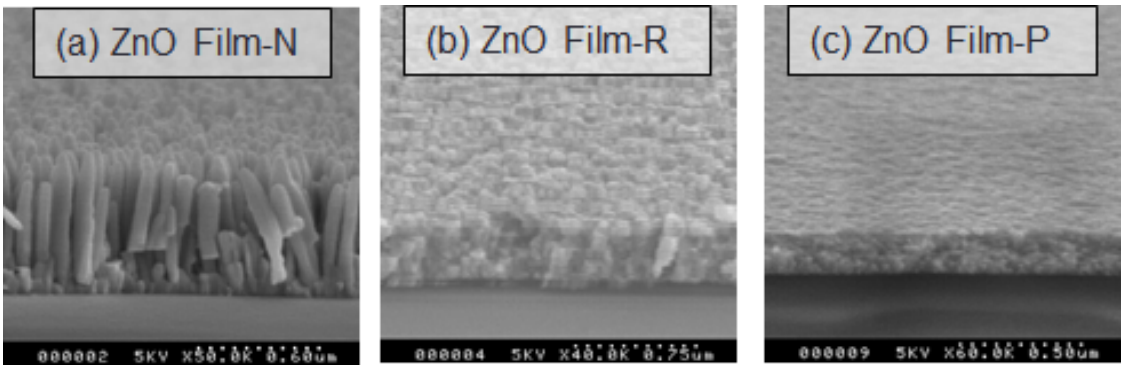

Fig. 3.5. FESEM images of 0.5 μm-thick MOCVD-grown ZnO films on glass with three different morphologies: (a) Film-N (Nanorods), (b) Film-R (Rough), (c) Film-P (Planar). Ref. [47]

The three-step functionalization of ZnO, illustrated in Fig. 3.6, followed the previously discussed methodology (Section 3.1). In Step A bifunctional linker 16-(2-pyridyldithiol)-hexadecanoic acid (PDHA) was bound to ZnO through the COOH group, leaving available for further functionalization a thiol group, protected as a 2-pyridyl disulfide, on the opposite end of the long saturated aliphatic chain. Step B involved a disulfide exchange with a thiol-substituted single stranded DNA (SH-ssDNA), which was obtained by *in situ* reduction of the commercially available ssDNA-S-S-ssDNA by treatment with DTT resin in in PBS buffer to form the free thiol. The resulting ZnO films, with ssDNA immobilized on the surface, were treated in Step C and Step D with complementary or non-complementary ssDNA tagged with fluorescein (ssDNA-Fl and ssDNA'-F, respectively). The presence of the fluorescent tag was useful for imaging the films after the hybridization step. The entire sequence was conducted on ZnO Film-N, -R, and -P grown on glass and was also confirmed through mass loading frequency shifts on

a ZnO nanostructure-modified quartz crystal microbalance (QCM) with ZnO Film-N, -R, and –P surfaces.

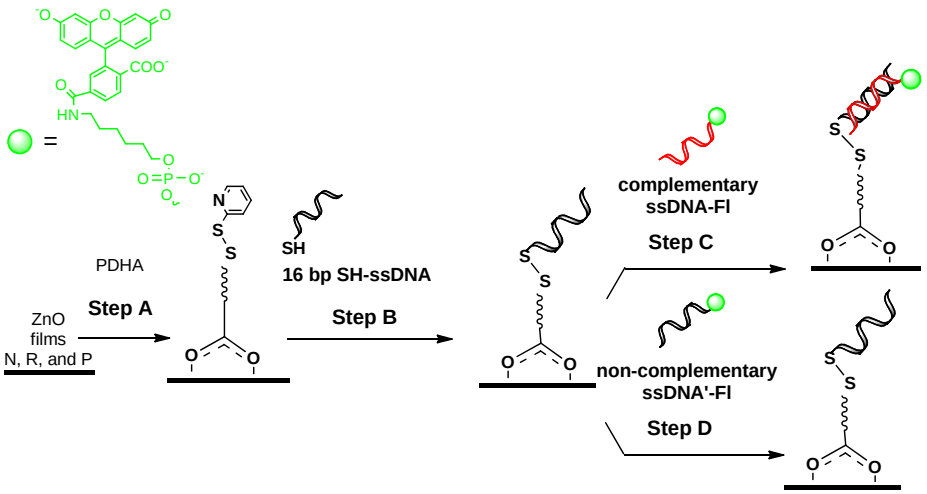

Fig. 3.6. Functionalization sequence employed to immobilize DNA on the three morphologies of ZnO (Film-P, -R, and –N). Step A involves the linker binding, Step B involves DNA immobilization, and Step C involves DNA hybridization. Ref. [47]

The functionalization sequence was monitored by FT-IR-ATR on ZnO Films-N, -R, and –P. In step A, binding of the COOH group resulted in spectral changes in the carbonyl region, (Fig. 3.7(a)). The characteristic carbonyl asymmetric stretch (ν_{as}(C=O)) band of the free acid at 1706 cm^{-1}, which is present in the spectrum of neat PDHA, was replaced by bands assigned to the carboxylate asymmetric stretch, ν_{as}(O···C···O), at 1540 cm^{-1} and at 1400 cm^{-1}. The C-O stretch band at 1250 cm^{-1} disappeared upon binding and the C-H stretch bands of the long saturated alkyl chain were visible in the region below 3000 cm^{-1} in the bound films. This C-H peak at 3000 cm^{-1} represents the binding of the linker molecules to the ZnO surface, and the amplitude of this peak roughly indicates how much of the linker molecules have attached to the ZnO samples. We did this

measurement for the three different ZnO surface morphologies. Fig. 3.7(b) shows the FTIR spectrum of each ZnO surface morphology after Step A of the functionalization route. The C-H absorbance peak for the ZnO Film-P exhibited the lowest amplitude of 0.03, while the ZnO Film-R has a an absorbance amplitude of 0.05, while the ZnO Film-N exhibited the highest C-H peak absorbance amplitude of 0.07. This qualitatively shows that the ZnO with the nanorod morphology is the best morphology among the three samples tested.

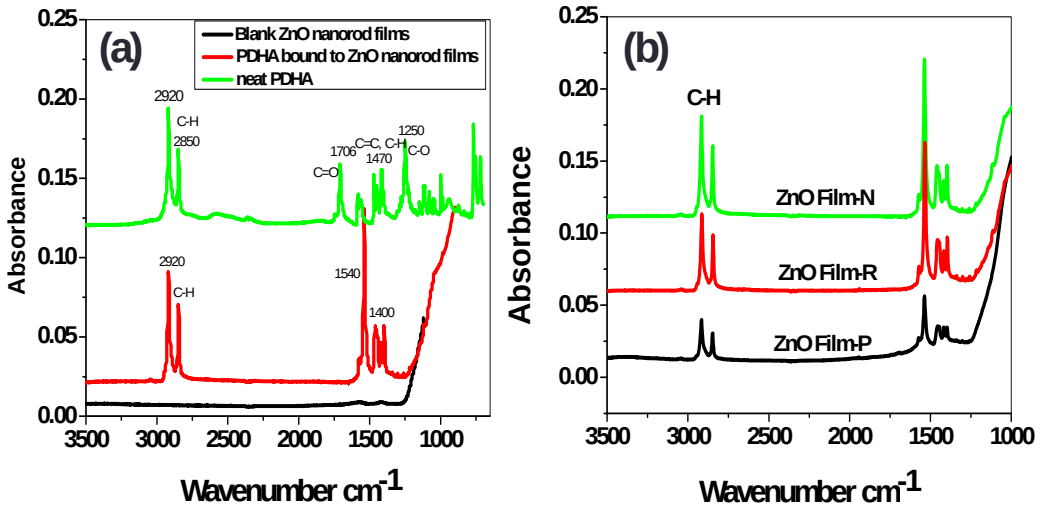

Fig. 3.7. (a) FTIR spectrum of the blank ZnO film (black), pure PDHA powder (green), and PDHA binding with ZnO (red). (b) FTIR spectrum of ZnO with PDHA binding for the various ZnO surface morphologies. Ref. [47]

All three morphology types of ZnO films, after the hybridization step with ssDNA-Fl were studied by monitoring the fluorescence of the 56-FAM fluorescein tag (λ_{ex} = 495 nm) which exhibits an intense band centered at 520 nm (Fig. 3.8). A comparison of the fluorescence spectrum of the immobilized and hybridized DNA-Fl on ZnO Film-N, -R and -P, show the fluorescence emission peak is highest for the ZnO Film-N, which is

consistent with the results obtained from the FTIR of the PDHA linker binding. As a control, we also took the fluorescence spectrum of the samples before the hybridization step. This step involves only the immobilized DNA and not the fluorescence tagged complement. As expected, the fluorescence spectrum for the control samples did not show any fluorescence peak at 520 nm which confirms the absence of the complementary DNA strands.

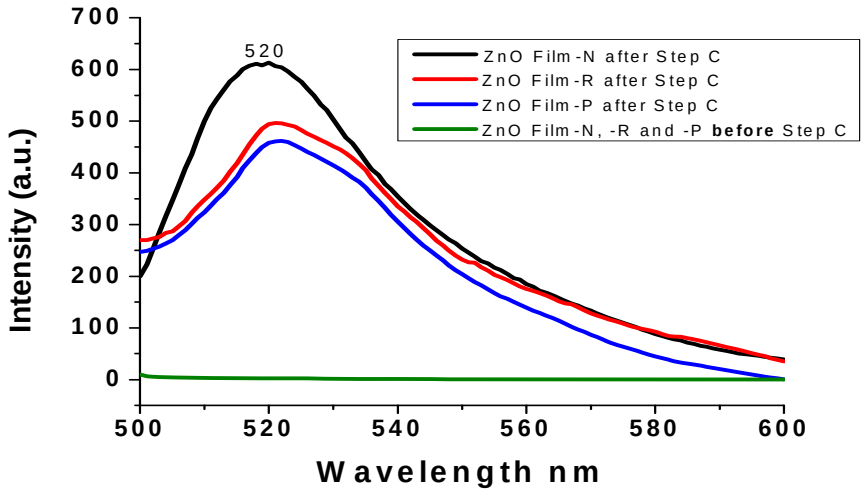

Fig. 3.8. Fluorescence spectra after Step 3 (ssDNA-Fl hybridization) for ZnO Films-N (black), ZnO Films-R (red); ZnO Films-P (blue); ZnO Films-N and-P before the hybridization step (green solid line) (λ_{ex}= 495 nm). Ref. [47]

3.4 Summary

In order to design the ZnO-based biosensors with high sensitivity and selectivity, the nanostructured ZnO sensing layer must be biochemically surface-treated through various biofunctionalization protocols. The morphology of the ZnO nanostructure surface also affects the quality of the molecular binding to ZnO. In this chapter we have

shown three different biofunctionalization protocols. The first protocol activates ZnO to specifically detect DNA. A three-step procedure to functionalize ZnO nanotips films with ssDNA followed by hybridization with complementary, fluorescein-tagged ssDNA was developed. First, long chain fatty acids capped with two different types of reactive end-groups (bifunctional linkers) were bound to the ZnO surface through the COOH group, leaving a second functional group available for further reactions. This allowed to covalently bind ssDNA to an "active layer" on ZnO by two different reactions: (i) thiol-disulfide exchange reaction, and (ii) NHS-ester hydrolysis reaction. A hybridization step was then performed on the DNA functionalized films. The second protocol activates ZnO to specifically bind to monoclonal epithelial growth factor receptor antibodies (mAbs EGFR) through silane linkage chemistry. The third protocol develops a platform for ZnO to sustain a living cell culture on the nanostructure surface. We demonstrated the growth of bovine aortic endothelial cells (BAEC) on fibronectin-treated ZnO nanostructures.

In addition to developing biofunctionalization protocols for ZnO, we also studied the effects of different surface morphologies of nanostructured ZnO on BAEC cell adhesion and proliferation and on DNA binding. For the case of BAEC cell growth on ZnO, we found that there is an inherent tradeoff in choosing the optimal ZnO morphology for the sensing surface. In terms of cell attachment, the cells favor the adhesion to flatter surfaces, but in terms of device performance the sharper surface provides the highest sensitivity due to the large effective sensing area provided by the nanostructures. It is determined that an intermediate morphology of rough ZnO surface is the most suitable morphology for adhesion and viability for cell growth without sacrificing the device sensitivity. For the case of DNA binding to ZnO, FT-IR-ATR spectra and fluorescence

emission studies indicated that the ZnO nanorod films with larger surface area (i.e. rough and nanorods) are needed for the immobilization and detection of biomolecules to be optimal.

The novel biological surface treatment techniques developed in this research allows the ZnO nanostructures to serve as both the biomolecular interface via surface functionalization and the sensitivity-enhancing layer resulting from the controlled morphology and gigantic effective surface area. This combination is expected to greatly enhance the device sensitivity, allow for simultaneous measurements of multiple parameters in a single test, and enable noninvasive and dynamic monitoring for living sample detection. More importantly, this novel approach allows sequential reactions on the surface of ZnO nanostructures and, in principle, can be extended to numerous other molecules and biomolecules.

Chapter 4

ZnO Nanostructure-Modified Thin Film Bulk Acoustic Wave Resonator for DNA/Oligonucleotide Sensing

In the previous chapter, we established biofunctionalization protocols to activate ZnO to selectively bind with vaious biochemical and biological species with high sensitivity. Beginning in this chapter we will discuss various ZnO-based biosensors using the integration of biofunctionalized ZnO nanostructured sensing layer with various ZnO-based devices. From Chapter 2 we learned that ZnO and its ternary alloy $Mg_xZn_{1-x}O$ are piezoelectric materials, which can be used for high quality factor bulk acoustic wave (BAW) resonators operating at GHz frequencies. The thin film bulk acoustic resonators (TFBARs) are attractive for applications of advanced communication and various sensors as they offer the capability of monolithic integration of BAW resonators with radio frequency integrated circuits (RF ICs). In this chapter we report the $Mg_xZn_{1-x}O$-based TFBAR biosensors. The devices are built on Si substrates with an acoustic mirror consisting of alternating quarter-wavelength silicon dioxide (SiO_2) and tungsten (W) layers to isolate the TFBAR from the Si substrate. High quality ZnO and $Mg_xZn_{1-x}O$ thin films are achieved through a radio frequency (RF) sputtering technique**.** Tuning of the device operating frequency is realized through varying the Mg composition in the piezoelectric $Mg_xZn_{1-x}O$ layer. Simulation results based on the transmission line model of the TFBAR show close agreement with the experimental results. ZnO nanostructures are grown on the TFBAR's top surface using metalorganic chemical vapor deposition (MOCVD) to form the nano-TFBAR sensor, which offers giant sensing area, faster response, and

higher sensitivity over the planar sensor configuration. A mass sensitivity higher than 10^3 Hz cm^2/ng is achieved. In order to study the feasibility of the nano-TFBAR for biosensing, the nanostructured ZnO surfaces are functionalized to selectively immobilize with DNA, which is verified by hybridization with its fluorescence-tagged DNA complement.

4.1. Introduction

Bulk acoustic wave (BAW) resonators, which are often associated with communication system applications [48,49,50,51,52,53], have many advantages, such as small size, low insertion loss, and lower power consumption. Thin film bulk acoustic wave resonators (TFBARs) are particularly attractive as they offer the capability of monolithic integration of BAW resonators with Si-based radio-frequency integrated circuits (RF ICs), leading to miniaturization by reducing circuit foot print. Piezoelectric ZnO thin film transducers are used in a variety of microwave acoustic device applications for the generation and detection of surface acoustic wave (SAW) and BAW due to their high electromechanical coupling coefficients. Various RF devices utilizing piezoelectric ZnO-based TFBARs have been reported, ranging from high frequency filters to compact low power GSM receivers. [51,52,53]. In addition to their applications for communications, BAW devices have also been used for sensor applications, such as temperature, pressure and ambient gaseous atmosphere detection [54,55]. Since TFBARs allow the implementation of BAW devices from several hundred MHz up to 20 GHz, a higher sensitivity manifested in large frequency shift per unit mass loading is expected. In

addition, TFBAR sensors are much smaller, and can be readily integrated into arrays. Solidly mounted TFBAR sensors can be fabricated on silicon, glass or other substrates using the planar technology. The sensors can be integrated with other Si-based electronic components on the same Si substrate. Another distinct advantage of BAW sensors is that they can be used for wireless distance probing in ecological applications. R. Gabl et al. reported solidly mounted ZnO FBARs with frequency around 2 GHz for bio- and gas-detection with an optimized sensitivity of 2500 Hz cm^2/ng, which was 2500 times larger in comparison with the typical 20MHz quartz crystal microbalance (QCM) sensors [56]. L. Mai et al. demonstrated ZnO-based FBAR devices for an ultra-mass-sensitive (0.057 x 10^5 Hz cm^2/ng) sensor application [57]. An implantable resonant mass sensor was reported for liquid sensing [58]. This sensor has a low Q value (40) at 2 GHz and a 5 ppm resonant frequency shift was detected, corresponding to $10^{-8}g/cm^2$ mass change on the sensor surface.

A new piezoelectric material, $Mg_xZn_{1-x}O$, which is a ternary alloy of ZnO and MgO, has been discovered and successfully grown [59,60]. ZnO belongs to the wurtzite crystal class, and is a well-known piezoelectric material. In contrast, MgO is a non-piezoelectric material with a rock-salt cubic structure. For the range of Mg content below approximately 33%, the $Mg_xZn_{1-x}O$ crystal retains the wurtzite structure. In comparison with ZnO, MgO has higher longitudinal and transverse bulk acoustic wave velocities. Thus, $Mg_xZn_{1-x}O$'s acoustic velocity increases and piezoelectric coupling decreases with increasing Mg content. By controlling the Mg mole percentage, the TFR frequency response can be tailored. $Mg_xZn_{1-x}O$ thin film bulk acoustic wave devices have been demonstrated on r-plane sapphire substrates [61].

In this chapter, $Mg_xZn_{1-x}O$ based single-mode thin film bulk acoustic wave resonators (TFBARs) built on Si substrates are demonstrated. In order to achieve the single-mode TFBAR, an acoustic mirror reflector structure is used to prevent the acoustic wave from transmitting into the Si substrate. The piezoelectric properties are tailored by controlling Mg composition in the $Mg_xZn_{1-x}O$ film. The TFBARs are adapted for mass-sensitive sensors. ZnO nanotips are grown on TFBAR surface using MOCVD to make the ZnO nano-TFBAR with high mass-sensitivity. The ZnO nanostructured surfaces are functionalized through selective DNA immobilization and hybridization for biosensing.

4.2. Device Structure and Design

A schematic of the TFBAR device structure consisting of Al/$Mg_xZn_{1-x}O$/Au/acoustic mirror/Si is shown in Fig. 4.1. For the experiments performed in Section 4.3, the device consists of Al and Au as the top and bottom electrode, respectively. Au is chosen as the bottom electrode to allow deposition of high quality ZnO and $Mg_xZn_{1-x}O$ thin films on top of it by the RF sputtering technique [62]. Al or Au is used as the top electrode. The Al electrode is used for the regular TFBAR without ZnO nanostructures to minimize the mass loading from the electrode. The acoustic mirror consists of two periods of quarter-wavelength SiO_2/W Bragg reflector, which is used to isolate the resonator from the Si substrate. ZnO and $Mg_xZn_{1-x}O$ thin films are used as piezoelectric layer. When a signal is applied between the top and the bottom electrodes, a longitudinal acoustic wave mode is excited. We have also integrated ZnO nanostructures with the TFBAR to form the novel biosensors, where, the ZnO nanostructures are deposited on Au

top electrode to provide a giant sensing area. The Au top electrode is used instead of Al to facilitate MOCVD growth of ZnO nanostructures with good crystalinity and to avoid the oxidation of the metal electrode.

The c-axis oriented ZnO and $Mg_xZn_{1-x}O$ ($0<x<0.33$) films were deposited using the RF sputtering technique. As-grown ZnO and $Mg_xZn_{1-x}O$ films generally show n-type semiconducting properties due to oxygen vacancies, Zn interstitials, and other defects and impurities. In order to effectively stimulate the piezoelectric effect in ZnO and $Mg_xZn_{1-x}O$, this n-type conductivity has to be compensated by heavily doping with species, such as Li, Ni, or Cu. We made ZnO and $Mg_xZn_{1-x}O$ sputtering targets with Ni-doping. The ZnO and $Mg_xZn_{1-x}O$ sputtering targets were prepared by mixing appropriate quantities of 99.99% pure ZnO and MgO powders with 2% wt NiO powder for compensation doping.

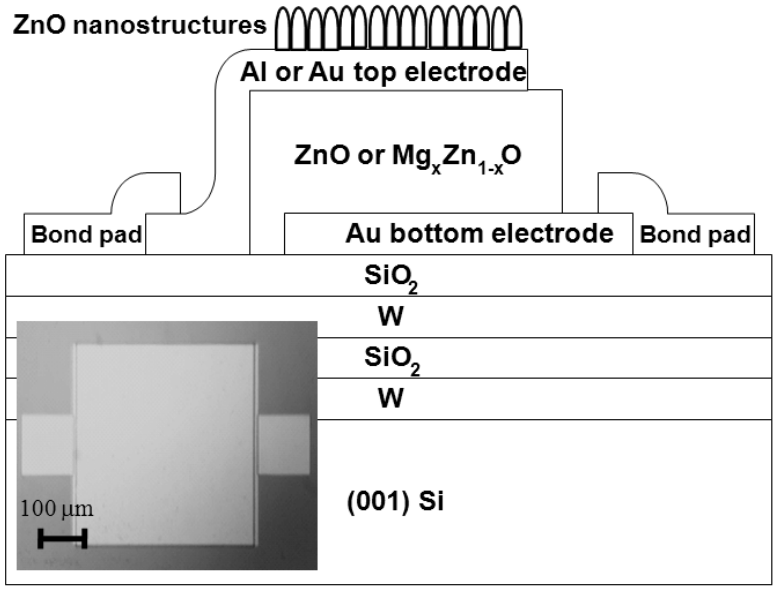

Fig. 4.1. Schematic diagram of the $Mg_xZn_{1-x}O$/Si TFBAR structure, the inset shows the optical microscope picture of TFBAR device. For the TFBAR nanosensor, Au top electrode is used to facilitate MOCVD growth of ZnO nanostructures. (Ref [11])

The ZnO and $Mg_xZn_{1-x}O$ films deposited from these targets do not require post-deposition diffusion at high temperature.

The sputtering chamber is equipped with a standard RF power source. Before deposition, the chamber was kept at a vacuum level of 5.0 x 10^{-6} torr. During deposition, a mixture of 1:1 Ar and O_2 was fed into the chamber, with the pressure of the chamber maintained at 7.5 x 10^{-3} torr. The substrate was heated at 400 ˚C to achieve films with good crystal quality and surface morphology. A ZnO buffer layer (50 nm) was first deposited, followed by deposition of a thicker film at a deposition rate higher than 0.7 μm/hr.

The crystallographic orientation and structural quality of the as-grown films were determined using a Bruker D8 Discover four-circle x-ray diffractometer (XRD). Fig. 4.2(a) shows an X-ray θ-2θ scan of ZnO and $Mg_{0.17}Zn_{0.83}O$ sputtered on SiO_2/Si. The scan is done using CuKα radiation to analyze the orientation of the ZnO film. ZnO (002) peak is observed at ~34.3°, indicating predominantly c-axis oriented ZnO film. Fig. 4.2(b) shows the X-ray θ-2θ scan of predominantly c-axis oriented $Mg_{0.17}Zn_{0.83}O$ (002) with peak at ~ 34.7°.

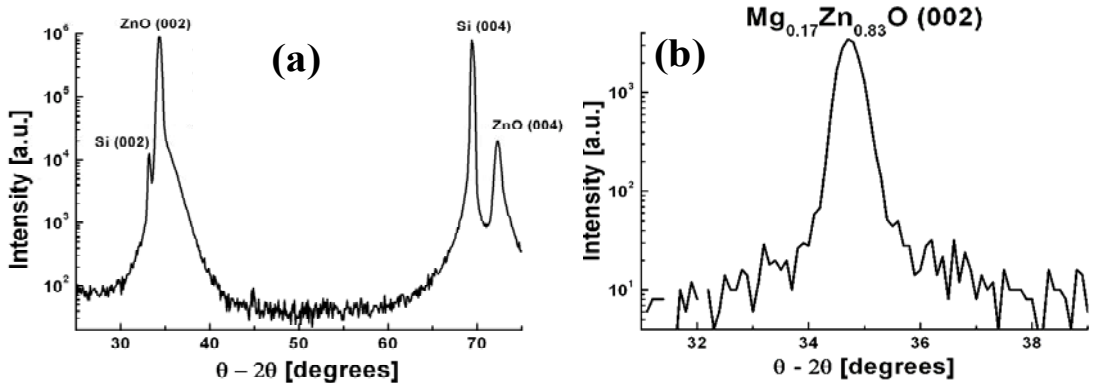

Fig. 4.2. X-ray θ-2θ scan of (a) ZnO and (b) $Mg_{0.17}Zn_{0.83}O$ films deposited on SiO_2/Si.

The surface morphology of the $Mg_xZn_{1-x}O$ films were characterized using a Leo-Zeiss field emission scanning electron microscope (FESEM). Fig. 4.3(a) shows the FESEM image of a $Mg_{0.2}Zn_{0.8}O$ thin film deposited on the mirror/Si structure. The image is taken from the active region of the device where the film is directly on the acoustic mirror, rather than on the Au bottom electrode. The $Mg_{0.2}Zn_{0.8}O$ film has a dense columnar structure, with smooth surface. The two-period acoustic mirror structure (750 nm SiO_2 and 720 nm W) is clearly visible as alternating light and dark layers.

Single crystalline ZnO nanostructures of 200 nm height and 70 nm diameter, are directly grown on Au electrode by MOCVD. The details of MOCVD growth have been reported earlier [63,64]. Diethyl Zinc (DEZn) and O_2 are used as Zn source and oxidizer, respectively. The substrate temperature was maintained at ~475 ^oC and chamber pressure at ~50 Torr during the MOCVD growth. The FESEM image for the vertically aligned ZnO nanostructures is shown in Fig. 4.3(b).

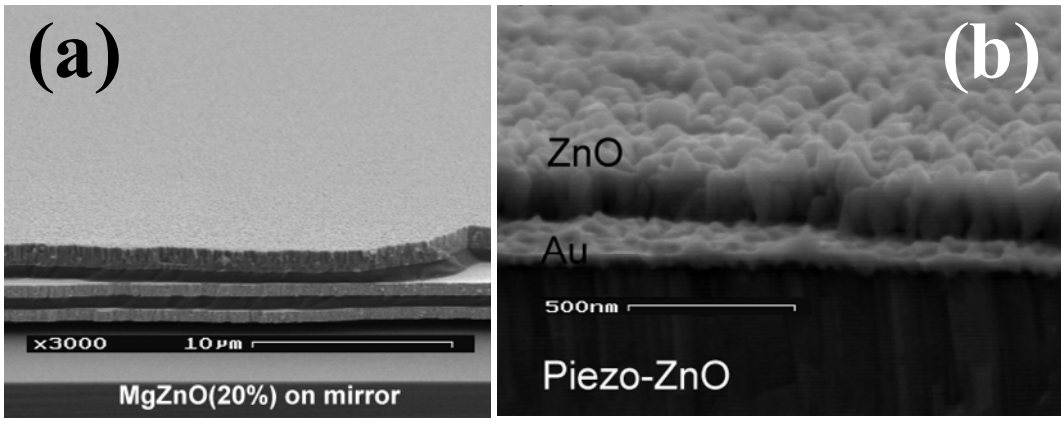

Fig. 4.3. Cross-sectional FESEM images of (a) $Mg_{0.2}Zn_{0.8}O$ film deposited on the mirror/Si structure; (b) ZnO nanostructures deposited on Au electrodes. Ref. [11]

4.3. Device Modeling and Characterization

4.3.1 Tuning of resonant frequency using $Mg_xZn_{1-x}O$

The three-port transmission line model [65] is used to analyze behavior of the acoustic waves propagating in the $Mg_xZn_{1-x}O$ thin film resonators built on Si substrates, as shown in Fig. 4.4. The resonator only excites the longitudinal wave mode, hence the circuit model is comprised only of the piezoelectrically active longitudinal branch.

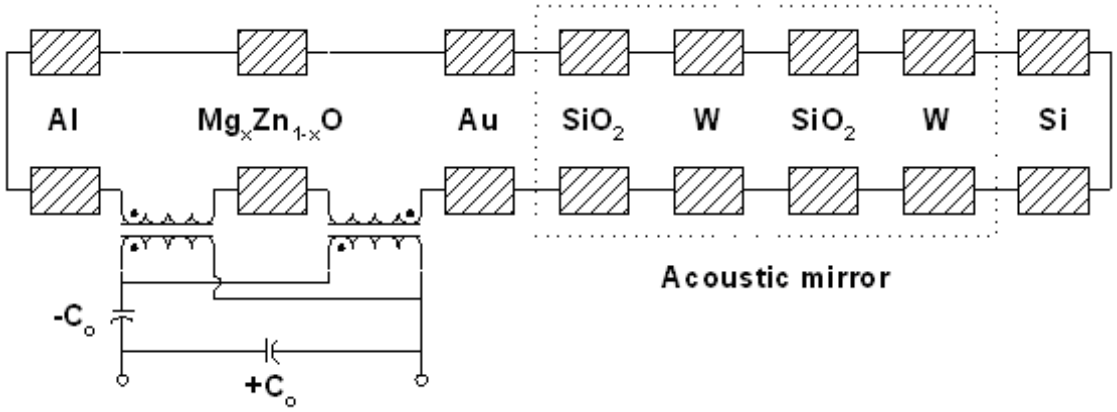

Fig. 4.4. The transmission line model of the multilayer TFBAR structure used for simulation of the frequency response of the device. Ref. [11]

This equivalent circuit model of the multilayer structure of the TFBAR was constructed using a modular building-block approach, wherein each layer corresponds to a network feature. The acoustic impedances of W and SiO_2 are 97.40 x 10^6 kg $s^{-1}m^{-2}$ and 13.25x10^6 kg $s^{-1}m^{-2}$), respectively. The reflectivity of the W – SiO_2 interface is:

$$R_{W,SiO2} = \frac{Z_W - Z_{SiO2}}{Z_W + Z_{SiO2}} \approx 0.79 \quad (1)$$

The two-period mirror structure effectively isolates the main resonance. In order to completely eliminate the spurious resonances from the substrate, the multiple-period mirror structure should be used.

RF characterization of the TFBAR devices was conducted using an HP 8573D Network Analyzer (Agilent Technologies, Palo Alto, CA) and a Cascade Microtech probe station (Cascade Microtech Inc. Beaverton, OR). The reflection parameter S_{11} of the thin film resonator was measured and the longitudinal acoustic velocity was calculated. The operating frequency of the TFBAR was measured for the corresponding mole fraction of Mg in $Mg_xZn_{1-x}O$ film. Fig. 4.5 shows the S_{11} spectra of $Mg_xZn_{1-x}O$ TFBARs whose device area is 400 μm x 400 μm. The solid line is the frequency response of a TFBAR with 1.12 μm thick ZnO layer, and the resonance frequency is at 2.04875 GHz with S_{11} = -13.14 dB. The dash line represents a TFBAR with 1.25 μm thick $Mg_{0.08}Zn_{0.92}O$ layer, and the resonance frequency is at 1.96875 GHz with S_{11} = -21.19 dB. The dotted line presents a $Mg_{0.2}Zn_{0.8}O$ TFBAR with film thickness about 1.38 μm, and the resonance frequency is at f = 1.91687 GHz and S_{11} = -23.5 dB. The simulation results based on the transmission line model reveal that the resonant frequency of the thin film resonator can be tailored by using different mole fractions of Mg in the piezoelectric $Mg_xZn_{1-x}O$ layer. The series resonant frequency f is determined by ratio of the phase velocity, v and the thickness of piezoelectric layer, h:

$$f = \frac{v}{2h} \tag{2}$$

The calculated phase velocity increases 7% when the Mg mole composition increases from 0 to 2%. The measured data of the resonant frequency corresponding to various

mole fractions of Mg in $Mg_xZn_{1-x}O$ agree closely with the simulation results. The calculated phase velocities from S_{11} measurements are 4,589 m/s for ZnO, 4,922 m/s for $Mg_{0.08}Zn_{0.92}O$, and 5,291 m/s for $Mg_{0.2}Zn_{0.8}O$.

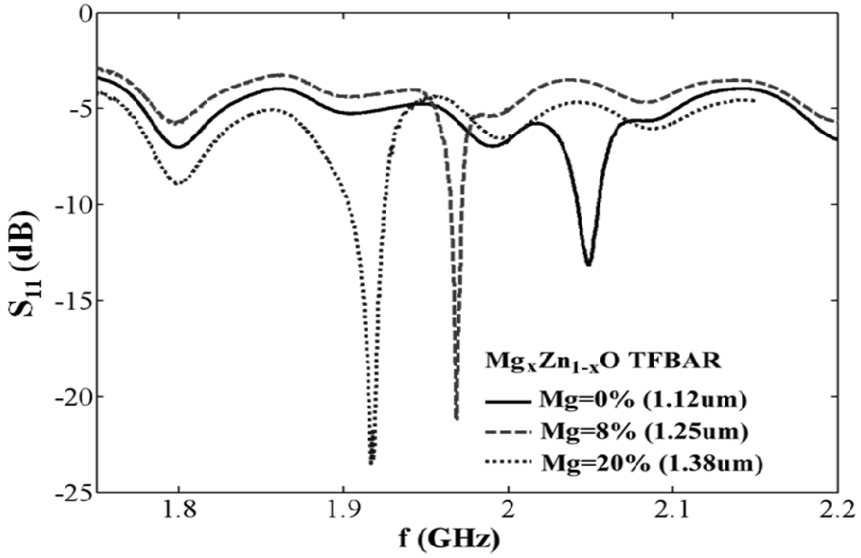

Fig. 4.5. Measured S_{11} spectra of the $Mg_xZn_{1-x}O$ TFBARs with varying Mg compositions x=0, 0.17 and 0.20 in the $Mg_xZn_{1-x}O$ films. The experimental results closely match the simulation results.

4.3.2. Device Calibration and Mass Loading Sensitivity

The sensitivity due to the mass loading effect is calculated using the Sauerbrey's formula [66]:

$$\Delta f = -\frac{2 f_0^2}{A\sqrt{c_{66}\rho}}\Delta m = -S_f \Delta m \tag{3}$$

where f_0 is the reference resonant frequency and $f_0 + \Delta f$ is the loaded frequency, c_{66} is the stiffness constant of the piezoelectric material, ρ is the density of the piezoelectric

material. In the case of ZnO, c_{66} = 4.43 x 10^{10} N/m^2 and ρ = 5680 kg/m^3. The TFBAR used for sensitivity measurement has a piezoelectric ZnO layer with thickness of 1.24μm. To determine the mass loading sensitivity S_f, we deposited a 60 nm layer of SiO_2 on the top electrode (with area of 150 μm x 150 μm) of the TFBAR using plasma enhanced chemical vapor deposition (PECVD). The density of SiO_2 deposited by PECVD is 2.3 g/cm^3. The measured frequency shift due to the deposited SiO_2 layer is 23.7 MHz as shown in Fig. 4.6. The experimental mass sensitivity S_f of 1.72 x 10^3 Hz cm^2/ng is achieved, which is useful for ultra-sensitive-mass loading sensor applications.

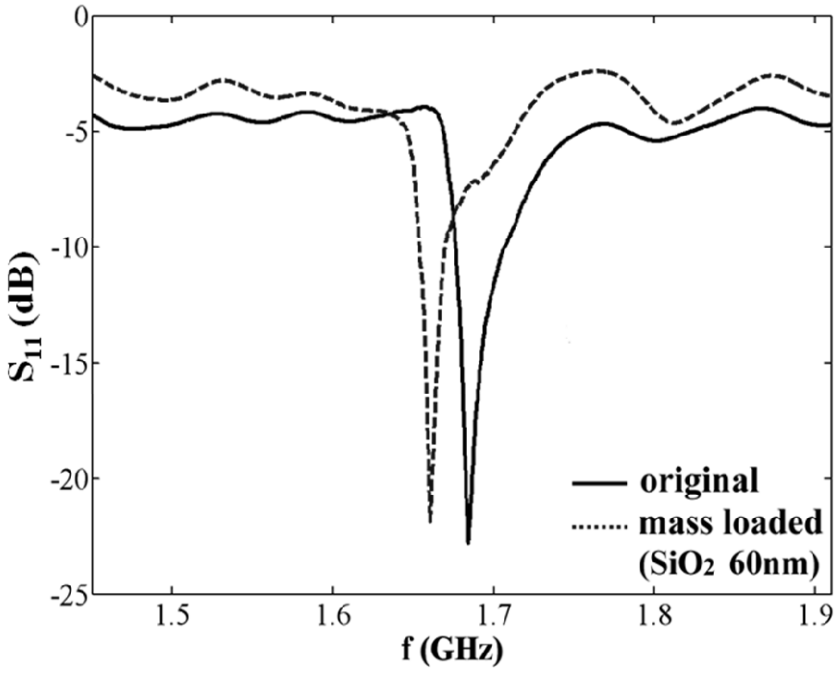

Fig. 4.6. Measured S_{11} spectra of a 150 μm x 150 μm ZnO TFR built on a mirror/ Si substrate, before and after deposition of 60nm SiO_2 as mass-loading.. Frequency shift due to mass loading results in 1.72 kHz/ng sensitivity. Ref. [11]

4.4. DNA Sensing using the ZnO_{nano}-TFBAR: Results and Discussion

ZnO nanostructures are integrated with the TFBAR to form the ZnO_{nano}-TFBAR. The ZnO nanostructures are directly grown on the top electrode by MOCVD as described in Section 4.2. The ZnO nanostructures have the advantage of controllable wettability which allows it to be super-hydrophilic surface. The super-hydrophilic property of the nanostructured TFBAR surfaces allow for the consumption of much less liquid samples during sensing.

The functionalization of the nanostructured ZnO sensing surface enables the nanostructures to only selectively bind to the prescribed set of biomolecules. The functionalization scheme is used to implement the selective binding of specific DNA oligonucleotides on the nanostructured ZnO surface, then hybridized with its fluorescent-tagged complement. The optimized chemical functionalization scheme discussed in Section 3.2 was applied to the ZnO nanostructures on the ZnO_{nano}-TFBAR which we reiterate here in simplified form: Step 1: ZnO + linker, Step 2: DNA immobilization, and Step 3: fluorescence-tagged DNA hybridization. After every step, the nanotips were rinsed with a pH-controlled buffer solution prescribed in Section 3.2, and the S_{11} spectrum of the ZnO_{nano}-TFBAR was measured for frequency shift due to mass loading.

Fig. 4.7 shows the frequency shifts of the ZnO_{nano}-TFBAR after each chemical step in the optimized functionalization scheme outlined above. The ZnO_{nano}-TFBAR sensing area is 0.25mm x 0.25mm. The solid black line represents the frequency response of ZnO_{nano}-TFBAR before step 1. The frequency peak at minimum insertion loss is 1562.81 MHz. After step 1, the frequency at minimum insertion loss shifted to 1553.75

MHz. After step 2, the frequency at minimum insertion loss further shifted down to 1540.94 MHz. After step 3, the frequency at minimum insertion loss further shifted to 1535.94 MHz. The measured results show that the resonance frequency decreases with increasing mass loaded on the top electrode of the ZnO_{nano}-TFBAR. The total frequency shift was about 26MHz, corresponding to 16.25 ng of hybridized DNA and linker molecules combined. To verify that the immobilized and hybridized DNA molecules only selectively attached to the ZnO nanostructured sensing area, we performed fluorescence measurements on the ZnO_{nano}-TFBAR sensing area. The fluorescence image of the nano-TFBAR in the inset of Fig. 4.8 shows that only the ZnO nanostructured sensing electrode area (bright gray squares) is positively fluorescing. This confirms that the DNA molecules only attached themselves to the ZnO nanostrucrued sensing area of the nano-TFBAR device. These results demonstrate that the ZnO nano-TFBAR is a promising device for biosensing applications.

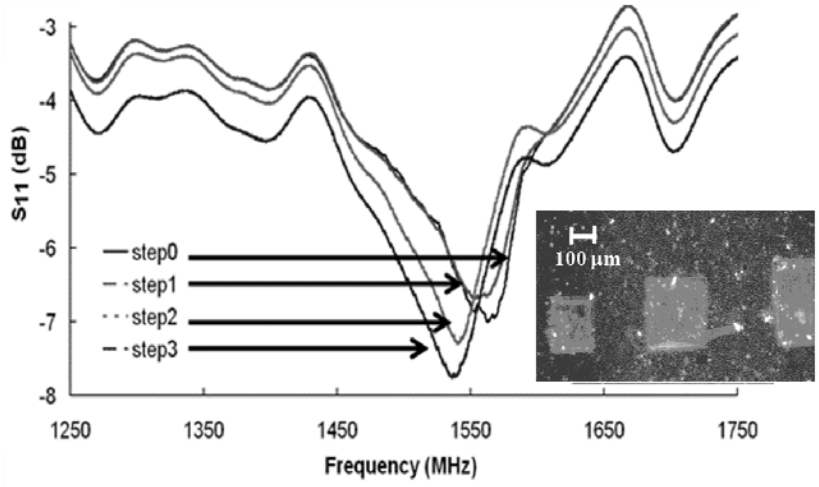

Fig. 4.7. Frequency shift due to mass loading on the nano-TFBAR, step 0: nano-TFBAR only, step 1: adding bifunctional linker, step 2: DNA immobilization, and step 3: DNA hybridization. Inset: fluorescence image nano-TFBAR sensors containing the fluorescing hybridized DNA. Ref. [11]

4.5. Summary

A Thin film bulk acoustic resonators using the new piezoelectric material $Mg_xZn_{1-x}O$ were demonstrated. The TFBAR devices are built on Si substrates with an acoustic mirror which consists of alternating quarter-wavelength SiO_2 and W layers. The mirror isolates the acoustic wave from transmitting into the Si substrate, assuring the single mode operation. The c-axis oriented piezoelectric $Mg_xZn_{1-x}O$ thin films were deposited using RF sputtering on the mirror/Si substrate. The bulk acoustic wave velocity can be tailored by changing Mg composition in $Mg_xZn_{1-x}O$. This allows flexibility in TFBAR device design because the resonant frequency can be determined by both thickness and Mg composition of the piezoelectric film. The mass sensitivity of ZnO based 1.67 GHz TFBAR is at 1.72 x 10^3 Hz cm^2/ng, which is three orders higher in comparison of the standard QCM. The ZnO_{nano}-TFBAR biosensor is made by integrating ZnO nanostructure on the ZnO-based TFBAR device. The selective DNA immobilization and hybridization are realized through optimized functionalization of the nanostructured sensing area.

Chapter 5

Dynamic and Nonivasive Cell Monitoring Using ZnO Nanostructure-Modified Quartz Crystal Microbalance

In the previous two chapters, we focused on designing ZnO-based biosensors aimed at detecting biomolecular species. These biomolecules are the building blocks of a larger and more complex biological species, the living cell. Non-invasive and real-time examination of live cell function is essential in advancing the understanding of the mechanistic and dynamic progression of biological processes related to cell growth and death. Such understanding has a great impact on development of the cell-based drugs and assays. It also complements the existing analytical tools that are used for gene and protein identification. The main issue with cellular measurements is that the physical quantities such as viscoelasticity do not directly report on a specific molecular target in a given cellular pathway [67]. However, loss of homeostasis, alterations in molecular function, and deregulation of molecular pathways inevitably manifest themselves as detectable physical changes in cellular properties. There are numerous methods being used to monitor biological cell activity. Among them, optical microscopy, hemacytometry, and flow cytometry are the standard techniques [68]. However, the standard methods often involve invasively killing the cells and tagging them with optically active biomolecules to obtain information about their growth, proliferation, and function. Recently, there has been increasing interest in developing non-invasive and label-free techniques in monitoring cell function. In-vivo flow cytometry [69] is one of the most recent developments for non-invasive cell monitoring, but is not label free. It

combines confocal microscopy and flow cytometry and is limited to the cells that are circulating in the bloodstream. This method requires the target cells to be tagged with fluorescent markers to act as the label for the confocal microscope. Non-optical biosensing devices have also been employed for cellular monitoring. Among them, the most common method is the impedance spectrum analysis of acoustic wave devices such as the quartz crystal microbalance (QCM), the QCM with dissipation (QCM-D) [70,71,72], or the E-Plate impedance sensor [73].

The quartz crystal microbalance (QCM) which is a bulk acoustic wave device has been used as a compact, versatile and cost effective sensor with a high quality factor (Q), typically 10^4 to 10^6 at room temperature in vacuum or gaseous environment [74]. A typical QCM device consists of a piezoelectric AT-cut quartz crystal sandwiched between a pair of metal electrodes. QCM sensors have been traditionally used to dynamically monitor thin film thicknesses during the deposition through change in mass loading by measuring the shift of its resonant frequency (Sauerbrey 1959). QCM devices can operate in the range of several MHz to tens of MHz, determined by the thickness of the quartz layer. The QCM-D on the other hand, is a modified version of the QCM which allows the sensor to simultaneously detect frequency shifts and energy dissipation [70]. Both the QCM and QCM-D have been used as sensitive and accurate biochemical sensors [75,76,77,78]. Recently, QCM and QCM-D have found important biological applications, including detection of protein adsorption on metals [79], DNA immobilization and hybridization [8,80], human serum albumin [81], and biological cell growth studies [67,70,71,82,83,84,85,86,87]. For cell monitoring applications, the impedance spectrum analysis using the QCM, QCM-D and E-plate sensors measure the

peak frequency shift (QCM/QCM-D) and resistance shift (E-plate) as a function of time when the cell culture grows on the sensor's active area. These devices are also used to analyze the time evolution of the acoustic energy dissipation due to cell accumulation, making them suitable for dynamic and noninvasive biological sensing.

The use of nanostructured ZnO for biological cell analysis has been mainly focused on (i) a nanostructured platform to facilitate cellular adhesion for various cell lines [5], (ii) a conductive nano-coating for intracellular probes mainly to detect cytoplasmic pH [88,89], and (iii) a material for enhancing optical detection (fluorescence and Raman type microscopy) [90].

In this chapter we present a dynamic and noninvasive method of monitoring the adhesion and proliferation of bovine aortic endothelial cells (BAEC) using a ZnO nanostructure-modified quartz crystal microbalance (ZnO_{nano}-QCM) biosensor deployed *in-situ* of a standard cell culture environment. Cell adhesion to the ZnO nanostructure-modified sensing surfaces with various morphologies is studied and the optimal morphology is chosen for the BAEC adhesion. The dynamic motional resistance and inductance relating to the cells' viscoelastic properties during growth are extracted from the measured time-evolving acoustic spectra. The Butterworth-Van-Dyck (BVD) model is adapted for the ZnO_{nano}-QCM biosensor system and is used to correlate the measured time-evolving acoustic spectra with the motional characteristics of cell attachment and proliferation. Finally we will show that the ZnO_{nano}-QCM parameters reveal viscoelastic transitions during the early seeding and adhesion stage in the cell growth. Cellular confluency or the maximum proliferation is detected when the temporal components of the acoustic spectra reach the steady state.

5.1. ZnO Nanostructure-Modified ZnO_{nano}-QCM

5.1.1 Device Structure, Characterization and Modeling

Device Structure: The ZnO_{nano}-QCM biosensor consists of a conventional QCM with ZnO nanostructures directly grown on its sensing electrode. The schematic of a ZnO_{nano}-QCM device is shown in Fig. 4.1(a) for the top view, and in Fig. 4.1(b) for the cross sectional view of the multilayer structure. The piezoelectric AT-cut quartz layer is sandwiched between two 100 nm gold electrodes. The quartz substrates have a diameter of 1.37 cm and the sensing area is 0.2047 cm^2. The ZnO_{nano}-QCM device consists of ZnO nanostructured arrays that are integrated on a standard AT-cut QCM. The ZnO nanostructures are directly grown on the sensing area of the QCM through a shadow mask using MOCVD. The optimal ZnO nanostructure morphology was determined through the control of the MOCVD growth conditions described in Section 3.2. The ZnO nanostructure layer has a thickness of ~500 nm. The ZnO-covered sensing area was exposed to UV light to make it super-hydrophilic (Zhang *et. al*., 2007). The combined effect of very large effective surface area of the nanostructures and the ability to be induced into a superhydrophilic state makes the ZnO_{nano}-QCM a very sensitive mass measuring device as well as a monitoring device for viscoelastic transitions in the sample. The operating frequency of the standard QCM is 10 MHz, while the ZnO_{nano}-QCM has an operating frequency of 9.916 MH

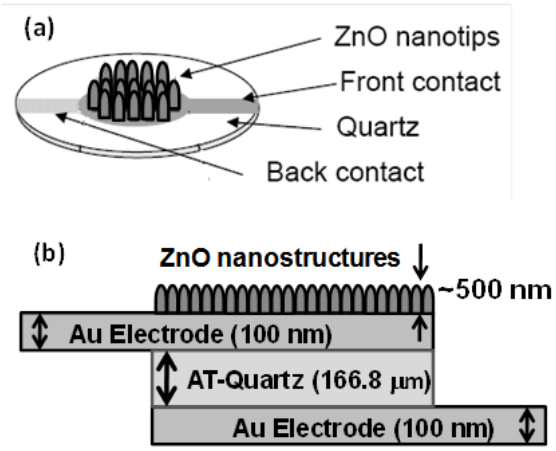

Fig. 5.1. (a) The ZnO_{nano}-QCM biosensor schematic, (b) its multilayer structure. Ref.[46]

Device Modeling and Characterization: The characterization and testing of the nano-QCM device was conducted using an HP 8573D Network Analyzer (Agilent Technologies, Palo Alto, CA). The forward transmission parameter (S_{21}) of the device was measured. The mass loading on the QCM can be determined directly from the shift in its resonant frequency and its mass sensitivity, S is given by the formula

$$S = \left(\frac{\Delta f}{f_0}\right)\left(\frac{A}{\Delta m}\right) \tag{5.1}$$

where Δf is the resonant frequency shift due to mass loading, f_0 is the resonant frequency of the QCM, Δm is the mass loading, and A is the area of the quartz layer.

The measured resonant frequency of the standard QCM is 9.9936 MHz while the nano-QCM has 9.9163 MHz resonance. Sauerbrey's model [66] is popular to calculate the QCM's mass loading. However, Sauerbrey's model which is typically used for dry sample testing is not accurate to predict frequency shifts in the liquid phase. In the liquid case, the acoustic waves would leak out to the liquid layer and introduce a damping effect on the resonating acoustic modes, resulting in reduction in the forward transmission

parameter (S_{21}) amplitude and change in its phase, which collectively cause the shift in resonant frequency. For simulation of QCM's mass loading in liquid case, we have used our multilayer transmission line (MTL) model [65] in which we consider the acoustic wave propagation through the different layers of the QCM device and calculate the acoustic impedance of the device by treating each layer as a two-port system. The MTL simulation parameters of the nano-QCM follow the multilayer structure shown in Fig 5.1(b). The density of the piezoelectric AT-cut quartz layer used in the simulation is 2.648×10^3 kg/m^3, and its acoustic velocity is 3.336×10^3 m/s. For the Au electrodes the density is 19.32×10^3 kg/m^3 and acoustic velocity is 3.240×10^3 m/s. Similarly, for the ZnO sensing layer we used the density value of 5.665×10^3 kg/m^3 and acoustic velocity of 6.152×10^3 m/s. The output of the MTL simulation is the device impedance spectrum and is shown in Fig. 5.2. The simulated frequency shift due to mass loading of 5 μL of water on the nano-QCM is 3.1414 kHz, which is in good agreement with the experimental data of 2.9034 kHz shown in Fig. 5.3.

Sensitivity Enhancement Through Wettability Control: We have shown that ZnO nanotips can be made reversibly super-hydrophylic and super-hydrophobic by UV irradiation and oxygen annealing, respectively [10]. Making the nano-sensing area super-hydrophilic significantly decreases the liquid sample consumption. In this work, the nano-QCM is exposed under UV radiation from a lamp (Model 66002, Oriel Optics, Stratford CT) for 10 minutes to make the nano-sensing area super-hydrophilic. The nano-QCM with the super-hydrophilic nano-ZnO surface only requires 0.5 μL of DI water to cover the entire sensing area while it needs to take 16 μL for the standard QCM.

Moreover, the same nano-QCM device exhibits a tenfold increase in frequency shift in detecting the same 1mL of water from the standard QCM (6.2 kHz for the nano QCM and 0.7 kHz for the standard QCM). This enhancement in device sensitivity is attributed to the giant effective sensing area for the liquid sample introduced by the super-hydrophilic ZnO nanotip surface.

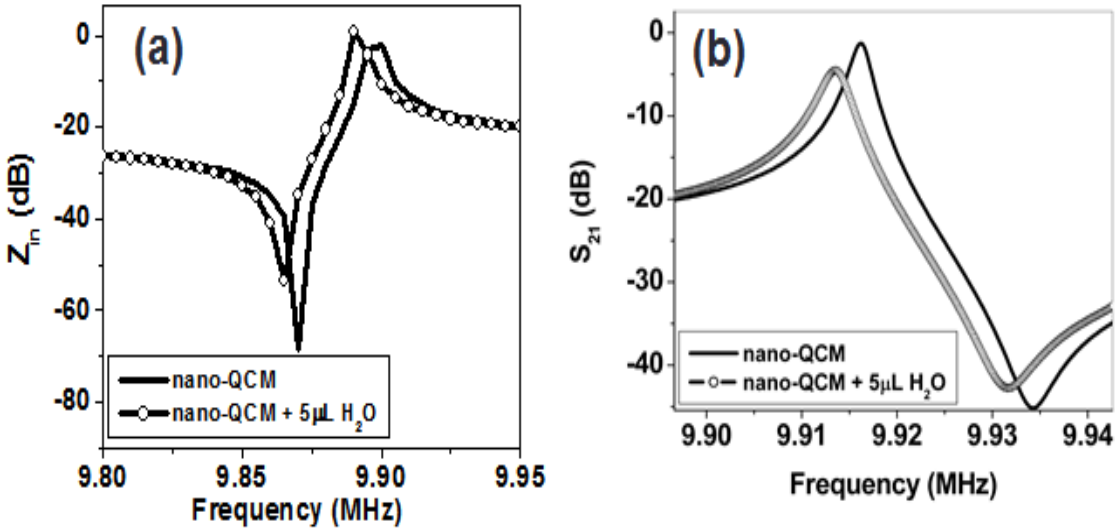

Fig. 5.2. (a) Simulated device impedance spectrum of the nano-QCM showing a frequency shift of 3.1414 kHz corresponding to a mass loading of 5 μL of water. (b) . S_{21} parameter measurement of the nano-QCM showing a frequency shift of 2.9034 kHz corresponding to a mass loading of 5 μL of water. Ref. [8]

5.1.2. DNA Sensing Using the ZnO_{nano}-QCM: Demonstration of Biosensing

Before we can deploy the ZnO_{nano}-QCM *in situ* of a living cell culture for dynamic monitoring purposes, we must first demonstrate that it can be operated and

calibrated under biochemical environments. To accomplish this we applied the stepwise DNA functionalization scheme developed in Section 3.1 to the ZnO_{nano}-QCM. The chemical scheme to functionalize ZnO with DNA in this section can be summarized in three steps (as shown in Fig. 5): step 1: ZnO + linker, step 2: DNA immobilization, and step 3: fluorescence-tagged DNA hybridization. The nano-QCM sensing area was immersed in the linker solution in a Teflon liquid flow static cell (International Crystal Manufacturing Co, Inc.) for 12 hours (step 1). DNA incubation was done on the device for 4 hours (step 2) and hybridization took 1.5 hours (step 3). After every step the nanotips were rinsed with a pH-controlled buffer solution and gently dried under gentle nitrogen flow. It is found that the selective DNA immobilization and hybridization can only be achieved on the ZnO nanotips if the three steps are completely followed in order.

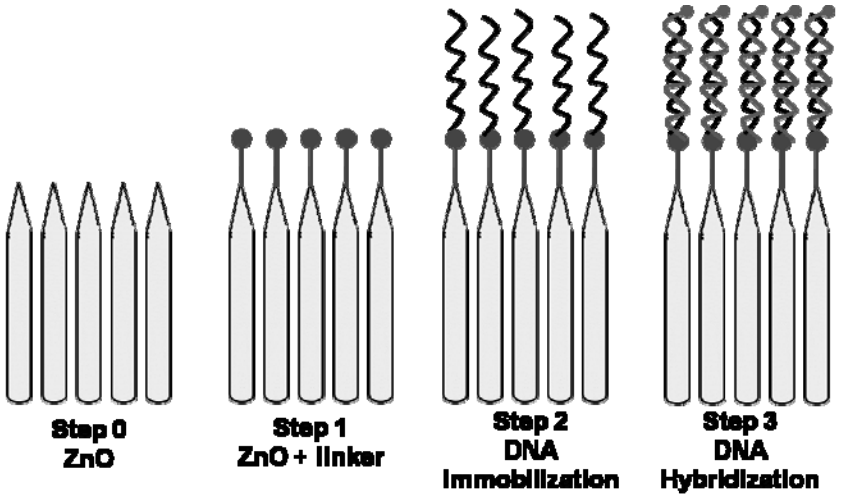

Fig. 5.3 Simplified schematic of the chemical functionalization scheme for the ZnO nanotips to implement selective DNA immobilization and hybridization. Ref. [8]

The nano-QCM device is used to sense the mass loading of each chemical step outlined above. The device sensing area was first made super-hydrophilic by exposing it

to UV light for 10 minutes. The device is then calibrated for DNA molecule detection by adding 2 μL of non-activated DNA oligonucleotide, which yielded a frequency shift of 0.3 kHz due to mass loading. The device sensitivity of 154.817 cm^2/g was calculated using Eq. (1). We then performed the optimized three-step procedure on the nano-QCM for DNA immobilization and hybridization that was outlined in the previous section. The frequency shifts of the nano-QCM's S_{21} parameter, resulted from the mass loading effect for each of the three chemical binding steps. The frequency response demonstrating the mass loading detection of each chemical step is shown in Fig. 5.4. The shift of 1.992 kHz after step 1 confirms that there are 265.606 ng of the linker molecules on the nano-QCM sensing area. A shift of 2.271 kHz after step 2 shows that 302.673 ng of DNA molecules are immobilized on the nanotips via the bifunctional linkers, and finally, a shift of 2.271 kHz after step 3 shows that 264.939 ng of the fluorescence-tagged complement DNA molecules are hybridized on the nanotips containing immobilized DNA. The uniform shift in S_{21} frequency throughout the 3-step chemical process indicates that the immobilized and hybridized DNA molecules have uniformly attached to the sensing area. The sensing area of the nano-QCM was washed with a pH-controlled buffer after hybridization and fluorescence imaging confirms that the immobilization and hybridization only occurs at the nanotip sites. Fig. 5.5(a) shows the fluorescence image of the nano-QCM sensing area after the 3-step process which confirms the presence of hybridized DNA on the nanotips. Fig. 5.5(b) shows the fluorescence image of the edge of the sensing area of the same device confirming that the DNA molecules bind only to the ZnO nanotip-covered sensing area of the device. The 3-step DNA binding scheme was also performed on a standard QCM. The experiment yielded no discernible frequency

shift from the S_{21} parameter and showed negatively fluorescing images of the sensing area. This confirms that the linker layer is validated only to ZnO nanotips and DNA. The ability of the ZnO nanotips to enhance the sensing function of the conventional QCM to facilitate and detect selective DNA immobilization and hybridization make the nano-QCM a promising biocompatible sensing device. Such a sensor also possesses advantages, including high sensitivity, simple structure, low cost, and compact size. The nano-QCM biosensor is promising to be used for enhanced chemical reaction analysis and high precision mass determination. Furthermore, the possibility of operating the nano-QCM wirelessly enables it to be used in non-invasive sensing in controlled biological testing environments.

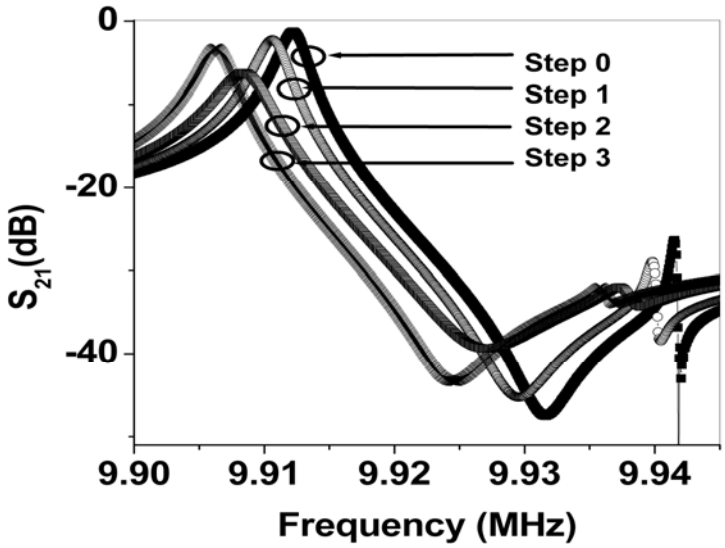

Fig. 5.4. Frequency response (S_{21}) of the nano-QCM, (Step 0) nano-QCM only, (Step 1) linker coating on ZnO, (Step 2) DNA immobilization, and (Step 3) DNA hybridization. Ref. [8]

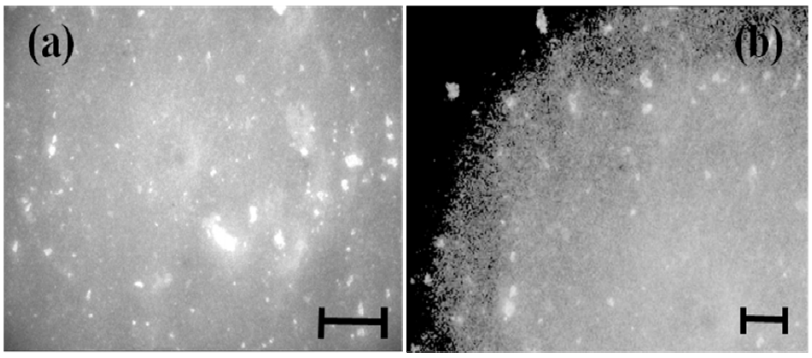

Fig. 5.5. (a) Fluorescence image (bar is 50μm) of the nano-QCM device sensing area (center region) after DNA hybridization; and (b) fluorescence image (bar is 100μm) of the edge of the sensing area revealing binding only at the nanotip sites. Ref. [8]

5.2 The Cell Monitoring System Using the ZnO_{nano}-QCM

After we have demonstrated the biosensing ability of the ZnO_{nano}-QCM device to detect static biomolecules (nonliving), we employ it to perform dynamic and noninvasive monitoring of the adhesion and proliferation of living bovine aortic endothelial cells (BAEC). In the subsequent sections we will compare the performance of a standard QCM with the ZnO_{nano}-QCM in detecting real-time data from viscoelastic transitions occurring during cell adhesion and proliferation on the sensing areas of both devices.

5.2.1. The Cell Culture Protocol

The cell line used for all experiments was bovine aortic epithelial cells (BAEC). All cells were maintained in the standard humidified incubator (5% CO_2 and 95% air) at 37^{o}C. The cells were grown in low glucose Dubelcco's modified eagle medium (DMEM) supplemented with 1% L-Glutamine, 1% bovine brain extract (BBE) (Clonetics, Inc.), 0.5% Heparin, 10% fetal bovine serum (FBS), and 0.4% of 10,000 U/ml

penicillin and 10,000 mg/ml streptomycin solution. The cell culture was trypsinized and diluted for re-seeding after ~85% confluency was reached.

Fibronectin was used to facilitate the cell anchorage to the sensor surfaces (both standard QCM and ZnO_{nano}-QCM). The fibronectin solution used for the surface treatment of the standard QCM and ZnO_{nano}-QCM was prepared using 1mg of human fibronectin (BD Biosciences) diluted into 1mL of PBS buffer solution. 50μL of this solution was applied to the sensing area of the (0.2047 cm^2) of the QCM and ZnO_{nano}-QCM. This ensures the area-density of the fibronectin on the devices to be 5μg/cm^2, which is the optimal amount determined experimentally.

After full confluency of the cell culture, fluorescence microscopy was used to monitor the cells grown on the sensors samples. Since the ZnO_{nano}-QCM and standard QCM are optically opaque, in order to confirm the growth of living cells on the ZnO_{nano}-QCM after the entire monitoring cycle, the growth medium was modified with a fluorescent living-cell tracer (Cell Tracker Orange CMRA) by preparing a 1:5 solution of CMRA fluorescent tracker and dimethyl sulfoxide (DMSO) to the growth medium. The fluorescent-tagged living cells growing on the active sensing area of the device were imaged using an Axiovert 200M confocal fluorescence microscope (Zeiss Axiovert 200M, Gottingen, Germany) with a 548 nm filter and 576 nm excitation to obtain reflection type fluorescence images.

5.2.2. System Structure, Characterization Setup

Cell Monitoring System: The ZnO_{nano}-QCM device consists of ZnO nanostructured arrays that are integrated on a standard AT-cut QCM. The ZnO

nanostructures are directly grown on the sensing area of the QCM through a shadow mask using MOCVD. The optimal ZnO nanostructure morphology was determined through the control of the MOCVD growth conditions described in Section 3.2. The ZnO nanostructure layer has thickness of ~500 nm. The ZnO-covered sensing area was exposed to UV light to make it super-hydrophilic. The combined effect of giant surface area of the nanostructures and superhydrophilic state makes the ZnO_{nano}-QCM a very sensitive mass measuring device as well as a monitoring device for viscoelastic transitions in the sample. The operating frequency of the standard QCM is 10 MHz, while the ZnO_{nano}-QCM has an operating frequency of 9.916 MHz.

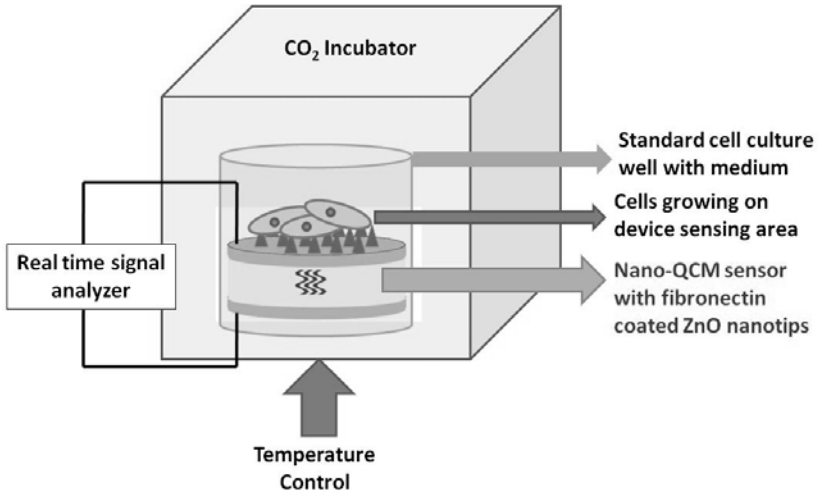

Fig. 5.6. Setup for deploying the ZnO_{nano}-QCM biosensor for noninvasive and dynamic cell growth monitoring. Ref. [46]

The ZnO_{nano}-QCM was then deployed inside a Teflon cell-growth well to serve as the test device (Fig. 5.6), while a standard QCM was inserted in a similar Teflon cell-growth well to serve as the reference device. The reference and test devices were both

sterilized with ethanol and de-ionized water, then surface-treated with human fibronectin. The Teflon well was filled with growth medium, and seeded with bovine aortic endothelial cells (BAEC). They were then placed in a standard CO_2 incubator for an average of 50 hours. The acoustic admittance spectra of the deployed devices were measured in real-time for an average of 50 hours while the cells were actively growing on each device.

Setup for Dynamic Measurements and Data Analysis: The characterization and testing of the ZnO_{nano}-QCM and standard QCM devices were conducted using an HP 8573D Network Analyzer (Agilent Technologies, Palo Alto, CA). The acoustic admittance (Y) spectrum of the device was automatically measured in every half-hour interval while the BAEC cells were growing on the ZnO_{nano}-QCM sensor inside the incubator. The final output of the ZnO_{nano}-QCM cell monitoring sensor is in the form of time-frequency 3D signals that contain multiple parameters in a single monitoring period, namely (i) peak frequency shift, (ii) motional resistance, (iii) motional inductance, and (iv) spectral shape evolution. Each of these parameters are analyzed for correspondence to the dynamic behavior of cell adhesion and proliferation and they are discussed in Section 5.3.

5.2.3. Enhanced Viscoelastic Transition Detection Using ZnO_{nano}-QCM

The ZnO_{nano}-QCM device with the optimized ZnO surface morphology (rough ZnO surface) was utilized to monitor adhesion and proliferation of the cells. The control (standard QCM) and test (ZnO_{nano}-QCM) devices were set up as described in the previous section. The devices were both surface treated with fibronectin, filled with growth

medium and stand for an hour in the incubator to let the devices reach stability, and for the medium to reach stable and suitable pH level before the growth wells were seeded with BAEC cells. The devices were seeded with cell density that would be fully confluent in approximately 45-50 hours. While the cells were growing on each device, we continuously measured the sensor's admittance parameter $Y(\omega)$ for half-hour intervals. A rough analysis of the real part of the time-evolving $Y(\omega)$ spectrum of both the standard QCM and the ZnO_{nano}-QCM reveal that the ZnO_{nano}-QCM exhibits an enhanced sensitivity of cellular growth activity (Fig. 5.7(a) and 5.7(c)). The ZnO_{nano}-QCM spectrum visibly shows modulation of the admittance amplitudes while the standard QCM spectrum does not show any change. However, the fluorescence image of both devices taken after 50 hours (Fig. 5.7(b) and 5.7(d)) show that the cell culture reached full confluency on both devices.

The time-evolving resonance frequency shift $\delta f(t) = f_0 - f(t)$ of both devices were monitored, where f_0 is the resonant frequency of the device before cell seeding and $f(t)$ is the subsequent resonant frequency of the device after a time t. Fig. 5.8 shows the plot of $\delta f(t)$ for both devices. The most evident feature of this plot is the enhanced sensitivity of the ZnO_{nano}-QCM over the standard QCM where the maximum frequency shift at confluence of the ZnO_{nano}-QCM is ~10 times larger than the standard QCM. This can be attributed to the giant effective surface area made available for cell attachment to the ZnO nanostructures on the sensing area of the ZnO_{nano}-QCM device. According to (Heitman *et. al.*, 2007), the detectable activity of cell growth on the QCM-type devices only happens at the interface of the cells and the sensing area. Adding the ZnO nanostructures to the QCM sensing area enhances this interfacial interaction by providing a huge

effective sensing area for the device. The ZnO_{nano}-QCM device also exhibits a linear cell proliferation from initial seeding before it tapers off at 40 hours when the cells reach full confluency. The standard QCM on the other hand shows nonlinear proliferation rate (Fig. 4 inset) and reaches confluency early at 25 hours of incubation.

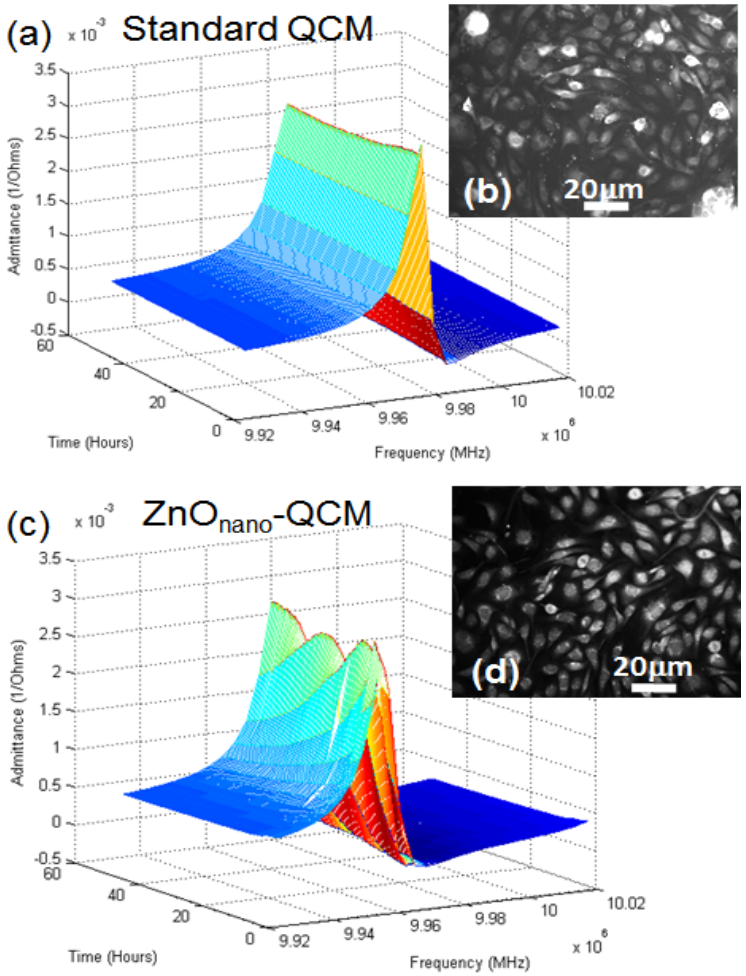

Fig. 5.7. (a) The time-evolving admittance spectra of the standard QCM, (b) 20x fluorescence image of the BAEC cells in full confluency on the sensing area of the standard QCM; (c) time-evolving admittance spectra of the ZnO_{nano}-QCM, and (d) 20x fluorescence image of the ZnO_{nano}-QCM sensing area showing full confluency. Ref. [46]

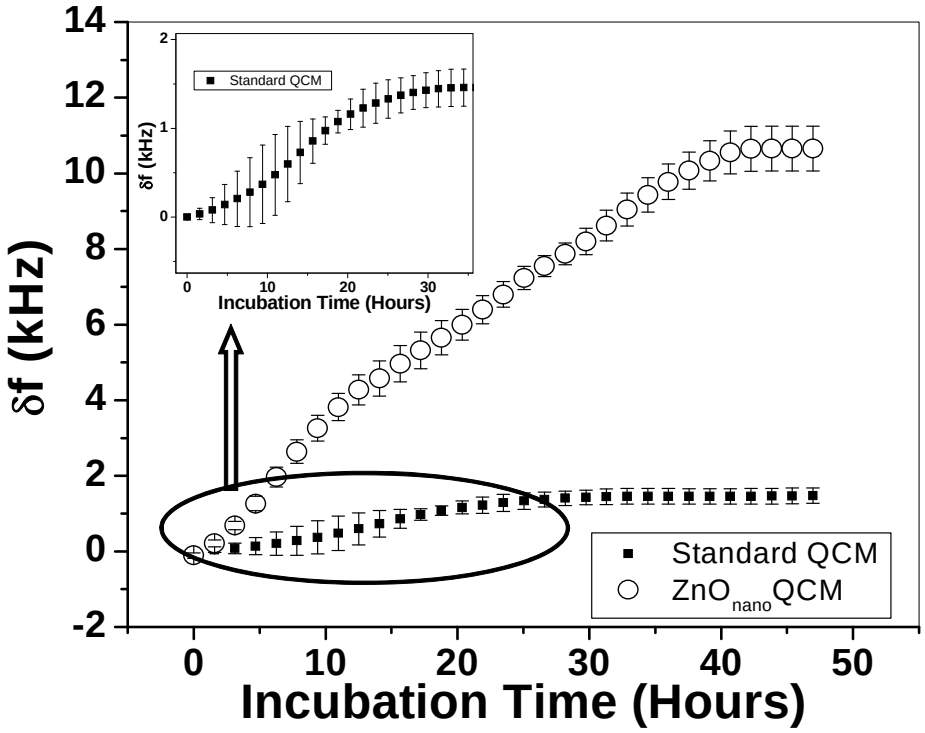

Fig. 5.8. The time-evolving frequency shift (deviation from resonance frequency) for the standard QCM (solid squares), and the ZnO_{nano}-QCM showing ~10 times enhanced sensing performance by the ZnO_{nano}-QCM. Ref. [46]

5.3. Multi-Parameter Extraction Using the Butterworth Van-Dyck Model

We need to establish the correspondence between the time-evolving admittance measurements from the ZnO_{nano}-QCM (which is an electrical parameter) with the mechanical parameters at the sensing area. The transmission line model of the basic QCM outlined by [91] was used to show the correspondence. The model is adapted to our cell monitoring system which consists of four mechanical transmission line impedance layers as depicted in Fig. 5.9(a): (i) the basic QCM layer described by its

characteristic impedance Z_Q and the coupling coefficient of quartz K^2, (ii) the ZnO nanostructure layer modeled as an ideal rigid mass layer described by the ZnO density ρ_{ZnO}, (iii) the biological cell layer modeled as a finite thickness viscoelastic film described by the cell density ρ_{cell} and the complex shear modulus $\mathbf{G}_{\text{cell}}$, and (iv) the cell growth medium modeled as a semi-infinite Newtonian fluid described by its density ρ_{medium} and viscosity coefficient η_{medium}. Layer (i) is treated as the basic device, and layers (ii)-(iv) are mechanical load impedances. If a small-load assumption is used, i.e. total load density is less than 5mg/cm^2 and the total viscosity is less than 10^3 g^2/cm^{4}s, then the entire transmission line model can be simplified into a lumped-parameter circuit equivalent called the Butterworth-Van-Dyke (BVD) lumped-parameter model [91,92]. This assumption is also valid for cell growth [92]. The BVD equivalent circuit of the nano-QCM is shown in Fig. 5.9(b), which is composed of a RLC circuit in series with a load impedance Z_{Load} (which includes the contribution due to the ZnO nanostructure, cell layer, and the growth medium), and in parallel with a capacitor $C_{0,}$ which represents the total capacitance of the dielectric quartz sandwiched between two Au electrodes. This capacitance describes the basic characteristics of the basic QCM far from the resonance frequency. The branch of the circuit that represents the motional characteristics of theZnO $_{\text{nano}}$-QCM near and at the resonance frequency is the load impedance with the series RLC circuit, composed of R_{QCM}, L_{QCM}, and C_{QCM}, the motional resistance, inductance and capacitance of the quartz resonator at no load, respectively. When the basic QCM experiences mechanical perturbations due to a collective load placed on its sensing electrode, the load impedance Z_{Load} takes effect. The load impedance can be further represented by a series RL circuit (R_{Load} and L_{Load}) and is given by:

$$Z_{Load} = R_{Load} + j\omega_o L_{Load} \tag{5.2}$$

where ω_o is the resonant frequency of the device. The electrical parameter (Z_{Load}) is directly related to the mechanical impedance experienced by the acoustic wave due to the physical perturbations occurring at the attached overlaying material given by the expression (Wegener *et. al*., 2000)

$$Z_{Load} = \frac{1}{Y_{Load}} = \frac{\pi}{4K^2\omega_0 C_0}\frac{Z_{mechL}}{Z_{QCM}} \tag{5.3}$$

where K^2 is the coupling coefficient of the piezoelectric quartz layer, Z_{mechL} is the mechanical impedance due to the ZnO layer + cellular layer + growth medium attached to the sensing area, and Z_{QCM} is the impedance the QCM at no load. Eq. (5.4) and (5.5) give the expressions for R_{Load} and L_{Load} and are related to the measured admittance parameter by:

$$R_{Load} = \frac{\pi}{4K^2\omega_0 C_0}\frac{\mathrm{Re}\{Z_{mechL}\}}{Z_{QCM}} = \frac{\mathrm{Re}\{Y_{Load}\}}{\mathrm{Re}^2\{Y_{Load}\} + \mathrm{Im}^2\{Y_{Load}\}} \tag{5.4}$$

$$L_{Load} = \frac{\pi}{4K^2\omega_0 C_0}\frac{\mathrm{Im}\{Z_{mechL}\}}{Z_{QCM}} = \frac{-\mathrm{Im}\{Y_{Load}\}}{\omega_0\left(\mathrm{Re}^2\{Y_{Load}\} + \mathrm{Im}^2\{Y_{Load}\}\right)} \tag{5.5}$$

The quantity R_{Load} corresponds directly to the mechanical or motional resistance and designates dissipation of acoustic energy due to the attached cell growth layer on the nano-QCM surface. The parameter L_{Load} on the other hand is directly proportional to the stored energy by the cell layer (i.e. elasticity increase). Y_{Load} is the measured admittance spectrum minus the no-load admittance spectrum of the standard QCM. Adapting our cell monitoring setup to the Z_{mechL} expression developed by Bandey [91], the mechanical impedance becomes a combination of the mechanical effects derived from the mechanical model in Fig. 5.9(a) and is given by Eq. (5.6)

$$Z_{MechL} = j\omega\rho_{ZnO} + Z_{cell}\left[\frac{Z_{Medium}\cosh(\gamma_{cell}h_{cell}) + Z_{cell}\sinh(\gamma_{cell}h_{cell})}{Z_{cell}\cosh(\gamma_{cell}h_{cell}) + Z_{Medium}\sinh(\gamma_{cell}h_{cell})}\right] \quad (5.6)$$

where $j\omega\rho_{ZnO}$ represents the impedance of the rigid ideal mass ZnO nanostructured layer, $Z_{Cell} = \rho_{Cell}G_{Cell}$ is the impedance of the finite-thickness (h_{cell}) viscoelastic cell layer, and $Z_{mediium}$ is the impedance of the growth medium as a semi-infinite Newtonian fluid, which is given by

$$Z_{Medium} = (1+j)\sqrt{(\omega\rho_{medium}\eta_{medium}/2)} \quad (6)$$

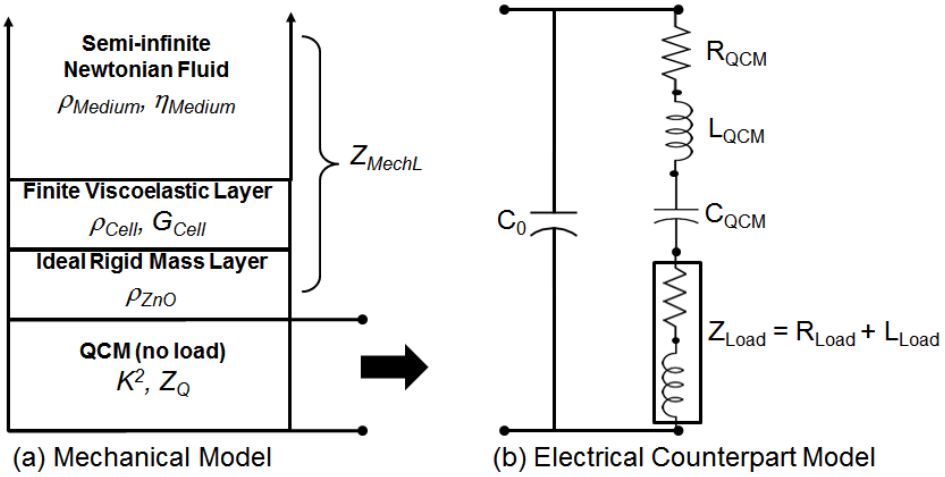

Fig. 5.9. (a) The mechanical impedance model of the ZnO_{nano}-QCM cell monitoring system (b) the corresponding lumped-element equivalent circuit of the Butterworth-Van-Dyke (BVD) of the nano-QCM cell monitoring system with the load resistance and load inductance representing the electrical counterpart of the mechanical load on the top electrode. Ref. [46]

To isolate the effects of the ZnO layer and the growth medium (and also obtain empirical values for the BVD parameters for these layers) we measured the admittance parameter of the ZnO_{nano}-QCM right after the ZnO nanostructure deposition on the

sensing electrode to show that the only effect the ZnO layer does on the signal is to introduce a Sauerbrey frequency shift as shown in Fig. 5.10(a). This confirms that the ZnO nanostructure layer indeed behaves like an ideal rigid mass and does not contribute to the viscoelastic transitions. Next, we monitored the admittance spectrum of the ZnO_{nano}-QCM with the growth medium and fibronectin in the container for 20 hours. Fig. 5.10(b) shows that the time-evolving admittance spectra do not change for the whole monitoring duration except a reduction in the signal amplitude compared to the device without the growth medium. This means that the growth medium also does not contribute to the viscoelastic transitions occurring in the cell monitoring setup. Both sets of signals (Figs. 5.10(a-c)) provide the baseline signals which verify that the changes we observed in the time-evolving admittance spectra are only due to the viscoelastic cell layer.

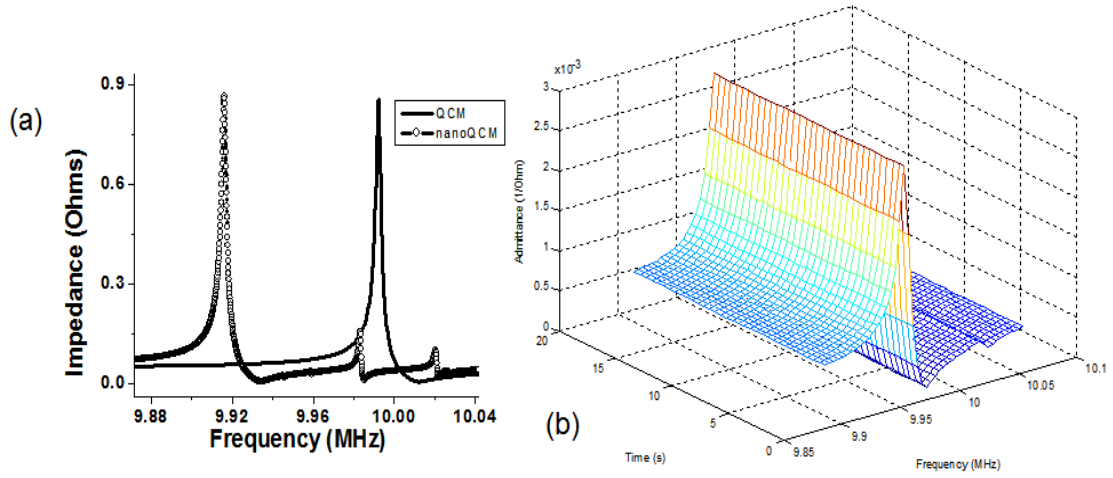

Fig. 5.10. The impedance spectrum of the standard QCM (a) (solid line), the ZnO_{nano}-QCM (after ZnO nanostructure deposition) (c) (circles), and (b) the time-evolving admittance spectrum of the same ZnO_{nano}-QCM with the fibronectin and growth medium. Signals from both (a) and (b) show no dynamic changes therefore can be subtracted as background signals. Ref. [46]

We used Eq. (5.4) and (5.5) to generate the motional resistance and inductance plots that relate the measured admittance spectra to the viscoelastic changes happening during the cell growth process monitored by the ZnO_{nano}-QCM. Fig. 5.11(a) shows the motional resistance of the ZnO_{nano}-QCM for the 50-hour cell growth monitoring period. The inset shows the same parameter for the standard QCM. The most obvious information derived here is the highly enhanced sensitivity of the ZnO_{nano}-QCM compared to a standard QCM in detecting viscoelastic transition. For the standard QCM, the total change in motional resistance ΔR_{total} was only 1.5kΩ, while for the ZnO_{nano}-QCM it was 37.5kΩ which is 25 times higher than the standard QCM. Fig. 5.11(b) shows the motional inductance experienced by the nano-QCM due to the cell growth. Fig. 5.11(a) and (b) reveal certain details about the cell growth on the ZnO_{nano}-QCM sensor. L_{Load} increases continuously from 0 to 50 hours while R_{Load} changes in different time intervals. From 0 to 6 hours the R_{Load} decreases from 8kΩ and settles to 2.5 kΩ from 6-15 hours. This indicates a small energy dissipation due to the low value of R_{Load}. This may be due to the cells settling on the ZnO nanostructured surface but have not adhered to the surface yet. For the time interval 15-40 hours there is a rapid increase in the value of R_{Load} indicating a high energy dissipation that may be caused by the formation of more rigid focal adhesion points by the individual cells, and the onset of proliferation. At 40 hours onwards, the value of R_{Load} further increases faster indicating further energy dissipation due to the rigid attachment of the cells to the nanostructures but having an increased amount of viscoelastic bodies attached to them from cell crowding. This increase in energy dissipation is caused by the dampening of the shear waves induced by the large amount of cellular proliferation. Fig. 5.11(c) shows a plot of the motional

resistance versus motional reactance. The upward curvature $\frac{\partial^2 R_{Load}}{\partial(\omega L_{Load})^2} > 0$ indicates that the energy loss per unit mass of the cells increases with the cell culture proliferation. The solid lines in Fig. 5.11(a) and (b) represent the BVD fitting curves derived from empirical parameter fitting of the individual layers in the BVD model. The BVD model curves agree with the measured parameters; however, they do not closely fit because we did not include the energy lost to the transverse component of the acoustic waves that could be introduced by the ZnO nanostructures.

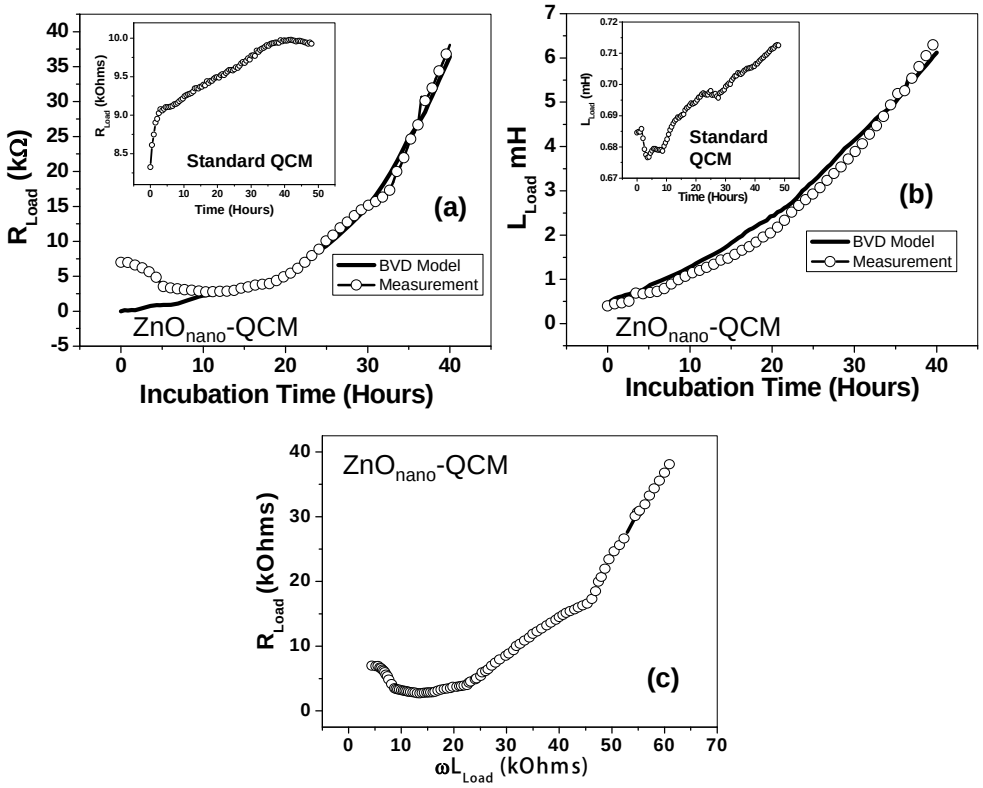

Fig. 5.11 . (a) The time-evolving load resistance of the ZnO_{nano}-QCM due to the adhering and proliferating cells and inset: the load resistance change in the standard QCM; (b) The time-evolving load inductance of the ZnO_{nano}-QCM and inset: the load inductance change in the standard QCM; (c) the load resistance versus reactive load plot of the ZnO_{nano}-QCM showing an upward curvature. Ref. [46]

5.4. Summary

The integration of ZnO nanostructures and a standard QCM forms a surface-modified QCM biosensor (ZnO_{nano}-QCM), which possesses significantly enhanced sensitivity over the conventional QCM counterpart. The nano-QCM biosensor is installed *in situ* using a standard cell culture environment for noninvasive and dynamic cellular monitoring. We have demonstrated the controlled adhesion and proliferation of BAEC cells on the nanostructured ZnO surface with the optimized surface morphology. The ZnO_{nano}-QCM exhibited enhanced sensitivity to detection of cell adhesion, proliferation, and viscoelastic transitions through a single measurement of time-frequency 3D acoustic spectra. The ZnO_{nano}-QCM shows 10 times increased sensitivity in frequency shift due to total cell proliferation in comparison with the standard QCM. The Butterworth-Van-Dyke (BVD) lumped-parameter model analysis was applied to the measured acoustic spectra to extract dynamic information from the signal's spectral shape evolution, peak frequency shift, and amplitude modulation. The presented technology provides a base for noninvasive, real-time, dynamic and label-free cellular monitoring

Chapter 6

Sensor-on-Food Package Using a ZnO Surface Acoustic Wave (SAW) Device on Zein-Coated Flexible Substrate

There has been growing interest for innovative food packaging technologies due to the increasing complexity of consumer needs and regulatory requirements for food products. Requirements such as biodegradability, longer shelf-life, spoilage detection and contamination monitoring, have led to the active exploration of a new-generation intelligent food packaging technology [93], which involves embedding various sensing devices onto food packaging materials. One of such efforts includes a food package with gas indicators, primarily oxygen detectors to alert microbial spoilage and to rejuvenate the packaging's internal environment [94,95]. However, such oxygen detection is realized externally through measurements of the emissions of optically excited luminescent probes embedded in the package. Humidity sensors consisting of capacitive, resistive, or acoustic wave devices are promising for food freshness detection [96], as relative humidity inside the food package is one of the widely-used standard indicators of food freshness, for example, packaged fresh fruits and vegetables need high humidity, while dry goods require only low humidity. However, such humidity sensing devices have not been embedded into the food packaging. Previously-developed types of intelligent packaging involve food packages with colorimetric labels to indicate oxygen reaction [97] and time-temperature indicators [98]. These labels which are deployed inside the package contain colorimetric dyes that distinctly change color when a gas such

as oxygen is detected, or the labels could exhibit diffusion of dye particles to indicate the history of temperature for a particular package. However, these types of sensors do not quantify the amount of gas it detects. The sophisticated sensors such as “electronic noses” and “electronic toungues” have been developed to detect various biochemicals that cause the spoilage of food [99,100,101]. However, these devices are highly complex therefore expensive, and the sensing is done outside the food package. This requires tampering food package, taking a sample of the contents, applying it to sensor for diagnosis, which is an invasive and tedious method.

In this chapter, we demonstrate a promising intelligent food packaging platform consisting of a ZnO surface acoustic wave (SAW) sensor built on zein-coated flexible substrates. The platform combines the unique wireless sensing capability of piezoelectric ZnO with the edible, anti-microbial and biodegradable properties of zein.

6.1 ZnO/Zein/Flexible Substrate Platform

Due to its well-known piezoelectric properties, ZnO has been widely used in SAW and BAW devices in communication applications. ZnO SAW sensors have been demonstrated for toxic and combustible gas sensing, as well as organic gas molecules as shown in earlier sections. ZnO has also been used as a sensitivity-enhancing material for an AlN/ZnO-based SAW humidity sensor [102]. These ZnO-based SAW sensors have the advantage of being operated wirelessly with low power consumption. ZnO can be bio-functionalized to specifically bind to various types of biochemicals. So far, ZnO SAW devices are built on rigid substrates including Si, quartz, glass, etc. However, there

has been no report on the SAW sensing devices directly built on the flexible biopolymer substrates.

Zein is a prolamin protein extracted from maize, which is a promising biopolymer for future renewable food packaging material. Zein can be shaped into a uniform structure, being a tetramer formed by individual zein cylinders through α-helix folding [103]. The conformation of zein's uniform structure can be tuned by different solvents [104]. In addition to its featured structure, zein has many advantages over other biopolymers, including toughness, hydrophobicity, greaseproof, anti-microbial function, and convenience for film-making [105]. These intrinsic properties make zein a highly suitable coating material for food packaging. This is particularly advantageous as a protective layer of the packaging, which maintains the internal humidity of the package and simultaneously protects food matrix from external microbial attack.

The combination of ZnO and zein into an intelligent packaging platform provides both the food freshness monitoring and food protection. To the authors' knowledge, there has been no report so far of any sensors being embedded onto zein. It is recognized that the humidity and temperature of the internal environment of the food packaging are main parameters determining the freshness of the packaged food [106] specifically for fresh produce, such as fruits and vegetables. The ZnO/zein platform is used to perform the humidity sensing. It promises to enable smart embedded wireless sensor-on-food-packaging (SOFP)

6.1.1. Material Preparation

Zein Film Preparation: In this work, the zein films were prepared using zein powder (Wako Corporation), and AcOH (ACS reagent grade >99.7%) from Sigma-Aldrich, Inc

(St. Louis, MO). Milli-Q water was utilized throughout the entire material preparation. Zein was dissolved in acetic acid and then spin-coated onto polyimide flexible substrates for the demonstration of the ZnO-SAW on zein-coated food packaging humidity sensing. Zein was also coated on silicon (Si) for characterization and processing control. The spin-coating was done using a Laurell model WS-400A-6NPP/LITE spin coater (Laurell Technologies Corp., North Wales, PA). Different spinning speeds were applied to control the thickness of Zein film on the substrates.

ZnO Thin Film Deposition [107]: The ZnO films were deposited using the RF magnetron sputtering technique. The sputtering targets were prepared by sintering pure ZnO powders mixed with Ni (~2% wt.) which serves as the compensation doping to achieve the piezoelectric ZnO films. Before deposition, the sputtering chamber was kept at a vacuum level of ~5.0 x 10^{-6} torr. During deposition, a mixed Ar and O_2 gas (ratio of 1:1) was fed into the chamber, the processing pressure of the chamber was maintained near 7.5 x 10^{-3} torr. The substrate temperature was kept at 120 ˚C, which was low enough to prevent the denaturation of the protein substrate. The deposition rate was approximately 1.0 μm/hr. The film thickness was in a range of 0.5 μm to1.5 μm for characterizing the SAW behavior in ZnO/zein/Si and ZnO/zein/flexible substrate structures. A ZnO thickness of 1.0 μm was deposited on the zein films on the polyimide flexible substrate for the sensor on food package demonstration.

In order to characterize the crystal quality of as-grown ZnO films on zein, X-ray diffraction (XRD) θ-2θ scan was performed on a Siemens D500 x-ray diffractometer by using Cu Kα radiation. The result is shown in the Fig. 6.1(a), wherehe ZnO (0002) peak

at about 34.7° is dominant against other ZnO peaks, indicating the polycrystalline structure with preferred c-axis orientation.

The surface morphology of ZnO thin film deposited on zein was characterized by using both tapping mode-atomic force microscopy (TP-AFM) and field emission scanning electron microscopy (FESEM). AFM top-view images were collected in tapping mode by using the NanoScope IIIA Multimode AFM (Veeco) with silicon-etched RTESP7 cantilever (Veeco Nanoprobe). The SEM images were taken by using a Zeiss Sigma field emission SEM system.

Fig. 6.1(b) shows the FE-SEM cross-section image of the ZnO thin film deposited on the zein layer, while Fig. 6.1(c) exhibits the TP-AFM height image of the same sample. Fig. 6.1(d) on the other hand shows the TP-AFM height image of the zein surface prior to the ZnO deposition. From both the AFM and SEM images, it is clear that ZnO forms dense and homogeneous films with closely packed columnar structures that aligned along the *c*-axis. The root-mean-square roughness of the ZnO film to be ~ 8.3 nm, determined by using software included with the AFM machine.

It is found that the adhesion of the two layers is strong due to the binding between ZnO and zein. During the RF magnetron sputtering process, a significant amount of oxygen gas was purged into sputtering chamber. The increased amount of oxygen onto zein surface generated more amount of carboxylic acid groups (-COOH) on zein. Those carboxylic acid groups can interact with ZnO through salt bridging, forming Zn-OOC binding. It was also reported that carboxylic acid groups (-COOH) facilitate a highly oriented growth of ZnO crystals [9,108].

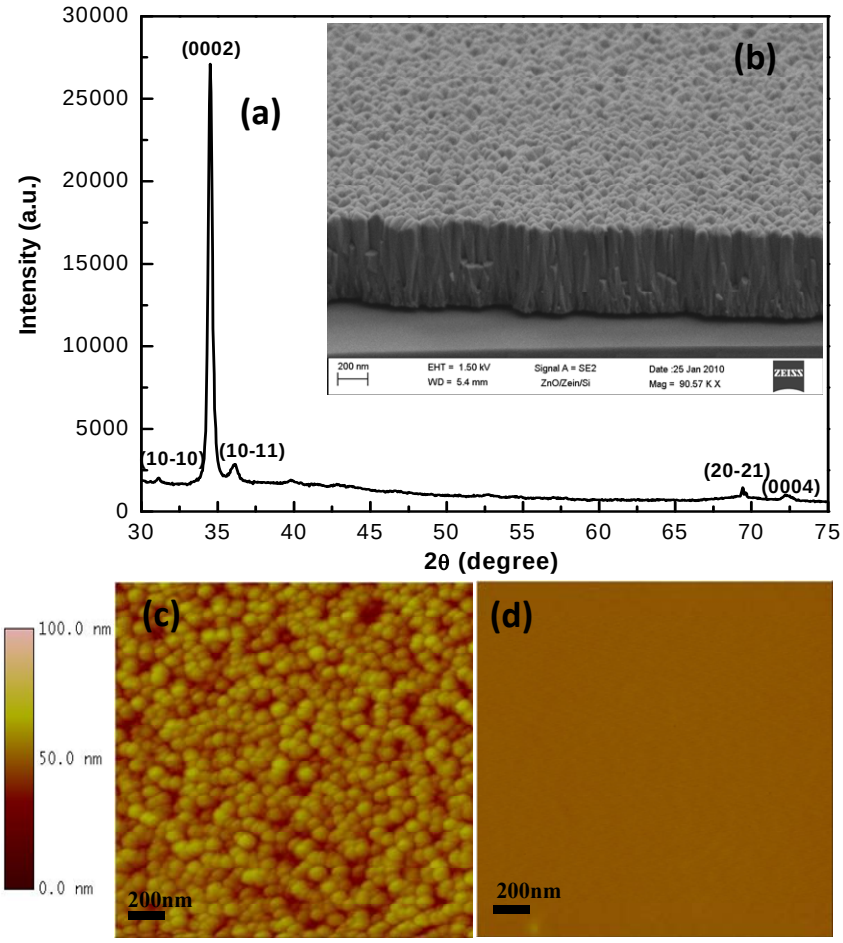

Figure 6.1. (a) X-ray diffraction pattern of ZnO sputtered on Zein/Si showing the ZnO (0002) peak at 34.7^{o} which indicate the c-axis oriented crystal structure of ZnO; (b) FE-SEM image of the cross section of the ZnO thin film deposited on Zein showing the surface morphology of the ZnO film (c) TP-AFM height image of the same ZnO film on Zein with 2µm×2µm scan size (small scan size is used for ZnO sample to view nano-structure more clearly); (d) TP-AFM height images of pure Zein surface with 10µm×10µm scan size. Ref. [107]

6.1.2. Control of ZnO Surface Wettability

The ZnO thin films deposited on Zein/Si and Zein/flexible substrate were analyzed for surface wettability using a Model 500 Advanced Goniometer from Ramé-

Hart Instrument Co. Lakeview NJ. The water droplet was dispensed onto the surface of the samples using the instrument's automated micro-liter dispensing system and the image of the drop was captured in real time by the instrument's CCD camera. Image analysis, baseline determination and contact angle measurements were performed using Image-Drop Advanced analysis software. UV irradiation on the ZnO thin films grown on zein was conducted to achieve surface hydrophilic status. A 1μL water drop was placed on the as-deposited ZnO thin film on zein/Si and zein/flexible substrate, and the measured contact angle was found to be 50.6^{o} and 57.4^{o}, respectively. The difference in the contact angles resulted from the different surface morphologies of the two structures. The same samples were then irradiated with UV light from a lamp (Model 66002, Oriel Optics, Stratford CT) to make the ZnO films hydrophilic. After 10 minutes irradiation, the contact angle reduced to 23.4^{o} for the ZnO on zein/Si sample while the contact angle reduced to 21.6^{o}, which shows a transition of the samples to hydrophilic state. Such wettability change benefits the humidity sensor based on the ZnO/zein/flexible substrate by increasing its ability to absorb more moisture.

6.2. SAW Characteristics of the ZnO/Zein Structures

We used the ZnO films grown on the zein/flexible substrate samples to perform a characterization of the SAW propagation properties on the ZnO/zein layers. A set of aluminum (Al) interdigital transducer (IDT) pairs of various wavelengths (λ=6, 8, and 10 μm) were deposited on each of the ZnO/zein/flexible substrate samples with various ZnO thicknesses. There are 20.5 electrode pairs (41 electrodes) for each IDT. The delay line with IDT center-to-center distance of 1000 was used for each IDT wavelength. The IDT apertures were 180 μm for all devices. Electrode length is 178 μm, end gap is 2 μm, IDT

to shorting surface distance is ¼ λ, and metallization ratio (metal surface to total period surface ratio) equals to 0.5. The schematic of the cross section of the SAW device is shown in Fig. 6.2(a) and the top-view is shown in Fig. 6.2(b). The devices were tested using a Cascade Microtech probe station with Cascade Microtech Air Coplanar Probes, and a HP 8753D network analyzer. The transmission spectrum (S_{21}) of the devices were measured and the SAW center frequencies were determined from the spectrum. The acoustic velocities for the propagating SAW modes were calculated using the relation $v_{SAW} = \lambda_o f_c$ where λ_o is the IDT periodicity and f_c is the center frequency of the propagating SAW modes.

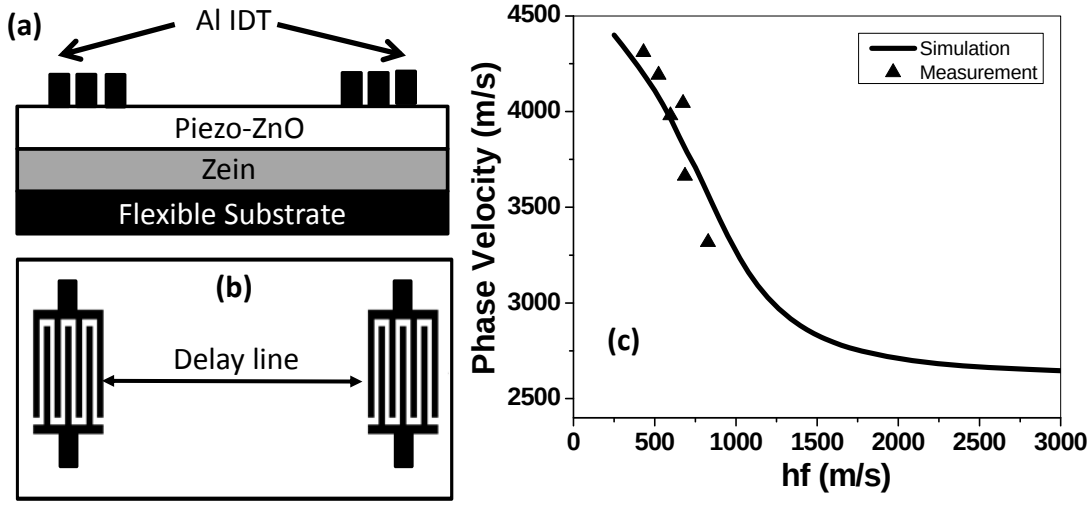

Fig. 6.2. The schematic of (a) cross-section and (b) top veiw of the ZnO grown on the zein/Si substrates that are used for SAW propagation characterization; (c) plot of the phase velocity versus thickness-frequency product of the SAW modes propagating in the ZnO/zein/Si system (solid line represents simulation results and solid triangles denote experimental data). The measured data follow closely the theoretical graph. Ref. [107]

For simulation of the SAW modes propagating in the ZnO/zein samples, we used the published values of the mechanical parameters of ZnO, zein on our multilayer transmission line (MTL) model in which we consider the acoustic wave propagation through the different layers of the SAW device and calculate the acoustic impedance of the device by treating each layer as a two-port system. Fig. 6.2(c) shows the result of the simulation of the SAW phase velocity as a function of the ZnO thickness-frequency product (*hf*). From the simulation curve we can see that the phase velocity would decrease as the ZnO thickness-frequency product hf increases. In the frequency range (hf<1250), the phase velocity drops sharply as frequency increases. In the high frequency range (hf>1250), phase velocity starts to taper off and remains at a fix value as thickness-frequency product reaches higher values. The measured values of the phase velocity for various ZnO thicknesses and IDT periodicities of the ZnO/zein/Si system are plotted simultaneously with the simulation curve and shows good agreement with the theoretical results.

6.3. Humidity Sensors Built on Food Packaging

The SAW characterization results described above are used to design and analyze the SAW device on the ZnO/zein/flexible substrate samples with tailored properties for humidity sensing. The device consists of an open SAW delay line between two inter-digital transducers (IDTs) similar to the one described in the previous section. The schematic of the cross section of the SAW device is shown in Fig. 6.3(a). The photograph of the device on the flexible substrate is shown in Fig. 6.3(b), where the thickness of the ZnO layer is 1.0 μm and the zein coating is 2 μm, respectively. The input and output IDTs consist of electrodes pairs with a periodicity of 6 μm, a center-to-center

delay line distance of 1000 μm. The radio frequency (RF) response measurements were made on the SAW devices using an HP 8573D Network Analyzer (Agilent Technologies, Palo Alto, CA) and a Cascade Microtech probe station (Cascade Microtech Inc. Beaverton, OR). The transmission parameter (S_{21}) freqeuncy response of the SAW device is shown in Fig. 6.3(c). As shown in the figure, the piezoelectric ZnO SAW device fabricated on the Zein/flexible substrate exhibits an operating frequency of ~687.38 MHz, generalized SAW mode (GSAW) with an insertion loss peak of ~25dB and a bandwidth of ~20 MHz at 3dB point. From the IDT wavelength and the operating frequency, the corresponding acoustic velocity on the ZnO/zein/flexible substrate system to be 4124 m/s.

To demonstrate the sensing ability of the SAW device on the ZnO/zein/flexible substrate system, the device was deployed in a chamber fed through with N_2 gas at room temperature. To control the humidity in the chamber, an ultrasonic nebulizer (ETS 572 Ultrasonic Humidification System) was used to introduce water vapor in the chamber at room temperature and 1 atm pressure. Prior to mounting in the humidity-contolled chamber, the SAW device was exposed to UV for ~10 min to make the surface of the open delay line hydrophilic, which increases the sensitivity of the SAW device to the amount of water vapor depositing on the delay line. The effect of changing in the RH values on the SAW sensor results in a shift in the peak frequency. The accumulating moisture on the SAW device changes the acoustic velocity on the ZnO layer just like a nonviscous ideal liquid layer [109]. This introduces a mass-loading effect on the SAW device and a frequency shift will be observed given by the relation $\Delta f/f_0 = \kappa(\Delta v/v_0)$ where Δf is the frequency shift, f_0 is the operating frequency of the SAW device, κ is a device

geometry constant, Δv is the change in the acoustic velocity upon mass loading, and v_0 is the acoustic velocity at no load. The S_{21} parameter of the SAW device was measured for 0% to 90% relative humidity (RH) at room temperature. For only N_2 in the chamber, we did not observe a frequency change for the SAW device, which remained at 687.38 MHz peak frequency corresponding to an acoustic velocity of 4124 m/s. The smallest humidity level that registered a frequency shift was 10% RH corresponding to 3151.22 parts per million by volume fraction (PPMv) sensitivity. The RF spectral responses showing frequency shifts for selected humidity levels (0%, 30%, 60%, and 90%) are shown in Fig. 6.4(a). The plot of the peak SAW frequency as a function of RH is shown in Fig. 6.4(b). The detection range is from 10% RH to 90% RH. This range is well suited for humidity monitoring of fresh unprocessed fruits and vegetables whose optimal packaged humidity should be maintained at ~85% RH to obtain a shelf life of 2-3 weeks [106]. The combination of having the ZnO-based SAW humidity sensor (operating at wireless frequency range) embedded on the flexible substrate that is coated with zein which is an impenetrable moisture barrier and biodegradable coating provides a promising fresh-produce intelligent packaging platform.

The schematic of (a) cross-section and (b) top veiw of the ZnO grown on the zein/Si substrates that are used for SAW propagation characterization; (c) plot of the phase velocity versus thickness-frequency product of the SAW modes propagating in the ZnO/zein/Si system (solid line represents simulation results and solid triangles denote experimental data). The measured data follow closely the theoretical graph.

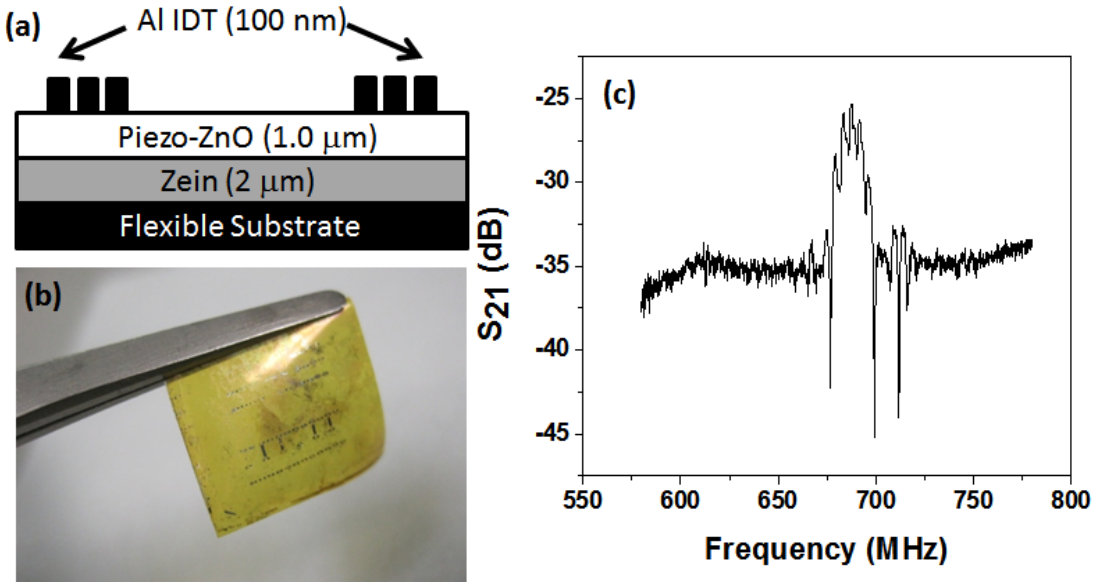

Fig. 6.3. The cross-sectional schematic of the ZnO-based SAW device fabricated on the zein-coated flexible substate, (c) photograph of the device, (d) the transission spectrum (frequency response) of the SAW device showing 687.38 MHz operating frequency. Ref. [107]

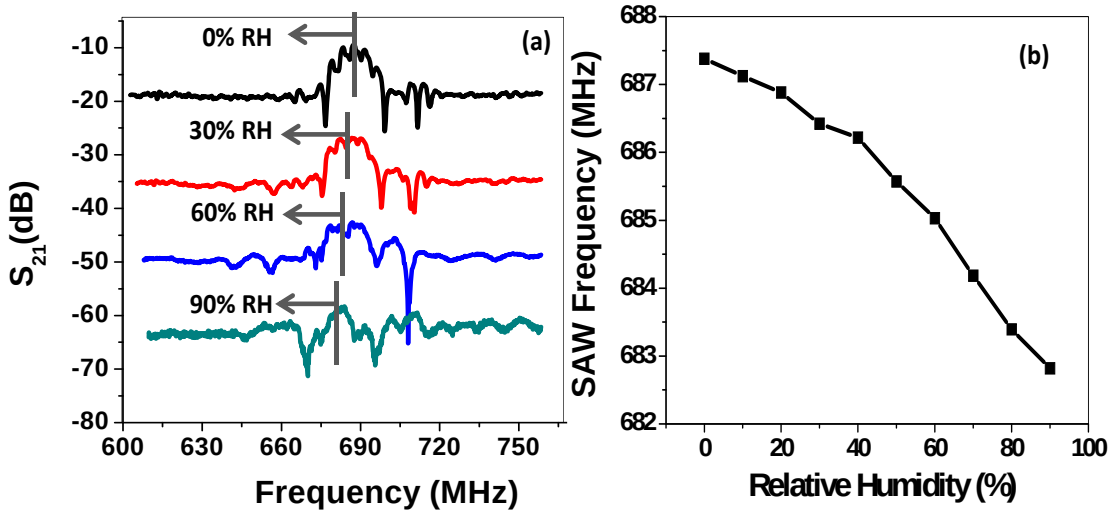

Fig. 6.4. (a) SAW device frequency response for selected RH values, (b) measured SAW peak frequencies as a function of RH values. Ref. [107]

6.4. Summary

Piezoelectric ZnO thin films with the preferred c-axis orientation were deposited on zein-coated flexible substrates at low temperature by RF magnetron sputtering. The ZnO thin film grown on zein exhibits the hydrophilic surface property after UV exposure, which enabled the SAW device to be used as a humidity sensor. The characteristics of the SAW modes propagating in the ZnO/zein system were simulated using multilayer transmission line model and the results have shown close agreement with the measured data. The results of the SAW mode characterization was used to fabricate and demonstrate a SAW humidity sensor built on the ZnO/zein/flexible substrate. The sensor yielded a sensitivity of 3151.22 PPMv and operaates in a humidity range of 10% - 90% RH. The sensor is well suited for detecting the humidity levels of packaged fresh food produce such as fruits and vegetables. The combination of the ability of zein as a moisture protector and ZnO-SAW humidity sensor provides a promising intelligent sensor on food package (SOFP).

Chapter 7

Immunosensors Using ZnO-Based Thin Film Transistors

Electrical-mode biosensors such as transistor-based sensors have been surfacing as an attractive method of biosensing due to their high gain and fast response. Ion-selective field effect transistors (ISFET) has been used popularly as a sensitive pH sensor and various biochemical sensors [110,111,112]. Recently the ISFET structure has been integrated with Poly-Si thin film transistors (TFTs) and GaN/AlGaN high electron mobility transistors (HEMTs) for detection of DNA, penicillin, and cellular potentials [113,114]. However, the sensing procedure using the ISFET can be invasive as its entire gate serves as the sensing area which contains both the analyte solution and the reference electrode. Another class of FET-type biosensors is based on organic field-effect transistors (OFETs) [115,116,117,118]. The general structure of an OFET consists of a back-gate MOSFET with the conducting channel made of organic semiconductors. The OFET has the advantage of being easily controlled through biasing due to the back-gate configuration. However, OFETs require high bias voltages, and suffer from low channel mobility. Currently, nanowire-based FET sensors are demonstrated with high sensitivity reaching the order of fM [119,120]. However, these prototypes of sensors generally involve a complex fabrication process as they are constructed individually by manipulating and aligning a single strand of semiconducting nanowire such as TiO_2 or Si as the FET channel between the source and drain patterns. It is difficult to achieve repeatability and manufacturability in fabrication and integration of these devices for larger sensor arrays. In this chapter, we report the highly sensitive and selective

immunosensing ability of a ZnO based thin film transistor biosensor (ZnO-bioTFT). The EGFR is used as the example because the sensing of EGFR-antibodies reacting with EGFR proteins has its implications in cancer related studies and drug screening for cancer, as EGFR is well-known to be over-expressed in solid tumors, especially breast cancers. The ZnO-TFT devices possess excellent and repeatable characteristics. It can be fabricated using the conventional microelectronic process and can be integrated into a large scale at low cost, which benefit for the further development of a platform not only for diagnosing cancers, but also for monitoring a patient's response to therapy in real-time.

7.1. ZnO bioTFT Device Structure and Characterization

The device schematic is shown as the inset of Fig. 7.1(a) [121]. It follows a back-gate inverted-staggered configuration. A Si substrate was covered with 1 μm layer of SiO_2 through wet oxidation followed by e-beam deposition of a layer of Au (50nm)/Cr (100nm) that serves as the gate electrode. A 70 nm layer of SiO_2 serving as the gate oxide was then deposited through plasma enhanced chemical vapor deposition (PECVD) with substrate temperature of 250 ^{O}C and using SiH_4 and N_2O as the source gases. A 50 nm ZnO thin film was grown using metalorganic chemical vapor deposition (MOCVD) on the top of the SiO_2 to serve as the *n*-type conduction channel, with substrate temperature at 350^{O}C and using diethyl zinc (DEZn) as the metal precursor and ultra-high purity O_2 as oxidizer. Au (50nm)/Ti (100nm) was deposited through e-beam evaporation for the source and drain Ohmic contacts. The exposed ZnO channel acts as the sensing area and has a dimension of 200 μm x 400 μm, giving a W/L ratio of 2. Shown in the inset of Fig.

1(b) is the top view of the TFT device. The electrical characteristics of the ZnO-bioTFT are shown in Fig. 7.1(a-b). The transconductance curve (drain current (I_D) vs gate voltage (V_{GS})) in Fig. 7.1(a) shows that the bioTFT is a normally-OFF enhancement mode transistor with a threshold voltage of 4.25 V and an ON-OFF ratio of ~10^8. The high ON-OFF ratio of the device provides the high sensitivity of the device to the charge modulation within the ZnO channel. Fig. 7.1(b) shows the transistor characteristic curves with drain current versus drain voltage for various gate-biasing of the device.

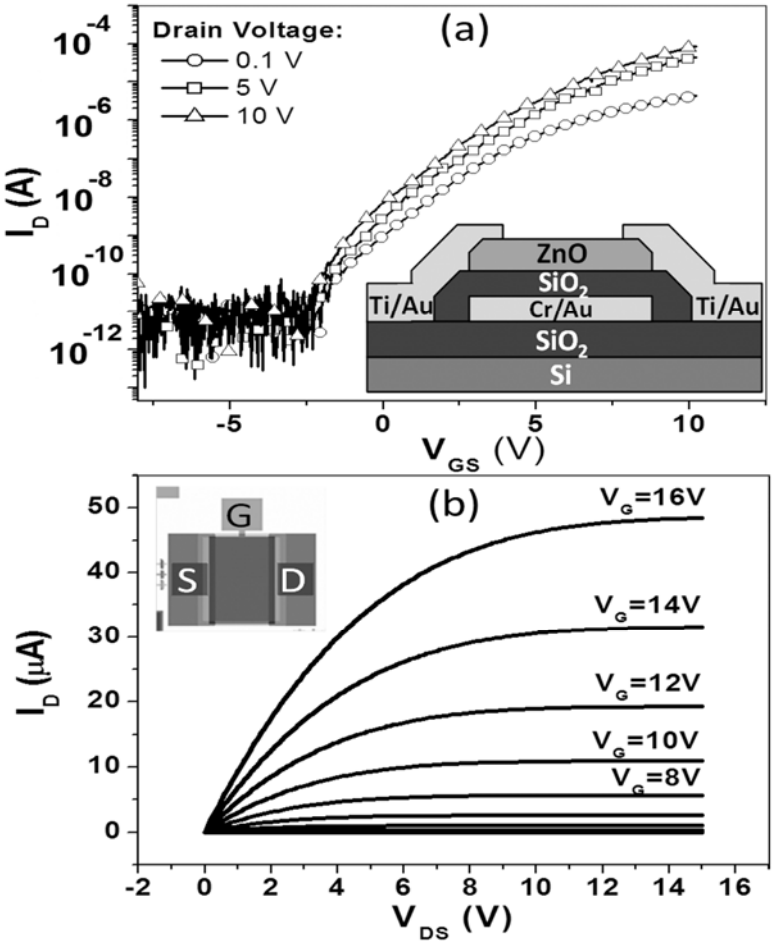

Fig. 7.1. (a) Transconductance curve of the ZnO-bioTFT and its vertical structure schematic (inset); (b) transistor characteristic curves for various gate bias, and the top view of the device (inset). Ref. [121]

7.2. Antibody-Protein Reaction Protocol

To realize the immunosensing ability of the ZnO-bioTFT, the exposed ZnO channel was functionalized using linkage chemistry, which involves three basic steps. First, the ZnO channel was functionalized with trimethoxysilane aldehyde (having a reactive aldehyde end group) by incubating the device in 1% v/v solution of the silane-aldehyde in 95% ethanol for 30 min. The device was then cured at 120°C for 15 min. Second, the aldehyde groups were coupled to the amine groups of the monoclonal EGFR antibodies (1:50) through reductive amination in the presence of 4 mM sodium cyanoborohydride in PBS (pH 7.4) for two hours. Third, unreacted aldehyde groups were blocked using 100 mM ethanolamine in a similar manner to prevent non-specific interactions of proteins. Finally, the device was rinsed in a continuous flow of PBS, pH 7.4 for 10 min.

7.3. Sensing Mechanism Through Pseudo Double-Gating Effect

The bio-functionalization enables the exposed ZnO channel direct interaction with the biochemical species being detected. The mechanism of detection of antibody-antigen reaction is illustrated in Fig. 7.2(a-d). In the first step (Fig. 7.2(b)) the unfunctionalized ZnO-bioTFT is positively biased at the drain and gate electrode. The positive voltage at the gate causes the majority carriers of the *n*-type ZnO channel to accumulate near the base of the ZnO layer to facilitate a conduction path for the current flow from drain to source. The positive voltage at the drain causes some of the carriers to also accumulate near the side of the drain electrode forming a wedge-shaped conduction path. The bias at the drain also acts as the electron pump to drive the current to flow. For the second step

(Fig. 7.2(c)), the exposed ZnO channel is functionalized with EGFR monoclonal antibodies (mAbs) having free lysine groups. The immobilized antibody molecules caused significant decrease in conductivity of the ZnO surface layer, thus, reducing the drain current. In the third step (Fig. 7.2(d)), the EGFR protein captured by the EGFR mAbs forms a polarized molecule with a dominant partially-positive charged tip [122] which led to the accumulation of negative carriers within the ZnO channel to accumulate near the exposed surface where the antibody-protein pairs were present. This carrier

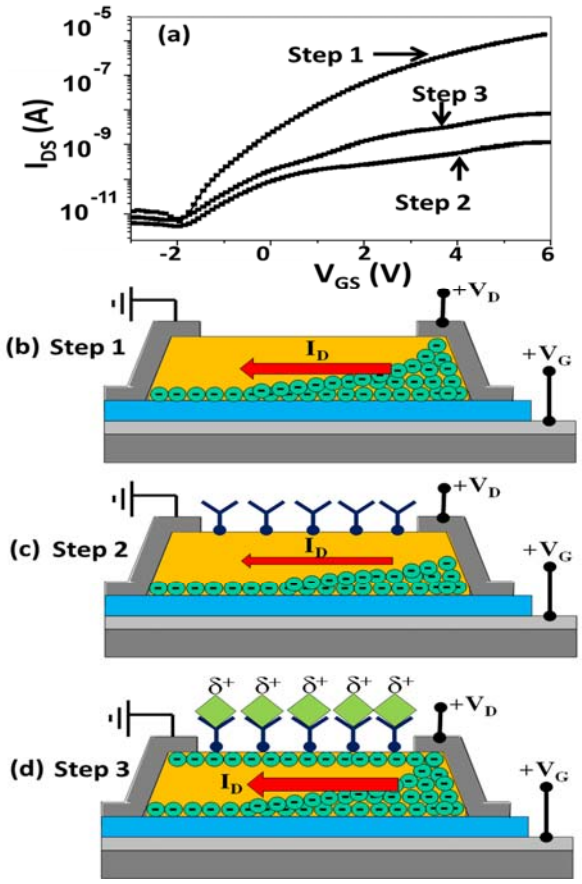

Fig. 7.2. (a) Drain current versus gate bias for fixed drain bias of 10V. Step 1: bare device, Step 2: EGFR-antibody immobilization, and Step 3: EGFR protein detection; (b-d) schematic of the carrier modulation mechanism for steps 1 to 3 respectively. Ref. [121]

accumulation was in addition to the conduction path created near the gate. The combined amount of accumulation layer caused an increase in the current flow. The top molecule layer (reacted protein) acted as a virtual top gate and the antibody layer acted as a virtual insulator layer, thus forming a pseudo-double gated field-effect conduction scheme for the ZnO-bioTFT. The actual measured drain currents that confirmed each step of the detection process are shown in Fig. 7.2(a). The drain voltage is fixed to 10V and the gate voltage is varied from -5V to +15V, and the drain current is measured using an HP4156C semiconductor parameter analyzer and Cascade Microtech probe station.

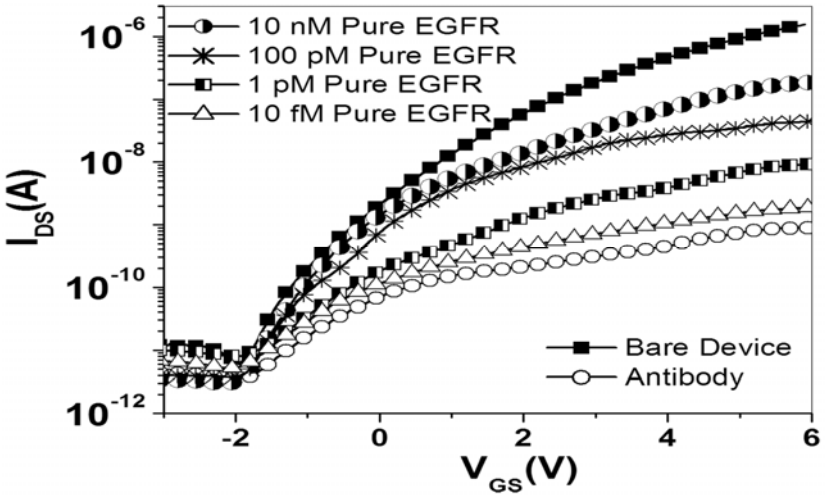

Fig. 7.3. Drain current versus gate bias for various Molar concentrations of pure EGFR proteins detected by the ZnO-bioTFT to demonstrate sensitivity. Ref. [121]

7.4. Immunosensing Results and Discussion

Sensitivity Test: To demonstrate the high sensitivity of the ZnO-bioTFT, solutions of pure EGFR (in PBS) were prepared with four different Molar concentrations using serial dilutions, namely 10 nM, 100 pM, 1 pM, and finally 10 fM. Each EGFR solution (2 μL) was introduced to a separate but similar ZnO-bioTFT fabricated on a

single chip that were simultaneously functionalized with EGFR mAbs. The drain current was monitored as a function of gate voltage with a fixed drain voltage of 10V, for each concentration. Fig. 3 shows the measured drain current versus gate voltage of the bioTFT. An increase in drain current was measured as the EGFR concentration was increased and the graph also shows that the device was able to detect as low as 10 fM of EGFR concentration. The trend in the current readings agrees with the hypothesis provided by the pseudo-double gating effect discussed above.

Selectivity Test: The highly selective sensing of EGFR using the ZnO-bioTFT was also demonstrated. In this experiment, a 5 mg/ml (in PBS, pH 7.4) goat serum solution was prepared, which contains many different species of proteins. As mentioned above, different EGFR solutions were prepared, namely 100 pM, 1 pM, and 10 fM, using this serum solution as the solvent and not pure PBS. For all the concentrations, the total amount of serum present remained approximately the same. Each of the different solutions (2 μL) was introduced onto a chip containing multiple similar bioTFT devices that were bio-functionalized with EGFR mAbs. The drain current of each device was measured as a function of gate voltage, with a fixed drain voltage of 10V. As a control, we first introduced serum solution without the EGFR proteins to the ZnO-bioTFT. Fig. 4(a) shows no change in the drain current for the pure serum confirming that there were no EGFR molecules in the solution. The drain current increased as a function of EGFR concentration. The bio-TFT detected only the EGFR proteins out of the many different proteins present in the serum solution introduced onto the sensing area of the device. Moreover, the device was able to discern as low as 10 fM of EGFR protein concentration

in the serum solution. The sensitivity plot of the device for both pure and in-serum detection is shown in Fig. 4(b) which exhibits linearity in the x-y logarithmic scale.

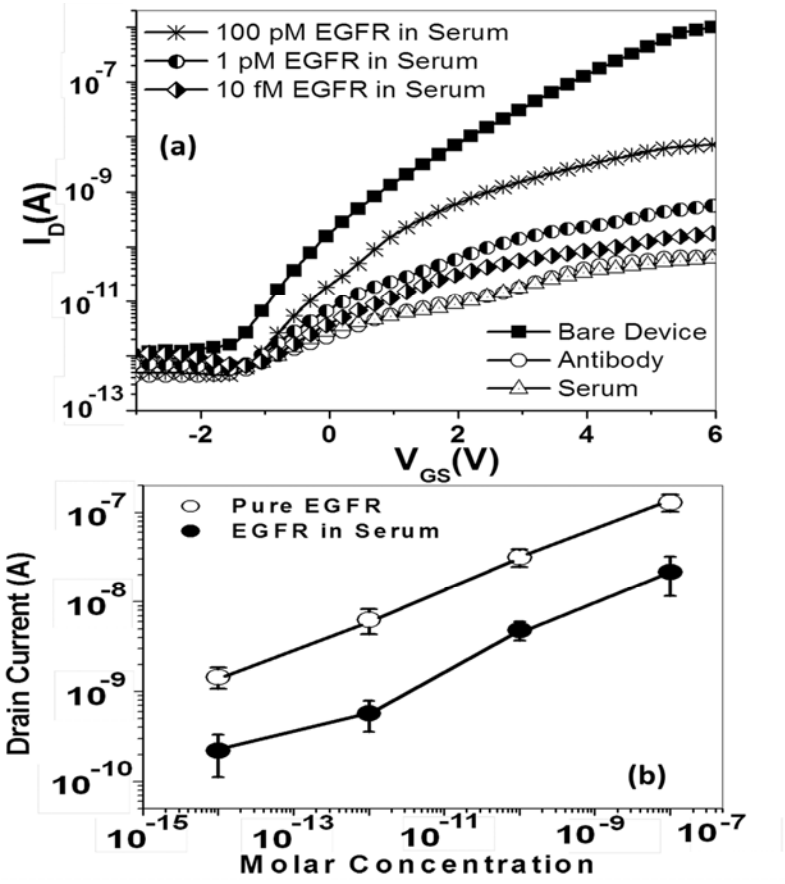

Fig. 7.4. (a) Drain current versus gate bias for various Molar concentrations of EGFR-proteins in a serum solution containing many different proteins. (b) Sensitivity plot of the device for pure protein and protein in serum detection. Ref. [121]

7.5. Summary

In summary, we have demonstrated a ZnO bioTFT that has the ability to perform immunosensing with high sensitivity and selectivity. The channel of the bioTFT is

functionalized with amine-terminated EGFR monoclonal antibodies. EGFR proteins with the lowest concentration of 10 fM were detected by the device in both pure state and selectively in a concentration serum solution containing various other protein species. The ZnO-bioTFT enables bias-controlled operation though its bottom gate configuration. The high sensitivity of the device is attributed to its high on-off ratio, and the output current trend is explained by the pseudo-double gating electric field effect. The realization of the ZnO-bioTFT functionalized with EGFR mAbs reacting with EGFR proteins has potential applications in cancer diagnosis and treatment.

Chapter 8

Conclusion and Suggestions for Future Work

8.1. Conclusion

ZnO is a multifunctional wide bandgap semiconductor that has excellent properties suitable for biosensing applications. ZnO has been shown to be highly sensitive to various chemical species including organic and inorganic gases and liquids. It is also known to be a biocompatible oxide. ZnO nanostructures can be grown on various substrates with tunable morphology. ZnO nanostructures can also have controllable and reversible surface wettability and can be biofunctionalized with various organic linkers for selective molecular binding. Using these multifunctional properties of ZnO, this dissertation focused on the development of biosensors by combining techniques of (i) accurate and high quality growth of multifunctional ZnO thin films and nanostructures, (ii) organic and biomolecular functionalization, and (iii) development of sensor platforms and devices for applications in biochemical detection and dynamic and noninvasive techniques of monitoring biophysical activity.

In order to design the ZnO-based biosensors with high sensitivity and selectivity the nanostructured ZnO sensing layer must be surface treated using various biofunctionalization protocols. In this dissertation we have shown three different biofunctionalization protocols. The first protocol activates ZnO to specifically detect DNA. A three-step procedure to functionalize ZnO nanotips films with ssDNA followed by hybridization with complementary, fluorescein-tagged ssDNA was developed. We demonstrated that the key step for this protocol is to design the bifunctional linker molecule that consists of COOH as the ZnO-binding group, and the open ended chain is

activated to attach to DNA either by (i) thiol-disulfide exchange reaction, or (ii) NHS-ester hydrolysis reaction. The second protocol activates ZnO to specifically bind to monoclonal epithelial growth factor receptor antibodies (mAbs EGFR) through silane linkage chemistry. The third protocol develops a platform for ZnO to sustain a living cell culture on the nanostructure surface. We demonstrated the growth of bovine aortic endothelial cells (BAEC) on fibronectin-treated ZnO nanostructures.

The morphology of the ZnO nanostructure surface also affects the quality of the molecular binding to ZnO. In addition to developing biofunctionalization protocols for ZnO, we also studied the effects of different surface morphologies of nanostructured ZnO on BAEC cell adhesion and proliferation and on DNA binding. For the case of BAEC cell growth on ZnO, we found that there is an inherent tradeoff in choosing the optimal ZnO morphology for the sensing surface. In terms of cell attachment, the cells favor the adhesion to flatter surfaces, but in terms of device performance the sharper surface provides the highest sensitivity due to the large effective sensing area provided by the nanostructures. It is determined that an intermediate morphology of rough ZnO surface is the most suitable morphology for adhesion and viability for cell growth without sacrificing the device sensitivity. For the case of DNA binding to ZnO, FT-IR-ATR spectra and fluorescence emission studies indicated that the ZnO nanorod films with larger surface area (i.e. rough and nanorods) are needed for the immobilization and detection of biomolecules to be optimal. The novel biological surface treatment techniques developed in this research allows the ZnO nanostructures to serve as both the biomolecular interface via surface functionalization and the sensitivity-enhancing layer resulting from the controlled morphology and gigantic effective surface area. More

importantly, this novel approach allows sequential reactions on the surface of ZnO nanostructures and, in principle, can be extended to numerous other molecules and biomolecules.

We also demonstrated a $Mg_xZn_{1-x}O$ nanostructure-modified TFBAR device as a DNA biosensor. The devices were built on Si substrates with an acoustic mirror consisting of alternating quarter-wavelength silicon dioxide (SiO_2) and tungsten (W) layers to isolate the TFBAR from the Si substrate. High quality ZnO and $Mg_xZn_{1-x}O$ thin films are achieved through a radio frequency (RF) sputtering technique**.** Tuning of the device operating frequency was realized through varying the Mg composition in the piezoelectric $Mg_xZn_{1-x}O$ layer. Simulation results based on the transmission line model of the TFBAR showed close agreement with the experimental results. Next, ZnO nanostructures were grown on the TFBAR's top surface using metalorganic chemical vapor deposition (MOCVD) to form the ZnO_{nano}-TFBAR sensor, which offers giant sensing area, faster response, and higher sensitivity over the planar sensor configuration. A mass sensitivity higher than 10^3 Hz cm^2/ng was achieved. In order to study the feasibility of the nano-TFBAR for biosensing, the nanostructured ZnO surfaces were functionalized to selectively immobilize with DNA, which is verified by hybridization with its fluorescence-tagged DNA complement.

We also built a ZnO-nanostructure-based quartz crystal microbalance (ZnO_{nano}-QCM) device for biosensing applications. ZnO nanotips were directly grown on the sensing area of a conventional QCM by metalorganic chemical vapor deposition (MOCVD) through a shadow mask. Scanning electron microscopy (SEM) showed that the ZnO nanotips are dense and uniformly aligned along the normal to the substrate

surface. By using superhydrophilic nano-ZnO surface, more than tenfold increase in mass loading sensitivity of the nano-QCM device was achieved over the conventional QCM. The ZnO nanotip arrays on the ZnO_{nano}-QCM were biofunctionalized for DNA detection using our developed protocol. The selective immobilization and hybridization of DNA oligonucleotide molecules were confirmed by fluorescence microscopy of the ZnO_{nano}-QCM sensing areas.

A dynamic and noninvasive method of monitoring the adhesion and proliferation of bovine aortic endothelial cells (BAEC) using a ZnO nanostructure-modified quartz crystal microbalance (ZnO_{nano}-QCM) biosensor was demonstrated. The ZnO_{nano}-QCM biosensor was deployed *in-situ* of a standard cell culture environment. Cell adhesion to the ZnO surfaces with various morphologies was studied and the optimal morphology is chosen for the BAEC adhesion. The ZnO_{nano}-QCM biosensor displayed enhanced sensitivity compared to the standard QCM sensor with ~10 times higher frequency shift and motional inductance, and ~4 times higher measured motional resistance at full confluency. The dynamic motional resistance and inductance relating to the cells' viscoelastic properties during growth were extracted from the measured time-evolving acoustic spectra. The Butterworth-Van-Dyck (BVD) model was adapted for the ZnO_{nano}-QCM biosensor system and was used to correlate the measured time-evolving acoustic spectra with the motional characteristics of cell attachment and proliferation. The ZnO_{nano}-QCM parameters revealed viscoelastic transitions during the early seeding and adhesion stage in the cell growth. Cellular confluency or the maximum proliferation was detected when the temporal components of the acoustic spectra reached the steady state. The confluency of the cells growing on the ZnO_{nano}-QCM and standard QCM was

verified using fluorescence imaging by replacing the regular cell medium with a fluorescent-tagged medium.

A prototype intelligent food packaging platform was demonstrated, which consisted of a ZnO surface acoustic wave (SAW) sensor directly built on the protein zein. The zein layer with 2 μm thickness acting as a biodegradable food-protecting coating was deposited onto the polyimide flexible substrate through spin-coating. The piezoelectric ZnO film was deposited on the zein layer using RF magnetron sputtering technique. The ZnO thin film grown on zein displayed the polycrystalline wurtzite structure with the preferred c-axis orientation. The ZnO surface was tuned to the hydrophilic state using UV exposure to enhance the sensitivity of the SAW devices. The sensor exhibited a 687.38 MHz operating frequency, and the measured SAW properties were in good agreement with the simulation using the multilayer transmission line (MTL) model. The humidity detection was realized through the SAW frequency shifts with a sensitivity of 3151.22 PPMv. The unique combination of a ZnO SAW sensor with anti-microbial zein-coated flexible substrate enables wireless sensing of food freshness and acchievement of food protection, which is promising for the intellegent food packages.

Finally, a ZnO thin film transistor-based immunosensor (ZnO-bioTFT) prototype was developed. The back-gate configuration TFT had an on-off ratio of 10^8 and a threshold voltage of 4.25 V. The ZnO channel surface was bio-functionalized with primary monoclonal antibodies that selectively bind with epidermal growth factor receptor (EGFR). Detection of the antibody-antigen reaction was achieved through channel carrier modulation via pseudo double-gating field effect caused by the biochemical reaction. The sensitivity of 10 fM detection of pure EGFR proteins was

achieved. Furthermore, the ZnO-bioTFT immunosensor also enabled selectively detecting 10 fM of EGFR in a 5 mg/ml goat serum solution containing various other proteins.

In summary, through the unique multifunctional properties of ZnO and the experimental results that we have presented: ZnO bio-interface development, ZnO-based devices, and high quality nanostructure growth and morphology control we are paving the way to a new generation of biosensing devices and platforms. This new sensor technology presents a great impact on the future classes of biosensor functions such as dynamic and noninvasive cellular monitoring, smart food packaging sensors, multi-modal and multifunctional biosensors, and high throughput single chip sensor arrays that perform highly sensitive and selective biochemical detection. These new biosensor functionalities would lead to a broad impact in drug discovery, environmental monitoring, biomedical applications such as cancer and genetic research, as well as the food industry.

8.2. Suggestions for Future Work

Even with the extensive research that has been done in ZnO-based biosensors, the field is still in its early stages. To be in the mature stage of development, these sensors ideally could be applied at the point-of-care level. Moreover, more studies have to be made in creating a larger database of biofunctionaliation protocols so that a wider range of biomolecules and biological species could be specifically bound to the ZnO nanostructured sensing layer. As we move on to biosensing requirements with increasing complexity, a more stringent design is needed for the device design and material growth.

The following new generation of ZnO biosensing devices and platforms should be studied:

- **Multimodal operation in a single platform:** In this dissertation, we have shown dual-mode sensing devices that have either acoustic-optical or electric-optical modes of operation. A truly multimodal operation should be a focus of further study where the integration of the multiple ZnO-based devices will be developed to include all three modes of operation in a single platform.
- **A 3-Dimensional organic-inorganic biointerface (2D film device platform + 1D nanostructured array):** The integration of the ZnO-based 2D-films with 1D nanostructures such as GZO film with ZnO nanotips arrays will lead to a more powerful interface for the biosensing layer. The ZnO nanotips array will serve the dual role of chemical binding site as well as an enhancer of the light capture. The GZO film serves as a transparent electrode. A study on the growth and morphology control of ZnO on GZO and the subsequent biofunctionaliation of the 3-D biointerface will be of great importance.
- **Integrated devices to form high throughput arrays in a single chip:** In this dissertation, we demonstrated a number of individual discrete devices performing biosensing applications. However, the ultimate goal in creating such biosensing devices is to have a high throughput platform that can handle the detection of many different biochemical reactions simultaneously in a single chip. The integration of these discrete devices into an array of devices is a very important aspect of further research in ZnO-based biosensor design.

References

[1] http://www.strategyr.com/Biosensors_in_Medical_Diagnostics_Market_Report.asp

[2] Anisimkin, V. I., Penza, M., Valentini, A., Quaranta, F., and Vasanelli, L., 1995. Sens. Actuators B: Chem, 23 (2-3), 197-201.

[3] Hsueh, T.-J., Chang, S-J., Hsu, C-L., Lin, Y-R., Chen, I.-C., 2007. App. Phys. Lett. 91, 053111.

[4] Miller, B. G., Trantim, T. W., 1998. J. Am. Chem. Soc. 120, 2666.

[5] Lee, J., Kang, B.S., Hicks, B., Chancellor, Jr., T. F., Chu B. H., Wang, H. –T., Keselowsky, B. G., Rena, F., Lele, T. P., 2008. Biomaterials 29 3743–3749.

[6] Al-Hilli, S. M., Al-Mofarji, R. T., and Willander, M., 2006. App. Phys. Lett. 89, 17, 173119.

[7] Wei, A., Sun, X. W., and Wang, J. X., Lei, Y., Cai, X. P., and Li, C. M., Dong, Z. L., Huang, W., 2006. App. Phys. Lett. 89 (12), 123902.

[8] Reyes, P. I., Zhang, Z., Chen, H., Duan, Z., Zhong, J., Saraf, G., Lu, Y, Taratula, O., Galoppini, E., Boustany, N. N., 2009. IEEE J. Sens. 10 (10) 1302-1307.

[9] Taratula, O., Galoppini, E., Wang, D., Chu, D., Zhang, Z., Chen, H., Saraf, G., and Lu, Y., 2006. J. Phys. Chem. B, 110 (13), 6506-6515.

[10] Zhang, Z., Chen, H., Zhong, J., Saraf, G., and Lu, Y., 2007. J. Electron Mater., 36, 8, 895.

[11] Chen, Y., Reyes, P.I., Duan, Z., Saraf, G., Wittstruck, R., Lu, Y., Taratula, O., and Galoppini, E., 2009. J. Electron. Mater., 38, 8, 1605-1611.

[12] Lodish, et. al., Molecular Cell Biology, McGraw-Hill 2006

[13] Alberts, et. al., Molecular Biology of the Cell, Taylor and Francis 2008

[14] Giuliano, K. A., Taylor, D. L., Fluorescent-protein biosensors: New tools for drug discovery, Trends in Biotechnology, 16, 3, March 1998, pp. 135-140.

[15] Srikant, V., Sergo, V., Clarke, D.R., J. Am. Ceram. Soc., 78, 7, 1935, (1995)

[16] Onodera, A., Tamaki, N., Jin, K., Yamashita, H., Jpn. J. Appl. Phys. Part I., 36, 9b, 6008, (1997).

[17] Prellier, W., Fouchet, A., Mercey, B., Simon, Ch., and Raveau, B., Appl. Phys. Lett., 82, 20, 3490, (2003).

[18] Bundesmann, C., Ashkenov, N., Schubert, M., Spemann, D., Butz, T., Kaidashev, E. M., Appl. Phys. Lett., 82, 12, 1974, (2003).

[19] Zhang, Z., Emanetoglu, N.W., Saraf, G., Chen, Y., Wu, P., Zhong, J., and Lu, Y., Chen, J., Mirochnitchenko, O., Inouye, M., 2006. IEEE Trans. Ultrasonics, Ferroelec. Freq. Contr. 53(4), 786-792.

[20] Zhang, Z., Chen, H., Zhong, J., Saraf, G., and Lu, Y., TMS & IEEE Journal of Electronic Materials, 36, 8, 895, (2007).

[21] Lee, J., Kang, B.S., Hicks, B., Chancellor, Jr., T. F., Chu B. H., Wang, H. –T., Keselowsky, B. G., Rena, F., Lele, T. P., 2008. Biomaterials 29 3743–3749.

[22] Yoshica, R., Kitamura, D., and Maenosono, S., J. Toxicol. Sci., Vol. 34, No. 1, pp. 119-122, 2009.

[23] Liu, J. Goud, P. M. Raj, M. Iyer, Z. Lin Wang and R. R. Tummala, 2008 Electronic Components and Technology Conference

[24] Asif, M. H., Fulati, A., Nur, O., Willander, M., Brännmark, Strålfors, C. P., Börjesson, S. I., and Elinder, F., App. Phys. Lett., 95, 023703 (2009).

[25] Al-Hilli, S., and Willander, M., Nanotechnology 20, 175103 (2009)

[26] Dorfman, A., Kumar, N., and Hahm, J., Langmuir 2006, 22, 4890-4895

[27] Dutta, R., Sharma, P., Pandey, A., Digest J. Nanomat. and Biostruc., 4, 1, 83-87, (2009).

[28] Dai Z., et al., Biosens and Bioelectron., 24, 1286–1291, (2009).

[29] Galoppini, E., Coord. Chem. Rev, 248, p. 1283, (2004).

[30] Yakimova, R., et al., Biosens. Bioelectron., 22, 2780–2785, (2007).

[31] Nel, A. E., et. al., Nature Materials, 8, p.543, (2009).

[32] Fu, Y. Q., et. al., IEEE Sensors Journal, pp. 478-483, (2007).

[33] Israr, M.Q., et al., Thin Solid Films 519, 1106–1109, (2010).

[34] Asif, M.H., et al., Biosens. Bioelectron., 25, 2205–2211, (2010).

[35] Wang, Z. L., Adv. Mater., 21, 4975–4978, (2009).

[36] Wang, J., Sun, X., Wei, X. W., Lei, A., Cai, Y., Li, X. P., and Dong, Z. L., Appl. Phys. Lett. 88, 233106, (2006).

[37] Pradhan, D., Niroui, F., and Leung, K. T., Appl. Mater. Interfaces, 2, 8, pp. 2409–2412, (2010).

[38] Kim, J.S., Park, W. I., Lee, C.-H. and G.-C. Yi, J. of the Korean Phys. Soc., 49, 4, 1635-1639, (2006).

[39] Chang, K. S., Chen, C. C., Sheu, J. T., and Li, Y.-K., Sens. Actuators B, 138, 148–153, (2009).

[40] Chu, Y.-M., Linb, C.-C., Chang, H.-C., Li, C., Guoc, C., Biosens. Bioelectron., 26, 5, 2334-2340 (2011).

[41] Reyes, P.I., Ku, C.-J., Duan, Z., and Lu, Y., Solanki, A., and Lee, K.-B., Appl. Phys. Lett. 98, 173702, (2011).

[42] Hu, W., Liu, Y., Yang, H., Zhou, X., Li, C.M. Biosens. Bioelectron. 26, 8, 3683–3687, (2011).

[43] Hong, X., Chu, X., Zou, P., Liu, Y., Yang, G., Biosens. Bioelectron. 26, 2, 918–922, (2010).

[44] de Julian Fernandez, C., Manera, M.G., Pellegrini, G., Bersani, M., Mattei, G., Rella, R., Vasanelli, L., Mazzoldi, P., Sensors Actuators B, 130, 531–537, (2008).

[45] Taratula, O., Mendelsohn, R., Galoppini, E., Reyes, P.I., Zhang, Z., Duan, Z., Lu, Y., Langmuir, 25, 4, 2107-2113, (2009).

[46] Reyes, P.I., Duan,Z., Lu, Y., Khavulya, D., and Boustany, N., "ZnO Nanostructure-Modified QCM for Dynamic Monitoring of Cell Adhesion and Proliferation" submitted to Biosensors and Bioelectronics Journal (January 2012).

[47] Cao, Y., Galoppini, E., Reyes, P.I., Duan, Z., and Lu, Y., "Morphology Effects on The Biofunctionalization of Nanostructured ZnO", Submitted to Langmuir Letters, (February 2012)

[48] Lakin, K. M., Kline, G. R., McCarron, K. T., IEEE Ultrasonics Symp., 471 (1992).

[49] Ruby, R., Bradley, P., Oshmyansky, Y., Chien, A., Larson III, J.D., IEEE Ultrasonics Symp., 813, (2001).

[50] Mang L., and Hickernell, F., Proc. IEEE Int. Freq. Control Symp., 363, (1996).

[51] Seabury, C. W., Kobrin, P. H., Addison, R., and Havens, D. P., IEEE MTT-S Digest, 181, (1997).

[52] Kaitila, J., Ylilammi, M., Molarius, J., Ella, J., and Makkonen, T., Proc. IEEE Int. Ultrasonics Symp., 803, (2001).

[53] Park, Y. S., Pinkett, S., Kenney, J.S., and Hunt, W.D., Proc. IEEE Int. Ultrasonics Symp., 839, (2001).

[54] Hauptmann, P., Lucklum R., and Schröder, J. Proc. IEEE Int. Ultrasonics Symp, 56, (2003).

[55] Mansfeld, G. D., and Kotelyansky, I.M., Proc. IEEE Int. Ultrasonics Symp., 909, (2002).

[56] Gabl, R., Green, E., Schreiter, M., Feucht, H.D., Zeininger, H., Primig, R., Pitzer, D., Eckstein G., and Wersing, W., Reichl W., and Runck, J., Proc. IEEE Sensors 2, 1184, (2003).

[57] Mai, L., Kim, D.H., Yim, M., and Yoon, G., Microwave and Opt. Tech. Lett. 42, 505 (2004).

[58] Zhang, H., Marma, M. S., Kim, E. S., McKenna, C. E., and Thompson, M. E., 17th IEEE Int. Conf. on Micro Electro Mech. Sys. 347, (2004).

[59] Emanetoglu, N.W., Muthukumar, S., Wu, P., Wittstruck, R., and Lu, Y., IEEE Intl. Ultrason. Symp. Proc. 253, (2001).

[60] Emanetoglu, N.W., Muthukumar, S., Wu, P., Wittstruck, R., Chen, Y., Lu, Y., IEEE Trans. on Ultrason. Ferroelectr. Freq. Contr. 50, 537 (2003).

[61] Wittstruck, R.H., Tong, X., Emanetoglu, N.W., Wu, P., Chen, Y., Zhu, J., Muthukumar, S., Lu, Y., Ballato, A., IEEE Trans. on Ultrason. Ferroelectr. Freq. Contr. 50, 1272, (2003).

[62] Yoshino, Y., Inoue, K., Takeuchi, M., Ohwada, K., Vacuum 5, 601, (1998)

[63] Chen, H., Zhong, J., Saraf, G., Zhang, Z., Lu, Y., Fetter, L. A., and Pai, C. S., Proc. SPIE, 5592, 164, (2004)

[64] Zhong, J., Saraf, G., Muthukumar, S., Chen, H., Chen, Y., and Lu, Y., J. Electr. Mater. 33, 654, (2004)

[65] Ballato, A., "Transmission-line Analogs for Piezoelectric Layered Structures", Ph.D. dissertation, Polytechnic Institute of Brooklyn, NY, June 1972.

[66] Sauerbrey, G., Verwendung von Schwingquarzen zur Wagung dunner Schichten und zur Mikrowagung, Z Phys 155 (1959), 206 – 222 (in German)

[67] Wegener, J., Janshoff, A., and Galla, H-J., 1998, Eur. Biophys. J. 28, 26-37.

[68] Freshney, R. I., Culture of Animal Cells: A Manual of Basic Techniques, 5th Ed., 2005, Wiley.

[69] Georgakoudi, I., Solban, N., Novak, J., Rice, W. L., Wei, X., Hasan, T., Lin, C. P., 2004. Cancer Res. 64, 5044–5047.

[70] Fredriksson, C., Kihlman, S., Rodahl, M., Kasemo, B., 1998. Langmuir 14 248-251.

[71] Marx, K. A., Zhou, T., Montrone, A., McIntosh, D., Brauhut, S. J., 2005. Anal. Biochem. 343, 23-34.

[72] Lord, M. S., Modin, C., Foss, M., Duch, M., Simmons, A., Pedersen, F. S., Milthorpe, F. Besenbacher, B. K., 2006. Biomaterials, 27, 4529-4537.

[73] Solly, K., Wang, X., Xu, X., Strulovici, B., Zheng. W., 2004. Assay and Drug Dev. Technol. 2 (4), 363-372.

[74] Rodahl, M., Höök, F., Krozer, A., Brzezinski, P., Kasemo, B., 1995. Rev. Sci. Instrum. 66 (7) 3924-3930.

[75] Wegener, J., Janshoff, A., Steinem, C., 2001. Cell Biochem. Biophys. 34, 121-151.

[76] Feiler, A. A., Sahlholm, A., Sandberg, T., Caldwell, K. D., 2007. J. Colloid Interface Sci. 315 (2), 475-481.

[77] Ishida, N., Biggs, S., 2007. Langmuir 23 (22), 11083–11088.

[78] Hovgaard, M. B., Rechendorff, K., Chevallier, J., Foss, M., Beenbacher, F., 2008. J. Phys. Chem. B. 112, 8241-8249.

[79] Homola, J., Yee, S. S., Gauglitz, G., 1999. Sens. Actuators B: Chem. 54 (1-2), 3-15.

[80] Zhou, X. C., Huang, L. Q., Li, S. F. Y., 2001. Biosens. Bioelectron. 16 (1), 85-95.

[81] Muratsugu, M., Ohta, F., Miya, Y., Hosokawa, T., Kurosawa, S., Kamo, N., Ikeda, H., 1993. Anal. Chem. 65, 2933-2937.

[82] Alessandrini, A., Croce, M. A., Tiozzo, R., Facci, P., 2006. App. Phys. Lett. 88, 083905.

[83] Heitmann, V., and Wegener, J., 2007, Anal. Chem., 79, 3392-3400

[84] Li, J., Thielmann, C., Reuning, U., and Johannsmann, D., 2005, Biosens. Bioelectron. 20, 1333-1340.

[85] Modin, C., Stranne, A. L., Foss, M., Duch, M., Justesen, J., Chevallier, J., Andersen, L. K., Hemmersam, A. G., Pedersen, F. S., and Besenbacher, F., 2006, Biomaterials, 27, 1346-1354.

[86] Rodahl, M., Höök, F., Fredriksson, C., Keller, C. A., Krozer, A., Brzezinski, P., Voinova, M., Kasemo, B., 1997, Faraday Discuss., 107, 229-246.

[87] Zhou, X. C., Huang, L. Q., Li, S. F. Y., 2001. Biosens. Bioelectron. 16 (1), 85-95.

[88] Asif, M. H., Fulati, A., Nur, O., Willander, M., Brännmark, C., Strålfors, P., Börjesson, S. I., and Elinder, F., 2009. App. Phys. Lett., 95, 023703.

[89] Al-Hilli, S. and Willander, M. , 2009. Nanotechnol. 20, 175103.

[90] Dutta R., Sharma P., and Pandey A., 2009. Dig. J. Nanomater. Biostruct., 4, 1, 83-87.

[91] Bandey H., Hillman A. R., Brown M. J., and Martin S. J., 1997. Faraday Disscus, 107, 105-121.

[92] Wegener J., Seebach J., Janshoff A., and Galla, H-J., 2000. Biophys. J. 78, 2821-2833.

[93] Yam, K. L., Takhistov, P. T., and Miltz, J., 2005, J. Food Sci., 70, 1, R1-R10

[94] O'Riordana, T. C., Voraberger, H., Kerry, J. P., Papkovsky, D. B., 2005, Anal. Chimica Acta, 530, 135–141.

[95] Mills, A., 1998, Sens. Actuators, B, 51, 60–68.

[96] Chen, Z., Lu, C., 2005, Sensor Lett., 3, 4, 274-295.

[97] Mills, A., 2005, Chem. Soc. Rev., 34, 1003–1011.

[98] Smolander, M., Alakomi, H.-L., Ritvanen, T., Vainionpaa, J., Ahvenainen, R., 2004. Food Control 15(3):217–29.

[99] Plutowska, B.; Wardencki, W., 2006, Food Chem., 101, 845-872.

[100] Winquist, F., Krantz-Rulcker, C.; Lundstrom, I., 2004, MRS Bull., 29, 726-731.

[101] Wright, A. T., Anslyn, E. V., 2006, Chem. Rev., 35, 14-28.

[102] Hong, H. S., and Chung, G. S., 2010, Sensors and Actuators B 148 347–352

[103] Matsushima, M., Danno, G., Takezawa, H., Izumi, Y., 1997 Biochimica et Biophysica Acta, 1339, 14-22.

[104] Ke, S., Kokini, J., Huang, R, 2009, J. Agric. Food Chem., 57, 2186-2192.

[105] Shuka, R.; Cheryan, M.; 2001, Industrial crops and products, 13, 171-192.

[106] Rodov, V., Ben-Yehoshua, S., Fierman, T., and Fang, D., 1995 Hort. Sci, 30, (2) 299–302.

[107] Reyes, P. Li, J., Duan, Z., Yang, X., Cai, Y., Huang, Q., and Lu, Y., "ZnO Surface Acoustic Wave Sensors Built on Zein-Coated Flexible Food Packages", Submitted to Sensor Letters (February 2012).

[108] Turgeman, R., Gershevitz, O., Deutsch, M., Ocko, B.M., Gedanken, A., Sukenik., Chem. Mater. 2005, 17, 5048-5056

[109] Gallipeau, D.W., Stroschine, J.D., Snow, K.A., Vetelino, K.A., Hines, K.R., and Story, P.R., Sensors and Actuators B, 24-25, 696-700 (1995).

[110] Begveld, P., Sens. Actuators B 88, 1-20, (2003).

[111] Asahi, M., and Matsuo, T., Suppl. Jpn. Soy. Appl. Phys. 44, 339, (1975)

[112] Gimmel, P., Schierbaum, K. D., Gopel, W., Van den Vlekkert, H. H., and de Rooy, N. F., Sens. Actuators B, 1, 345, (1990).

[113] Estela, P., Stewart, A. G., Yan, F., and Migliorato, P., Electrochimca Acta 50, 4995-5000, (2005).

[114] Yu, J., Jha, S. K., Xiao, L., Liu, Q., Wang, P., Surya, C., and Yang, M., Biosens. Bioelectron. 23, 513-519, (2007).

[115] Mabeck, J. T., and Malliaras, G. G., Anal. Bioanal. Chem. 384, 343-353, (2006).

[116] Torsi, L., Dodabalapur, A., Sabbatini, L., and Zambonin, P. G., Sens. Actuators B, 67, 312-316, (2000).

[117] Liu, J., Agrawal, M., and Varahramyan, K., Sens. Actuators B, 135, 195-199, (2008).

[118] Zhang, Q., and Subramanian, V., Biosens. Bioelectron. 22, 3182-3187, (2007).

[119] Chang, K. S., Chen, C. C., Sheu, J. T., and LiSens, Y.-K., Actuators B, 138, 148–153, (2009).

[120] Chu, Y.-M., Linb, C.-C., Chang, H.-C., Li, C., Guoc, C., Biosens. Bioelectron., 26, 5, 2334-2340 (2011).

[121] Reyes, P.I., Ku, C.-J., Duan, Z., and Lu, Y., Solanki, A., and Lee, K.-B., Appl. Phys. Lett. 98, 173702, (2011).

[122] Murali, R., Brennan, P., Kieber-Emmons, T.,and Greene, M. I., Proc. Natl. Acad. Sci. USA, Biochemistry, 93, 6252-6257, (1996)